Study of Spin Waves in In-plane Magnetized Thin Films by means of Brillouin Light Scattering and Magneto-optical Kerr Effect

Eric Robert Joseph Edwards

2012

To my parents. For everything.

Zusammenfassung

Die vorliegende Doktorarbeit berichtet über experimentelle Untersuchungen von Spinwellen in in der Ebene magnetisierten dünnen Filmen mit strukturierter Oberfläche. In dieser Untersuchung haben wir zwei abbildende Techniken verwendet, mikrofokussierte Brillouinlichtstreuung (μBLS) und ferromagnetisches Resonanz Scanning Kerreffekt Mikroskopie (SKEM). Verschiedene Arten von Experimenten wurden in in der Ebene magnetisierten dnnen Filmen durchgeführt.

In der ersten Serie von Experimenten haben wir den SKEM aufgebaut und seine Funktionalität demonstriert. Bei SKEM handelt es sich um ein modifiziertes, zeitaufgelöstes magnetooptisches Kerreffekt Experiment (TR-MOKE). Im Gegensatz zum zeitaufgelösten MOKE, welches die Magnetisierungsdynamik in der Zeitdömane und unter Auswirkung von Anregungspulsen (pump-probe Technik) untersucht, benutzt SKEM eine Synchronisierung zwischen dem sondierenden Laserpuls und dem anregenden Microwellenfrequenz-Sinusstrom um die Wellen der Magnetisierung über einen ganzen Zyklus des anregenden Stromes zu messen. Durch Abstimmen der Frequenz des anregenden Stromes auf die der Eigenmoden des Systemes kann man diese Eigenmoden direkt im Ortsraum abbilden. Im ersten Experiment untersuchten wir das Spektrum der magnetostatischen Spinwellenmoden in einer makroskopischen Yttrium Eisen Granat (YIG) Scheibe. Unsere Ergebnisse bestätigen zahlreiche vorherige Experimente, während sie subtile räumliche Eigenschaften der Eigenmoden, die bisher in ortsbeschränkten Systemen noch nicht beobachtet wurden, aufzeigen. Im zweiten Experiment verwendeten wir den SKEM-Aufbau um mikroskopische Proben zu untersuchen. Wir bildeten die Moden mit beugungsbegrenzter räumlicher Auflösung ab und konnten deshalb Eigenmoden der magnetischen Strukturen bis hin zu sehr hoher Ordnung untersuchen. Wir beobachteten die wohlbekannte Modenlokalisierung an den Rändern der in der Ebene magnetisierten Elemente, die von Demagnetisierungseffekten aufgrund der nichtelliptischen Form der Elemente herrühren.

Die zweite Serie von Experimenten wurden mit μBLS an einer Serie von

Spin-Hall Systemen durchgeführt, die aus einer Permalloy Scheibe bestehen, welche auf einem Platinstreifen liegen, durch den ein elektrischer Strom fließt. Aufgrund des Spin-Hall Effekts führt der Elektronfluss im Platinstreifen zu einem transversalen Spinstrom, der auf die Py/Pt Grenzfläche trifft. Im ersten Experiment benutzten wir die Möglichkeit des μBLS magnetische thermische Fluktuationen messen zu können, um die Auswirkung des Spin-Transfer-Torques (STT) auf die Fluktuationen des Systems zu untersuchen. Wir konnten zeigen, dass STT zu einer Unterdrückung oder Verstärkung der magnetischen Fluktuationen führt, je nach dem wie die Spinpolarsierung des Spinstroms und die statische Magnetisierung in der Py-Scheibe zueinander ausgerichtet sind. Im zweiten Experiment messen wir die ferromagnetische Resonanzcharakterstik einer Py-Scheibe in einem ähnlichen System. Wir erreichten eine zweifache Verringerung der FMR-Linienbreite des Py relativ zum Literaturwert in unstruktuierten Filmen. In der dritten Experimentserie studierten wir die Entwicklung der parametrischen Spinwelleninstabilität unter Einfluss des STT. Wir finden, dass STT während es die Fluktuation verstärkt, zu einer Reduzierung des Leistungschwellwerts, bei dem die parametrische Spinwelleninstabilität einsetzt, führt. Über zeitaufgelöste Messungen untersuchten wir das Anwachsen der dynamischen Magnetisierung während dem parallelen Pumpen und konnten somit die Relaxtionsfrequenz des magnetischen Systems bestimmen.

Abstract

This dissertation reports on experimental studies of spin-wave excitations in in-plane magnetized thin films and patterned structures. In this study we have used two optical techniques, microfocus Brillouin light scattering (μBLS) and ferromagnetic resonance scanning Kerr effect imaging (SKEM). Several types of experiments have been performed on in-plane magnetized thin films.

In the first series of experiments, we construct and demonstrate the functionality of the SKEM setup. SKEM represents a modification of time-resolved magneto-optical Kerr effect (TR-MOKE) experiments. In contrast to TR-MOKE, which allows investigation of the magnetization dynamics in the time domain under the influence of excitation pulses (the pump-probe-technique), SKEM utilizes synchronization between the probing laser pulses and the excitation microwave-frequency sinusoidal current to measure the waveform of the dynamic magnetization over an entire cycle of the excitation current. By tuning the frequency of the excitation current to the frequencies of the eigenmodes of the system, one may directly image these eigenmodes in real space. In the first experiment, we investigate the spectrum of magnetostatic spin-wave modes in a macroscopic yttrium iron garnet (YIG) disk. Our results confirm the results of numerous previous experiments, while revealing subtle spatial features of the eigenmodes, heretofore unobserved in confined systems. In the second experiment, we use the SKEM setup to investigate microscopic samples. We image the modes with diffraction-limited spatial resolution and, therefore, investigate the eigenmodes of the magnetic elements up to very high order. We observe the well-known mode localization at the edges of in-plane magnetized elements, resulting from demagnetizing effects due to the elements' nonellipsoidal shape.

The second series of experiments have been performed with μBLS on a series of spin Hall systems consisting of a Py disk fabricated on top of a Pt strip carrying electrical current. By means of the spin Hall effect, the electron flow in the Pt strip results in a transverse spin current, incident on the Py/Pt interface. In the first experiment, we use the possibility of μBLS

to measure magnetic thermal fluctuations to study the effect of spin transfer torque (STT) on the fluctuations of the system. We are able to show that STT leads to suppression or enhancement of the magnetic fluctuations, depending on the relative orientation of the spin polarization of the spin current and the static magnetization in the Py disk. In the second experiment, we measure the ferromagnetic resonance (FMR) characteristics of the Py disk in a similar system. We are able to reach a two-fold reduction of the FMR-linewidth in Py below its value in free-standing films. In the third series of experiment, we investigate the development of the parametric spin-wave instability under the influence of STT. We find that STT, in enhancing the fluctuations, significantly reduces the power threshold of the onset of the parametric spin-wave instability. By means of temporal measurements, we study the growth of the dynamic magnetization under parallel pumping and are able to determine the relaxation frequency of the magnetic system

Acknowledgements

I would like to thank my advisor, Sergej Demokritov, for his scientific guidance and his personal support.

I would like to thank Vlad Demidov and Matthias Buchmeier, whose assistance made these experiments possible.

I would like to thank Sergei Urazhdin, without whom the samples for the second series of experiments would not exist.

I would like to thank Oleksandr Dzyapko, Henning Ulrichs, Patryk Nowik-Boltyk and Johann Jersch for the exchange of ideas and tolerating countless questions on the finer points of the German language.

I would like to thank the science and math teachers at Saint Benedict at Auburndale, the physics faculty at the University of Alabama, and the staff of the MINT Institute. In particular, I would like to thank Bill Butler, for introducing me to the research field of magnetism, Tim Mewes for allowing me to carry out my first experiments in his lab, and Sanjoy Sarker for many enlightening discussions about physics, and life.

I would like to thank Bill Bailey, Georg Hoffstaetter, and Moty Heiblum for my time spent in their labs.

I would like to thank my fellow physics students—Colbert, Hippie, Andy, and Tim—for learning it all together.

I would like to thank my family and friends—in particular my mom and dad, my brother and sister, my honorary brother Mike, the Nissenbaums, Rachel, Isti, Suitopia, SBA Class of 2005, and everyone else along the way—for everything. And Melley, for your love and support.

Contents

List of Figures

Chapter 1

Fundamental Concepts

1.1 Introduction

The low-lying energy states of unbounded ferromagnetic media, called spin waves, were first introduced theoretically by Bloch on a microscopic model [1]. Far below the Curie temperature T_c, the excitations of a system of stationary spins coupled by the exchange interaction are found to be wavelike, i.e. spin waves, whose existence lead to a fractional reduction of the magnetization. This result, known as Bloch's $T^{3/2}$ law, since the reduction of the magnetization is proportional to $T^{3/2}$ where T is the temperature of the spin system, introduced the concept of spin waves to solid state physics. The experimental verification of Bloch's $T^{3/2}$ law [2] by nuclear magnetic resonance measurements first occurred decades after his prediction, precipitated by the discovery of the insulating ferromagnet $CrBr_3$ [3].

In his original work, Bloch [1] derived the first dispersion relation for spin waves. In this simplified model, accounting only for the energy of the exchange interaction among neighboring spins, he found $\omega(k) = Ck^2$ for spin waves of wavevector k where C is the spin stiffness constant. Holstein and Primakoff [4] extended Bloch's treatment to derive the spin-wave dispersion in the presence of an external magnetic field, accounting for the exchange interaction among neighboring spins and the magnetic (dipole-dipole) interaction. These microscopic models, while accurate, are often cumbersome for the interpretation of experimental results—the introduction of phenomenological constants to account for anisotropy, magnetoelastic, or magnetostatic energies is significantly simplified by a macroscopic, field-theoretic approach. A treatment of microscopic spin-wave theory may be found in [5].

Macroscopic spin-wave theory addresses the dynamics of a continuously varying field, the magnetization, obtained by coarse graining over the micro-

scopic spin system [6]. Solutions of macroscopic Maxwell's equation together with the equation of motion of the magnetization in ferromagnetic media describe the magnetization dynamics. The equation of motion for the magnetization in insulating, unbounded ferromagnetic media was obtained by Landau and Lifshitz [7], who simultaneously predicted the phenomenon of ferromagnetic resonance—the resonant absorption of electromagnetic energy by a ferromagnet driven by a time-varying magnetic field. A decade later, ferromagnetic resonance was experimentally observed by Griffiths [8].

The theory of ferromagnetic resonance in ferromagnets of finite spatial extent was addressed by Kittel [9]. He showed that the frequency of resonance depends sensitively on the shape of the specimen due to the shape-dependent magnetic field produced by the magnetization. Under the influence of a spatially uniform dynamic magnetic field, ferromagnetic resonance occurs for the spin-wave mode with wavevector $k = 0$, in which all spins precess in phase about the effective magnetic field. Herring and Kittel [10] first derived the spin-wave dispersion for non-uniform precession ($k \neq 0$) on a macroscopic model in an unbounded ferromagnet.

Ferromagnetic resonance experiments in the presence of inhomogeneous rf fields [11] subsequently lead to the investigation of non-uniform precession in bounded ferromagnets. Walker [12] analytically derived the spin-wave dispersion for the particular case of an ellipsoid of revolution in the magnetostatic approximation. At microwave frequencies, the spin-wave wavenumber k is much greater than that of the corresponding electromagnetic wave $k_0 = \frac{\omega}{c} << k$. Therefore the displacement current in macroscopic Maxwell's equations may be ignored. In addition, we restrict attention to insulating ferromagnets for which eddy currents are negligible. Under these conditions, macroscopic Maxwell's equations reduce to their magnetostatic form, in which the equations for magnetic fields are completely decoupled from those for electric fields. This approximation becomes more accurate with decreasing sample size or increasing spin-wave wavenumber. [1]

Thereafter, Dillon [13, 14] and Walker [15] experimentally studied magnetostatic modes of ferrites in plates and spheroids, respectively. Kittel [16]

[1] In his analysis, Walker also ignored the effect of the exchange interaction, since the exchange interaction is short-ranged and has only a slight effect on spin waves as $k \to 0$ in ferrite samples of millimeter extent. For this reason, such waves have become known as "magnetostatic" waves. Following the accepted terminology, we will use "spin waves" to designate magnetization oscillations where the effects of exchange may be important, and solely "magnetostatic waves" to designate magnetization oscillations whereby the effects of exchange are neglected. It should be borne in mind, however, that in macroscopic spin-wave theory both waves follow from Maxwell's equations in the magnetostatic approximation.

predicted the excitation of non-uniform spin-wave modes by a uniform dynamic magnetic field in thin films (ferrogmagnets confined in one dimension) magnetized normally to the plane of the film. This phenomenon, known as spin-wave resonance (SWR), was observed in ferromagnetic resonance experiments by Seavey and Tannenwald [17]. Damon and Eshbach [18] obtained the magnetostatic mode spectrum for thin ferromagnetic films magnetized in the plane of the film. Later, Hurben and Patton [19, 20] reexamined the magnetostatic mode spectrum in detail. The spin-wave spectrum of in-plane magnetized thin films under the influence of dipole-dipole as well as exchange interactions was subsequently studied by several researchers [21–25]. The widely used theory of Kalinikos and Slavin [22] obtained an explicit expression for the spin-wave dispersion in a perturbation theory.

The development of macroscopic spin-wave theory followed closely the development of microwave ferrite technology [26]. Technology for analog signal processing based on magnetostatic waves [27] in yttrium iron garnet (YIG) [28] created strong interest in magnetostatic wave techology as an alternative to surface acoustic wave technology at microwave frequencies (1–20 GHz).

Today, the continued technological interest in spin waves stems from their potential application in information processing. In recent years, YIG has been used as a medium to elaborate the principles of signal processing utilizing propagating waves of magnetization [29] and led, for example, to the experimental demonstration of prototypes of devices, such as spin-wave logical gates [30] and electronically controllable magnonic crystals [31]. YIG, however, is not compatible with standard semiconductor technology, which hinders its applications in modern integrated electronics. Therefore, the recent development of spin-wave based technology has focused on ferromagnetic transition metal alloys, such as $Ni_{80}Fe_{20}$ = Permalloy (Py).

With the discovery of spin-transfer torque (STT), particular interest has been focused on current-induced magnetization dynamics. The possibility to control high-frequency magnetization dynamics using dc currents makes STT phenomena promising for generation [32–35] and highly sensitive detection [36, 37] of microwave signals, as well as generation of spin waves for magnonic applications [38–40]. In addition, the effect of STT on the dynamic magnetic damping [41,42] can be utilized in integrated microwave technology for the implementation of high-quality microscopic microwave resonators and filters.

The optical study of spin waves began several decades ago, notably by means of the Faraday effect and magneto-optical Kerr effect (MOKE) [43–46] and Brillouin light scattering (BLS) [47,48]. The magneto-optical Kerr effect designates the rotation of the polarization of linearly polarized light as well as

the appearance of ellipticity upon reflection from the surface of the magnetic medium. The Faraday effect denotes an analogous effect upon transmission through a transparent sample. Brillouin light scattering designates the inelastic scattering of photons on magnons. Techniques based on these effects have been developed to study the spatial variation of the magnetization with diffraction-limited resolution, a prerequisite for the study of technologically interesting samples. In the first experiments of this work, we demonstrate the ability of a Faraday/MOKE-based setup to study magnetostatic waves with high spatial resolution, yielding maps of the magnetization in the frequency domain. In the second series of experiments, we apply BLS to study current-induced magnetization dynamics in a Py disk.

The dissertation is organized as follows. An introductory chapter presents the context of the experiments and fundamental concepts necessary for the interpretation of experimental results. In chapter 2, the experimental techniques used for the investigation of spin waves, scanning ferromagnetic resonance scanning magneto-optical Faraday/Kerr effect imaging (abbreviated as SFEM or SKEM) and microfocus Brillouin light scattering (μBLS) are discussed. A description of the SKEM setup, constructed as part of this work, is presented. The following five chapters, chapters 3–7, present the experimental results. Chapter 3 discusses experiments on a macroscopic YIG disk by means of SKEM. Chapter 4 covers experiments on microscopic Py elements by means of SKEM. Chapter 5 introduces the Py/Pt spin Hall system and discusses results of experiments on the magnetic fluctuations in Py by means of μBLS. Chapter 6 presents results of experiments on the ferrogmagnetic resonance characterstics of Py. Chapter 7 presents results of experiments on the parametric spin-wave instability in Py.

1.2 Fundamental Concepts

In this section, we discuss the fundamental concepts necessary for the interpretation of the experimental results presented in chapter 3–7 of this dissertation.

1.2.1 Macroscopic spin wave theory

In this section, we derive germane results from macroscopic spin-wave theory. We develop the problem sequentially, in order of increasing complexity. We present the equation of motion of the magnetization, and discuss uniform magnetization oscillations in an unbounded ferromagnet leading to the phenomenon of ferromagnetic resonance. We then address the problem of

non-uniform magnetization oscillations in an unbounded ferromagnet using the magnetostatic approximation. As a next step, we present the results for uniform magnetization oscillations in a bounded ferromagnet. Finally, we address the problem of non-uniform oscillations in a bounded ferromagnet, which underlines the importance of sample configuration in calculating the spin-wave spectrum in real specimens. In the next section, we address spin waves in thin ferromagnetic films magnetized in the plane of the film, the sample configuration relevant to the experimental results in this work.

It is well known from atomic physics [49] that the precession of a rigid magnetic moment $\vec{\mu}$ in the presence of a magnetic filed $\vec{H}$ is described by

$$\frac{\partial \vec{m}}{\partial t} = -\gamma \vec{\mu} \times \vec{H} \tag{1.1}$$

where γ is the gyromagnetic ratio. This is the so-called Larmor precession. For free electrons $\gamma = \frac{2\mu_B}{\hbar} > 0$ where μ_B is a Bohr magneton and $h = 2\pi\hbar$ is Planck's constant.

Macroscopic spin-wave theory replaces the microscopic theory based on individual spins or magnetic moments with a treatment based on the magnetic polarization, or magnetization $\vec{M}$. We define $\vec{M}$ by a coarse-graining procedure over the spin system. For simplicity, consider a one-dimensional spin system of uniformly spaced spins separated by a distance a. Coarse graining consists in defining a discrete coordinate x_i uniformly spaced by $\mathrm{d}x$ along the spin chain for which $a << \mathrm{d}x << \lambda$ where λ is the minimum spin-wave wavelength of interest. The local magnetization $\vec{M}(x_i)$ is defined by

$$\vec{M}(x_i) = \frac{\sum_{\mathrm{d}x} \vec{\mu}}{\mathrm{d}x} \tag{1.2}$$

where the sum $\sum_{\mathrm{d}x} \vec{\mu}$ is over all magnetic moments $\vec{\mu}$ in the interval $[x_i \pm \frac{\mathrm{d}x}{2}]$. Due to the inequality $\mathrm{d}x << \lambda$, we regard x_i as a continuous variable. We consider $\vec{M}(x)$ as a continuously varying field, although the underlying spin system is discrete [50].

Under these conditions, Landau and Lifshitz [6, 7] first derived the equation of motion of the magnetization,

$$\frac{\partial \vec{M}}{\partial t} = -\gamma \vec{M} \times \vec{H}_{eff} \tag{1.3}$$

where the effective magnetic field $\vec{H}_{eff}$ reflects contributions to the free energy functional $F[\vec{M}]$ for degrees of freedom coupled to the magnetization $\vec{M}(\vec{x})$. Hence, $\vec{H}_{eff} = -\frac{\partial}{\partial \vec{M}} F[\vec{M}]$ which, in general, includes contributions from the external applied field, shape anisotropy, magneto-crystalline anisotropy, as well as the exchange interaction.

- The external applied filed $\vec{H}_0$ couples to the magnetization through the Zeeman energy density of the form $-\vec{M} \cdot \vec{H}_0$.

- Shape anisotropy results from the purely magnetic dipole interaction between the magnetic moments of the system. It can be shown [5], the the resultant energy density is of the form $-\frac{1}{2}\vec{H}_d \cdot \vec{M}$, where $\vec{H}_d$ is the static magnetic field created by the magnetization $\vec{M}$, called the demagnetizing field. As a convention, the demagnetizing field is written $\vec{H}_d = -\overleftrightarrow{N}\ \vec{M}$, where $\overleftrightarrow{N}$ is called the demagnetization tensor. For a sample of arbitrary shape, $\vec{H}_d$ will, in general, be non-uniform inside the ferromagnet. In the special case of an ellipsoid, however, the field will be constant inside the ferromagnet. Furthermore, if the coordinate axes are aligned along the ellipsoid axes, $\overleftrightarrow{N}$ becomes diagonal, and expressions for the diagonal components can be obtained for the case of an arbitrary ellipsoid [51].

- The effective magnetic field also includes effects from the magneto-crystalline anisotropy, which results in a preferential alignment of the magnetization along axes relative to the crystal axes due to spin-orbit coupling; however, in epitaxial YIG and Py the effective field due to magneto-crystalline anisotropy is on the order of 1 Oe, negligible in comparison with the bias field (> 500 Oe) and will therefore be ignored in this treatment.

- Finally, it can be shown [5] that the form of the exchange energy density is $C\frac{\partial M_\alpha}{\partial x_\mu}\frac{\partial M_\alpha}{\partial x_\mu}$ where summation over repeated indices is implied and C is a scalar reflecting the isotropy of the medium (for an anisotropic medium, C is replaced by a tensor). This results in an effective field of the exchange interaction $\vec{H}_{ex} = q\nabla^2\vec{M}$ where q is the exchange constant.[2] This form of the exchange field reflects the fact that uniform alignment of spins minimizes the exchange energy, while spatial non-uniformities of the magnetization serve to increase the exchange energy.

The simplest solution of 1.3 is obtained in the case of an unbounded ferromagnet under the influence of a spatially uniform high-frequency magnetic field [50].

We decompose the field and magnetization into a static and time-varying

[2]This exchange constant q is related to the previous exchange stiffness constant C by $C = \gamma M_0 q$.

component,

$$\vec{H}_{eff}(t) = H_0\hat{z} + \vec{h}e^{i\omega t} \tag{1.4}$$

$$\vec{M}(t) = M_0\hat{z} + \vec{m}e^{i\omega t} \tag{1.5}$$

where $\vec{h}$ and $\vec{m}$ are the amplitude vectors of the time-varying field and magetization, respectively. We assume $|\vec{h}| << |\vec{H}_0|$ and $|\vec{m}| << |\vec{M}_0|$, where $\vec{H}_0 = H_0\hat{z}$ and $\vec{M}_0 = M_0\hat{z}$. By neglecting terms quadratic in $\vec{h}$ and $\vec{m}$, we obtain the solution of the linearized equation of motion,

$$\overleftrightarrow{P} = \begin{pmatrix} \chi & i\kappa & 0 \\ -i\kappa & \chi & 0 \\ 0 & 0 & 0 \end{pmatrix} \tag{1.6}$$

$$\chi = \frac{\omega_M\omega_H}{\omega_H^2 - \omega^2} \tag{1.7}$$

$$\kappa = \frac{\omega_M\omega}{\omega_H^2 - \omega^2} \tag{1.8}$$

where $\omega_H = \gamma H_0$, $\omega_M = 4\pi\gamma M_0$, and $\overleftrightarrow{P}$ is the Polder tensor $\vec{m} = \overleftrightarrow{P}\,\vec{h}$ [52].

From (1.7), we notice the resonant absorption of electromagnetic energy at the frequency $\omega = \omega_H$ under the influence of a transverse magnetic field $\vec{h}$. This phenomenon is known as ferromagnetic resonance (FMR).

The solutions (1.6)–(1.8) describe the uniform precession ($|\vec{k}| = 0$) of $\vec{M}$ throughout the medium. For non-uniform precession, we must solve Maxwell's equations self consistently, due to the dipole field generated by $\vec{M}$, which includes contributions from $\vec{M}_0$ as well as the dynamic magnetization $\vec{m}$ [19]. Maxwell's equations for the dynamic electric field $\vec{e}(\vec{r},t)$, magnetic field $\vec{h}(\vec{r},t)$, and magnetization $\vec{m}(\vec{r},t)$ in a magnetic insulator with dielectric constant ϵ are

$$\nabla \cdot \vec{e}(\vec{r},t) = 0 \tag{1.9}$$

$$\nabla \times \vec{e}(\vec{r},t) = -\frac{1}{c}\frac{\partial}{\partial t}\left[\vec{h}(\vec{r},t) + 4\pi\vec{m}(\vec{r},t)\right] \tag{1.10}$$

$$\nabla \cdot \left[\vec{h}(\vec{r},t) + 4\pi\vec{m}(\vec{r},t)\right] = 0 \tag{1.11}$$

$$\nabla \times \vec{h}(\vec{r},t) = \frac{\epsilon}{c}\frac{\partial}{\partial t}\vec{e}(\vec{r},t), \tag{1.12}$$

which yield a wave equation for $\vec{h}(\vec{r},t)$,

$$\nabla^2\vec{h}(\vec{r},t) - \frac{\epsilon}{c^2}\frac{\partial^2}{\partial t^2}\vec{h}(\vec{r},t) = -4\pi\nabla\left[\nabla \cdot \vec{m}(\vec{r},t)\right] + 4\pi\frac{\epsilon}{c^2}\frac{\partial^2}{\partial t^2}\vec{m}(\vec{r},t). \tag{1.13}$$

In an unbounded medium, we may consider plane-wave solutions for $\vec{h}$ and $\vec{m}$,

$$\vec{h}(\vec{r},t) = \vec{h}_{\vec{k}} e^{i(\vec{k}\cdot\vec{r}-\omega_k t)} \tag{1.14}$$

$$\vec{m}(\vec{r},t) = \vec{m}_{\vec{k}} e^{i(\vec{k}\cdot\vec{r}-\omega_k t)} \tag{1.15}$$

and we obtain from (1.13) a relation between the amplitudes $\vec{h}_{\vec{k}}$ and $\vec{m}_{\vec{k}}$,

$$\vec{h}_k = -\frac{1}{k^2-k_0^2} 4\pi \vec{k}(\vec{k}\cdot\vec{m}_{\vec{k}}) + \frac{k_0^2}{k^2-k_0^2} 4\pi \vec{m}_{\vec{k}} \tag{1.16}$$

where k_0 is the wavenumber of an ordinary electromagnetic wave of frequency ω_k propagating in the medium $k_0 = \frac{\omega_k}{c}\sqrt{\epsilon}$. At microwave frequencies in specimens of practical interest, we find in nearly all cases

$$k >> k_0. \tag{1.17}$$

Thus (1.16) yields

$$\vec{h}_{\vec{k}} \approx -\frac{4\pi}{k^2}\vec{k}(\vec{k}\cdot\vec{m}_k) \tag{1.18}$$

for the dipole field $\vec{h}_{\vec{k}}$ associated with a propagating spin wave of wavevector $\vec{k}$ and amplitude $\vec{m}_k$. Approximation (1.17) constitutes the so-called "magnetostatic" approximation, since under (1.17) the contribution of the second term on the right-hand side of (1.16), due to electromagnetic propagation, is negligible.

The spectrum of spin waves in an unbounded medium was first obtained in macroscopic spin-wave theory by Herring and Kittel [10]. They considered the magnetization dynamics under an effective field including exchange fields $\propto q\nabla^2\vec{m}$ and the dipolar fields of the dynamic magnetization in the form of (1.18). They derived a dispersion relation for propagating spin waves,

$$\omega_k^2 = (\omega_H + \gamma q M_0 k^2)(\omega_H + \gamma q M_0 k^2 + \omega_M \sin^2\theta_k) \tag{1.19}$$

where θ_k is the polar angle between static magnetization $\vec{M}_0 \parallel \hat{z}$ and the spin-wave wavevector $\vec{k}$. As shown in Figure 1.1, the spin-wave dispersion exhibits several interesting characteristics. The spin-wave spectrum is gapped, with the minimal spin-wave frequency $\omega_H = \gamma H_0$ determined by the external applied field. The dipolar field of the dynamic magnetization introduces an anisotropy into the spin-wave spectrum of an otherwise isotropic ferromagnet: the spin-wave frequency depends on the relative direction of the static magnetization $\vec{M}_0$ and spin-wave wavevector $\vec{k}$. If we fix the magnitude

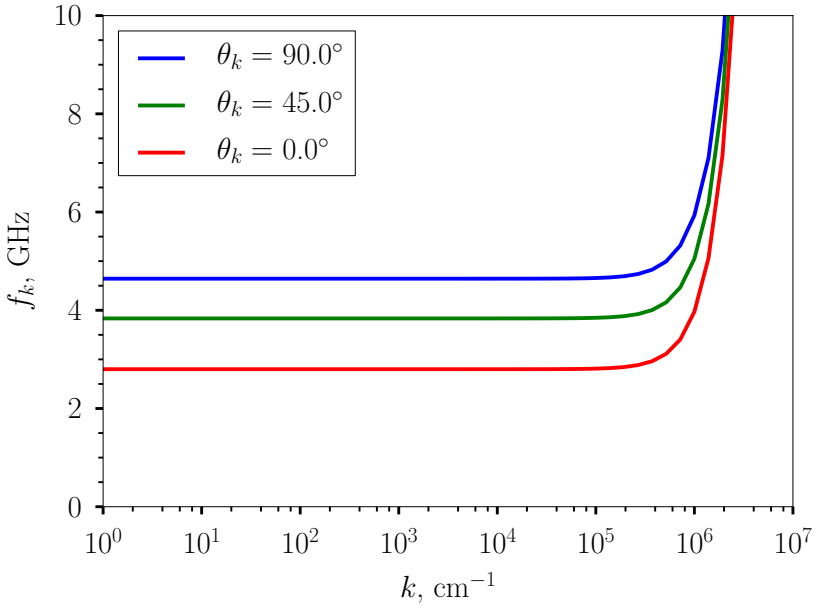

Figure 1.1: The bulk dispersion relation for spin waves in YIG at $H_0 = 1000$ Oe, $4\pi M_0 = 1750$ G, and $q = 3 \times 10^{-12}$ cm^2 for various propagation angles θ_k, calculated from (1.19).

of the spin-wave wavevector $|\vec{k}|$, then the maximum frequency corresponds to $\theta_k = 90°$, i.e propagation perpendicular to $\vec{M}_0$ while the minimum frequency corresponds to $\theta_k = 0°$ or propagation parallel to the magnetization. Moreover, in the limit $|\vec{k}| \to 0$, the dipole-dipole interaction becomes dominant (reflecting its long-range character) and the dispersion can be approximated via $\omega_{|\vec{k}|\to 0} \approx \sqrt{\omega_H(\omega_H + \omega_M \sin^2\theta_k)}$. In contrast, at large $|\vec{k}|$, the dispersion becomes quadratic, dominated by the exchange interaction $\omega_{|\vec{k}|\to\infty} \approx \gamma q M_0 k^2$.

From (1.19), it is evident that the frequency of the uniform mode $\omega_{|\vec{k}|=0}$ in an unbounded ferromagnet is not well-determined since the spectra corresponding to different orientations of the magnetization and spin-wave wavevector do not approach a unique limit as $|\vec{k}| \to 0$. This problem is removed in bounded specimen by imposing boundary conditions on the dynamic fields at the sample surface. Kittel [9] has derived the frequency of the uniform mode in an ellipsoidal ferromagnet,

$$\omega_{|\vec{k}|=0} = \sqrt{(\omega_H + \omega_M \frac{N_{11} - N_{33}}{4\pi})(\omega_H + \omega_M \frac{N_{22} - N_{33}}{4\pi})} \tag{1.20}$$

where the N_{ij} are the components of the demagnetization tensor $\overleftrightarrow{N}$. As seen from (1.20), $\omega_{|\vec{k}|=0}$ is unique and determined by the shape-dependent demagnetization tensor $\overleftrightarrow{N}$, together with H_0 and M_0.

Finally, we note that (1.3) does not account for energy dissipation. In order to account for dissipation, the most common approach is the addition of a phenomenological damping torque to the right-hand side of (1.3). The form most often used is due to Gilbert [53], who introduced a dimensionless damping parameter α leading to

$$\frac{\partial \vec{M}}{\partial t} = -\gamma \vec{M} \times \vec{H}_{eff} + \frac{\alpha}{M_0} \vec{M} \times \frac{d\vec{M}}{dt}. \tag{1.21}$$

The second term on the right-hand side corresponds to energy dissipation of the precessing magnetization, allowing it to relax into the direction of $\vec{H}_{eff}$. Other forms of the damping parameter are sometimes used, notably the form originally proposed by Landau and Lifshitz [7] as well as dissipative terms suggested by Bloch and Bloembergen [54]. It can be shown [50] that for small damping, the Gilbert and Landau-Lifshitz dissipation parameters are identical. In the present work, we adopt the Gilbert form, in order to facilitate comparison with previous work.

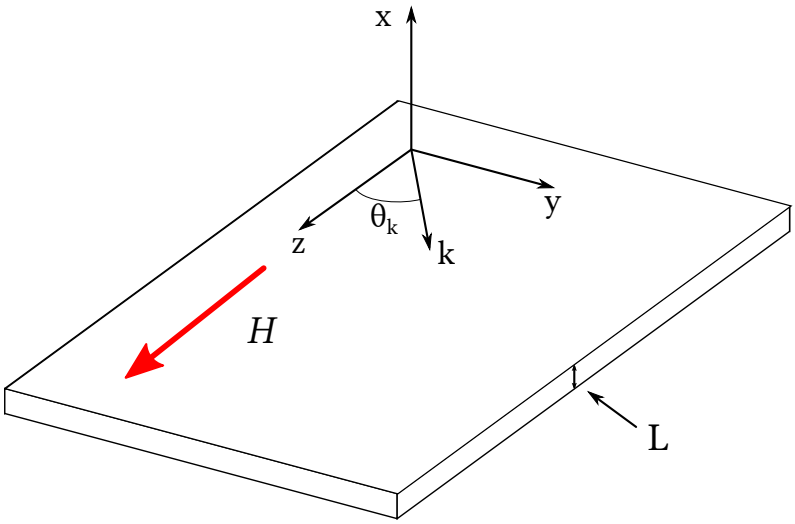

Figure 1.2: A schematic of the thin-film geometry of a film of thickness L and spin wave with in-plane wavevector k propagating at an angle θ_k to the z-axis. The film is considered unbounded in the $y-z$ plane.

1.2.2 Spin waves in thin ferromagnetic films

In this section, we present the theory of spin waves in thin ferromagnetic films. We consider only sample configurations for which the static magnetic field is applied in the plane of the film. We first discuss the theory for magnetostatic modes, i.e. dipolar spin waves [18–20]. Then we present the results of theory for dipolar-exchange spin waves [22].

Damon and Eshbach first obtained the magnetostatic modes of an in-plane magnetized thin ferromagnetic film [18]. In their approach, one starts by solving for the high-frequency magnetic susceptibility (1.6) from the linearized equation of motion. This tensor is used to solve Maxwell's equation in the magnetostatic approximation, which reduce to differential equations for the magnetic potential. This method yields a transcendental equation for the dispersion relation the magnetostatic modes.

In the magnetostatic limit, Maxwell's equations reduce to

$$\nabla \times \vec{H}_{eff} = 0 \tag{1.22}$$

$$\nabla \times \vec{B} = 0 \tag{1.23}$$

with the usual electrodynamic boundary conditions.

By applying the definitions (1.4) and (1.5), we obtain Ampere's and

Gauss' law for the dynamic magnetic field and magnetization,

$$\nabla \times \vec{h} = 0 \tag{1.24}$$

$$\nabla \cdot (\vec{h} + 4\pi\vec{m}) = 0. \tag{1.25}$$

Due to (1.24) we introduce a magnetic potential ψ such that $\vec{h} = \nabla\psi$, for which (1.25) becomes

$$\nabla^2\psi + 4\pi\nabla \cdot \vec{m} = 0. \tag{1.26}$$

Walker first study these equations in the the case of spheroid [12] and obtained an equation for the magnetic potential ψ,

$$(1+\chi)\left(\frac{\partial^2\psi}{\partial x^2} + \frac{\partial^2\psi}{\partial y^2}\right) + \frac{\partial^2\psi}{\partial z^2} = 0 \tag{1.27}$$

inside the medium, where χ is defined by (1.7). Outside the medium, the magnetic potential obeys Laplace's equation,

$$\nabla^2\psi = 0. \tag{1.28}$$

Damon and Eshbach studied (1.27) for the case of a ferromagnetic thin film, magnetized in the plane of the film as shown in Figure 1.2. By imposing the electromagnetic boundary conditions on ψ at the film surfaces, and matching the solutions inside the film from (1.27) and outside the film from (1.28), they obtained a relation between the spin-wave wavevector components and frequency. Their result may be written as

$$k_x^i = \pm k\sqrt{-\frac{1+\chi\sin^2\theta_k}{1+\chi}} \tag{1.29}$$

$$k_x^e = k \tag{1.30}$$

$$k_x^{e\,2} + 2k_x^e k_x^i(1+\chi)\cot k_x^i L - k_x^{i\,2}(1+\chi)^2 - \kappa^2 k^2\sin^2\theta_k = 0, \tag{1.31}$$

where k_x^i and k_x^e denote the x-component of the wave vector internal and external to the film, L is the film thickness, $k = \sqrt{k_z^2 + k_y^2}$ is the magnitude of the in-plane wavevector, θ_k is the in-plane angle between $\vec{k}$ and $\vec{M}_0 \parallel \hat{z}$, and χ and κ are defined in (1.7) and (1.8). Together, (1.29)–(1.31) yield a transcendental dispersion equation connecting the mode frequency, in-plane wave number k, and in-plane propagation angle θ_k.

In their given form, the results of Damon and Eshbach are difficult to analyze and must be solved with numerical methods. However, a few salient

features of the modes can be recognized. The sign of the quantity under the square root in (1.29)

$$-\frac{1+\chi\sin^2\theta_k}{1+\chi} \tag{1.32}$$

determines whether the transverse wave vector inside the film is real or imaginary, corresponding to sinusoidal or decaying exponential distribution of the amplitude of the dynamic magnetization in the transverse direction, respectively. We rewrite (1.32) as

$$\frac{\omega^2-\omega_H(\omega_H+\omega_M\sin^2\theta_k)}{\omega_H(\omega_H+\omega_M)-\omega^2}, \tag{1.33}$$

which is positive in the frequency range,

$$\omega_H(\omega_H+\omega_M)>\omega^2>\omega_H(\omega_H+\omega_M\sin^2\theta_k). \tag{1.34}$$

For fixed H_0, M_0, and ω, the sign of expression (1.32), i.e. the transverse profile of the dynamic magnetization, is determined entirely by the in-plane propagation angle θ_k. The frequency band defined by (1.34) corresponds to real values of k_x^i, or sinusoidal dependence of the dynamic magnetization throughout the volume, and are termed volume modes. This result suggests that surface modes, for which k_x^i is imaginary, may exist at all frequencies outside the volume mode frequency band. In fact, further analysis [19] shows that surfaces modes below the bottom of the frequency band, for which $\omega<\omega_H(\omega_H+\omega_M\sin^2\theta_k)$, do not exist. It can be shown [19] that the surface mode frequency band is given by

$$\omega_H(\omega_H+\omega_M)+\frac{(\omega_M\sin^2\theta_k-\omega_H\cos^2\theta_k)^2}{4\omega_M^2\sin^2\theta_k}>\omega^2>\omega_H(\omega_H+\omega_M) \tag{1.35}$$

under the condition $\theta_k>\theta_s=\arctan\sqrt{\frac{\omega_H}{\omega_M}}$. Thus, we see that the magnetostatic spin-wave spectrum is defined by two complimentary mode types, volume and surface modes, with frequency bands intersecting at the Kittel frequency, which for in-plane magenetized thin films is given by $\omega_{|\vec{k}|=0}=\sqrt{\omega_H(\omega_H+\omega_M)}$. Since the surface modes were a novel result of spin-wave spectra in bounded ferromagnets, these modes are sometimes referred to as "Damon-Eshbach" modes.

The study of spin waves in thin ferromagnetic films under the influence of dipole-dipole and exchange interactions was later carried out by several researchers [21–25]. The presence of the exchange field, quadratic in derivatives of $\vec{M}$ requires additional boundary conditions for the dynamic magnetization

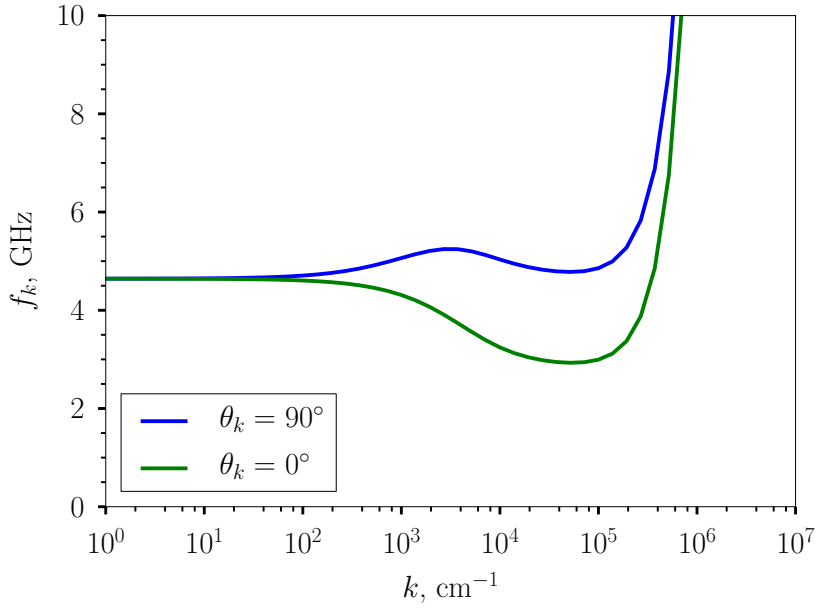

Figure 1.3: The dispersion of dipolar-exchange spin waves in a 5.1 μm thick YIG film for $H_0 = 1000$ Oe, $4\pi M_0 = 1750$ G, $q = 3 \times 10^{-12}$ cm^2, and in-plane propagation angle θ_k, calculated from (1.36) in the $n = 0$ approximation.

$\vec{m}_{\sim}$, so-called exchange boundary conditions, at the sample boundaries reflecting the fact that the precession of spins at boundaries depends strongly on the degree of surface anisotropy present in the system [16, 55]. Kalinkos and Slavin [22] have derived a particularly simple expression for the dispersion relation of dipole-exchange spin waves in a thin ferromagnetic film subject to arbitrary exchange boundary conditions, magnetized in the plane of the film:

$$\omega_n^2 = (\omega_H + q\omega_M k_n^2)(\omega_H + q\omega_M k_n^2 + \omega_M F_{nn}) \tag{1.36}$$

where

$$F_{nn} = 1 - P_{nn}\cos^2\theta_k + \omega_M \frac{P_{nn}(1 - P_{nn})\sin^2\theta_k}{(\omega_H + q\omega_M k_n^2)}, \tag{1.37}$$

θ_k is the angle of the in-plane wavevector $\vec{k}$ to the static magnetization $\vec{M}_0$, $k_n^2 = k^2 + \kappa_n^2$, and $\kappa_n = \frac{n\pi}{L}$ where L is the film thickness. The dispersion relation for the pure volume ($\theta_k = 0°$) mode and pure surface ($\theta_k = 90°$) mode is plotted in Figure 1.3.

In the approximation of totally unpinnned surface spins, P_{nn} has the explicit expression

$$P_{nn} = \frac{k^2}{k_n^2} - \frac{k^4}{k_n^4} F_n \frac{1}{(1 + \delta_{0n})} \tag{1.38}$$

whereby

$$F_n = \frac{2}{kL}[1 - (-1)^n e^{-kL}]. \tag{1.39}$$

In this approximation, we have assumed that the transverse distribution of the magnetization across the film thickness is uniform ($n = 0$) or harmonic ($n \neq 0$), which is obviously a poor approximation for surface modes ($\theta_k > \theta_s$). However, for sufficiently thin films, the distribution of the magnetization across the film thickness can, to a good approximation, for both volume and surface modes be considered uniform for a wide range of in-plane wavevectors ($|\vec{k}|L << 1$).

1.2.3 Caustics

In this and the next section, we discuss peculiarities of the spin-wave dispersion in thin ferromagnetic films. From (1.36) and (1.37) it is evident that the spin-wave dispersion depends on the angle θ_k between the in-plane wavevector and the external applied field. In fact, for magnetostatic waves ($q \to 0$), this angular dependence may result in the formation of so-called caustic wave beams [56]. In this case, the local excitation of spin waves in an unbounded medium results in an angular confinement of the energy flow at an angle θ_c relative to the external applied field.

Analogous effects have been previously observed for phonons propagating in an anisotropic crystal [57–59]. Utilizing a heat pulse as an incoherent point source of ballistic phonons, an angular confinement of the energy flux of acoustic phonons in single crystal Ge was observed [59]. Theoretically, it was found that the energy flux into a given direction of phonons excited at angular frequency ω_p is inversely proportional to the curvature of the iso-frequency surface in reciprocal space [57, 58]. The elastic anisotropy deforms this surface into a nonspherical shape, introducing a noncollinearity between the phase $v_{ph} = \frac{\omega(\vec{k})}{|\vec{k}|}$ and group $v_g = \nabla_{\vec{k}}\omega(\vec{k})$ velocity of the phonons. Energy of an elastic wave is transported parallel to the direction of the group velocity. Therefore, the phonon energy flux is concentrated along directions for which the Gaussian curvature of the iso-frequency surface is small, or vanishes, corresponding to a large number of phonons with various phase velocities and nearly equal (small curvature) or equal (vanishing curvature) group velocities. Terminologically, the wave beams formed in directions corresponding to vanishing curvature of the iso-frequency surface are called caustics. These directions need not coincide with the crystal symmetry axes, since the curvature of the iso-frequency surface is determined by the ratio of the elastic constants of the medium.

Such an approach is also applicable to spin waves propagating in ferromagnetic thin films [60]. More than a decade ago [61], the study of the diffraction of spin-waves in in-plane magnetized YIG films by means of BLS revealed that the scattering of spin waves from a point defect resulted in the angular confinement of the spin wave energy flux along directions at an angle θ_c with respect to the externally applied magnetic field. Recently, it has been shown that the radiation of spin-waves from a one-dimensional wave source in YIG, actually a patterned waveguide contacting a large film, may result in the formation of non-diffractive wave beams along the critical directions [62]. The radiation of caustic beams from a decaying, strongly-localized spin wave packet (a so-called spin wave "bullet") was also experimentally observed [63]. Similar studies have been carried out in Py. The radiation of spin waves from a waveguide, excited by a microstip antenna, into an unbounded Py film [64], as well as the diffraction of spin-waves from a defect within a waveguide [65], were experimentally observed. In addition, the excitation of semicaustic beams in Py by a Cu coplanar waveguide was experimentally observed by means of SKEM [46]. Finally, the radiation of spin-waves from a spin torque nano-oscillator (STNO) contacting an unbounded Py film was experimentally studied and exhibited a directionality controllable by the external magnetic field [38].

Similar to phonon propagation in anisotropic crystals, the directional

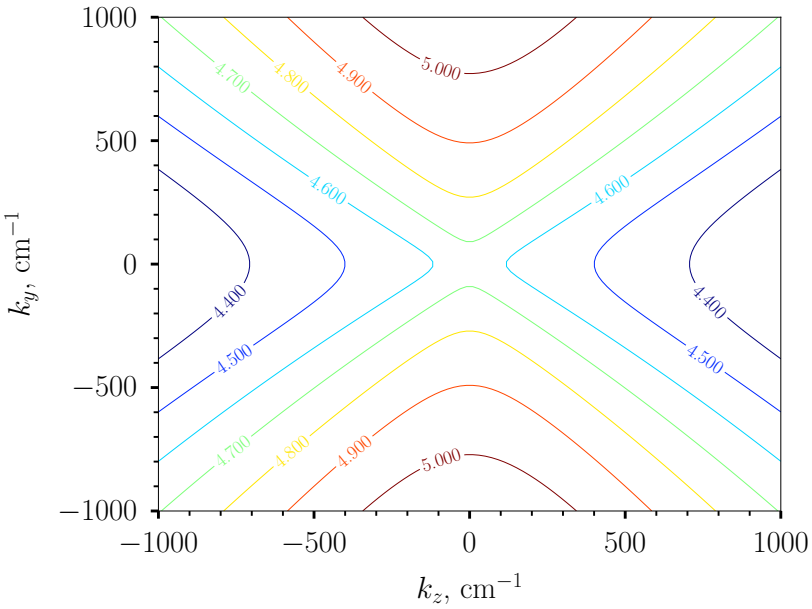

Figure 1.4: Iso-frequency curves of a 5.1 μm thick YIG film calculated from (1.36) for magnetostatic waves ($q \to 0$), at frequencies as labeled. The external field $H_0 = 1000$ Oe and the saturation magnetization $4\pi M_0 = 1750$ G, and we assume uniform magnetization profile across the film thickness ($n = 0$). With these parameters, the frequency of the uniform precession mode is 4.64 GHz.

character of these effects may be explained by considering the curvature of the iso-frequency curves for magnetostatic waves (in the case of magnetostatic waves in thin films, in the $n = 0$ approximation, the dimensionality is reduced and the relevant cross sections in reciprocal space are curves).

We consider the physical quantities ω_H, ω_M, q, and L to be fixed. For simplicity, we assume the film is sufficiently thin ($|\vec{k}|L << 1$) such that the $n = 0$ approximation (uniform distribution of spin-wave amplitude across film thickness) can be applied in a wide range of in-plane wavevectors $|\vec{k}|$. Then, equation (1.36) defines a two-dimensional spin-wave dispersion surface $\omega = \omega_{n=0}(\vec{k})$.

The points on this surface represent the plane waves $e^{i\vec{k}\cdot\vec{r}}e^{i\omega(\vec{k})t}$ which satisfy the systems of equations. If we consider localized excitation by a sinusoidal dynamic magnetic field at frequency $f_{ex} = \frac{\omega_{ex}}{2\pi}$, the excited wave packet is synthesized from plane waves lying on the isofrequency contour defined by $\omega_{n=0}(\vec{k}) = \omega_{ex}$. These plane waves have phase velocity $\vec{v}_{ph} = \frac{\omega_{n=0}(\vec{k})}{\vec{k}}$ and

group velocity $\vec{v}_g = \nabla_{\vec{k}}\omega_{n=0}(\vec{k})$, which defines the direction of energy propagation and is oriented normal to the isofrequency curve. For fixed excitation frequency, the problem may be reformulated in one-dimension, with the isofrequency curve, shown in Figure 1.4 for YIG, defined by $k_z = k_z(k_y, \omega_{ex})$. The curvature of the isofrequency curve vanishes at points

$$\frac{d^2k_z}{dk_y^2} = 0 \tag{1.40}$$

which designates linear regions of the isofrequency curve in the $k_y - k_z$ plane, i.e. sets of plane waves with parallel $\vec{v}_g$. At these points, caustic beams are formed with wavevector $\vec{k}_c$.

Lastly, we note that the size of the wave source and spectrum of the excitation field determine the conditions and character of the caustic wave beam. A wave source of finite size efficiently excites plane waves for which $|\vec{k}| < \frac{\pi}{r}$ where r is the radius of a circular wave source. If $|\vec{k}_c| > \frac{\pi}{r}$, a caustic beam will not form [62]. If the spectrum of the excitation field is supported at many frequencies, as can be expected for current-induced magnetization dynamics, the resultant wave packet is synthesized from plane waves lying on many isofrequency curves. If the excitation field spectrum is not too broad, the wave packet may exhibit directional characteristics, but can be expected to have a broad spatial profile, demonstrated experimentally for an elliptical wave source driven by spin-transfer torque in [38]. We note that the detection of caustic beams in thin ferromagnetic films confined in the in-plane directions first occurred in the experiments presented in chapter 3.

1.2.4 Lateral confinement

In the previous sections, we have presented the macroscopic spin-wave theory for unbounded ferromagnetic media and thin ferromagnetic films, i.e. ferromagnets confined in a single direction. Lithographical advances in recent decades have enabled the fabrication of thin film samples with in-plane dimensions sufficiently small to result in lateral confinement in a single in-plane dimension (stripes) [66–70] or both in-plane dimensions (rectangular platelets) [71–75].

These studies have shown that lateral confinement results in two effects under linear excitation, depending on the dimension of confinement and orientation of the external applied magnetic field [76]. In wires magnetized along the length, the principle result of lateral confinement is the quantization of the in-plane wavevector along the width of the wire [66,67]. In wires magnetized along the width, strong demagnetizing effects create regions near the

wire edge of highly reduced internal field [68–70]. This spin-wave well allows the excitation of localized spin-wave modes, so-called edge modes. In rectangular platelets magnetized to saturation, both effects are present [71–74].

Consider a wire of width w and length l such that $\frac{w}{l} << 1$. Align the wire length along the z-axis, so that the x-axis is directed normal to the wire surface. This geometry corresponds to a thin film confined along one-dimension, here along the y-axis, along the wire's width.

In the first case, if the external magnetic field is applied parallel to the z-axis, static demagnetizing effects are not appreciable. It has been shown [77], however, that excitation of the magnetization results in dynamic dipolar fields near the edge of the wire. These dipolar fields are inhomogeneous and lead to so-called dipolar pinning, which causes spin-wave quantization of the wavevector component along the width of the stripe. In [77] it has been shown, that the discrete frequencies of the spin-wave modes are given by

$$\omega_m^2 = \omega_H(\omega_H + \omega_M) + \omega_M^2 \frac{\pi(2m-1)}{4} p \tag{1.41}$$

where $m = 1, 2, 3, \cdots$ indexes the quantized wavevector along the strip width and $p = \frac{L}{w} << 1$ is the stripe aspect ratio.

If the external magnetic field is applied along the wire's width, parallel to the y-axis, static demagnetizing effects create a strongly inhomogeneous internal field along the wire's width. The inhomogeneous internal field along the wire width may be calculated according to [78]

$$H_i(y) = H_0 - N_{yy}(y) \times 4\pi M_0 \tag{1.42}$$

where

$$N_{yy}(y) = \frac{1}{\pi} \times \left[\arctan \frac{L}{2y+w} - \arctan \frac{L}{2y-w} \right]. \tag{1.43}$$

In Figure 1.5, we plot the internal field for a Py stripe, magnetized parallel to its width.

To understand the spin-wave localization, we consider (1.36) for a spin wave propagating parallel to the wire width, which corresponds to $\theta_k = 0$. With $\omega_H(y) = \gamma H_i(y)$ and a uniform spin-wave profile across the wire thickness ($n = 0$), (1.36) becomes

$$\omega_{n=0}^2(y) = \left[\omega_H(y) + q\omega_M k^2\right] \left[\omega_H(y) + q\omega_M k^2 + \frac{\omega_M}{kL}(1 - e^{-kL})\right]. \tag{1.44}$$

In Figure 1.6, we plot the spin-wave dispersion at several points along the wire width due to the inhomogeneous internal field. If the wave propagates through the region of inhomogeneous internal field, from the edge region

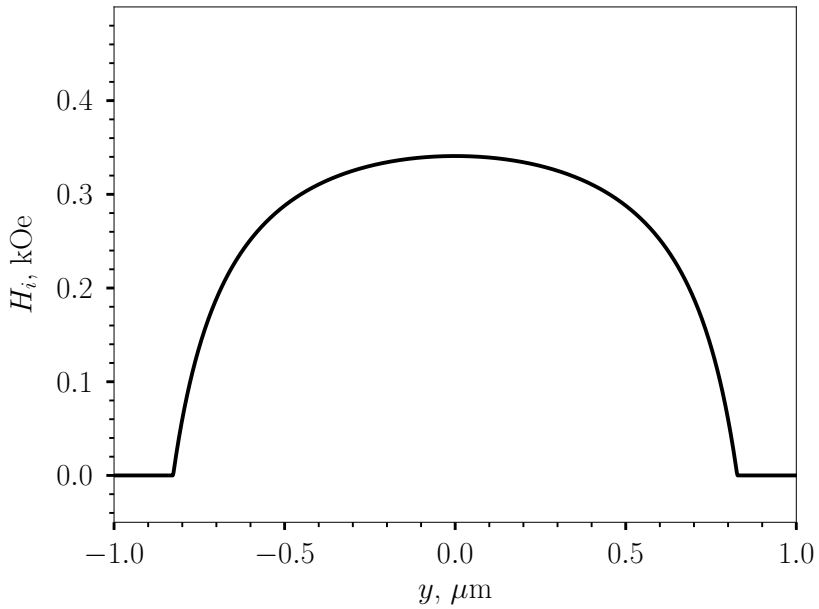

Figure 1.5: The value of the internal magnetic field H_i as a function of the the coordinate y along the wire width w in a 2 μm wide wire magnetized along its width ("transversely magnetized wire") as calculated from (1.42). The external applied field $H_0 = 0.5$ kOe, the wire thickness $L = 50$ nm, and the saturation magnetization of Py is taken as $4\pi M_0 = 10000$ G. The maximum value of the internal field at $y = 0$ is $H_i = 0.34$ kOe.

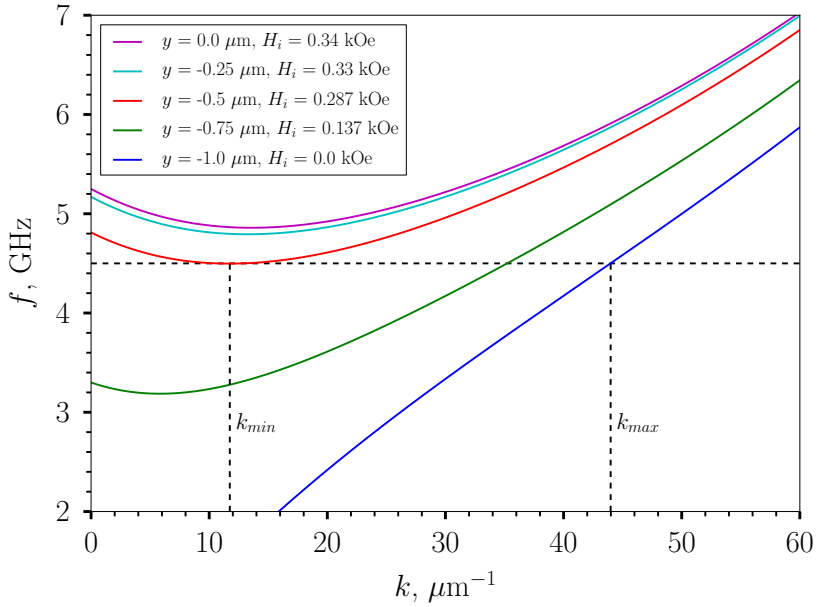

Figure 1.6: The local dispersion relation in a transversely magnetized Py wire, as function of transverse coordinate y. The parameters and internal field are the same as in Figure 1.5. A spin wave excited in the edge region ($H_i = 0$) at 4.5 GHz with wavevector k_{max} propagates towards the center of the wire, adjusting its wave vector until reaching k_{min} at $y = -0.5$ μm, corresponding to the maximum field value $H_i = 0.287$ kOe for which a plane wave state exists at 4.5 GHz. The wave is reflected, contributing to the formation of a mode localized at the transverse wire edges.

to the center, the wavevector changes continuously $k = k(y)$ to satisfy the dispersion relation $\omega_{n=0}(k(y), \omega_H(y))$ [79]. The spin wave will be reflected, however, at the point where the internal field increases sufficiently such that no solution of the dispersion equation (1.44) with real k exists. The spin wave therefore becomes localized in the edge region.

In rectangular platelets, both affects modify the spin-wave spectrum. It has been shown [80] that the quantization can be accounted by decomposing the two-dimensional spin-wave profile into quantized one-dimensional distributions—one corresponding to a wire magnetized along its length, the other along its width. We note that, while the formation of edge modes follows the same principles as in wires, the actual profile of the internal field must be numerically calculated, hindering analytic analysis.

1.3 Current-induced magnetization dynamics

In the following sections, we introduce the concepts and results necessary for the interpretation of experimental results on current-induced magnetization dynamics. First, we address the thermal magnetization fluctuations in a thin ferromagnetic film. Next, we introduce the concept of spin-transfer torque and discuss its origins in simple structures. Finally, we discuss the spin Hall effect, which is used as a means of spin-current creation in the second series of experiments in this work.

1.3.1 Thermal magnetization fluctuations in thin films

In this section, we address the thermal magnetic fluctuations in a thin ferromagnetic film. We discuss the character and importance of these fluctuations in devices applications. Finally, we present the fluctuation-dissipation theorem (FDT) in its specific form for thin ferromagnetic films.

In the foregoing, we have considered coherent magnetization dynamics in thin ferromagnetic films, i.e. the linear response theory of the magnetization due to a dynamic magnetic field. Here, we address incoherent magnetization dynamics in thin ferromagnetic films. The spectrum of thermal magnetization fluctuations in thin ferromagnetic films is a problem of great technological interest, since these fluctuations determine the obtainable signal-to-noise ratio of thin-film magnetoresistive devices used as read sensors in magnetic storage systems [81].

A giant magnetoresistance (GMR) sensor comprises a thin-film element magnetized to saturation (single magnetic domain) in the plane of the element. Thermal agitation results in the excitation of spin-wave modes, which appear as peaks in the spectrum of magnetic noise. Their frequencies are determined by the magnetic material, the in-plane shape of the thin-film, and the bias field. If the spectrum of the magnetic flux read by the sensor is supported at any of the frequencies of the thermal spectrum peaks, the sensor exhibits undesired ringing, which places an upper bound on the operation frequency [82, 83].

If we wish to study incoherent magnetization dynamics due to thermal magnetic fluctuations, we may apply the fluctuation-dissipation theorem [84, 85], which states a general relationship between the power spectral density of fluctuations and the dissipation obtained in linear response theory. In order to solve for the linear response of the system with dissipation when the thermal energy $k_B T$ is much smaller than the microscopic exchange energy, we consider the Landau-Lifshitz-Gilbert equation of motion for the

magnetization,

$$\frac{\partial \vec{M}}{\partial t} = -\gamma \vec{M} \times \vec{H}_{eff} + \frac{\alpha}{M_0} \vec{M} \times \frac{d\vec{M}}{dt}. \tag{1.45}$$

where α phenomenologically models the dissipation and we have assumed that the damping is isotropic (corresponding to scalar α). We wish to consider the linear response of the uniform precession mode in a thin ferromagnetic film to an external magnetic field $\vec{h}_e$. For an in-plane magnetized thin ferromagnetic film considered as a limiting case of an ellipsoid, the demagnetizing tensor $\overleftrightarrow{N}$ has components $N_{xx} = 4\pi$, $N_{ij} = 0$ otherwise. Solving the linearized version of (2.2) with $\vec{H}_{eff}$ comprising the external fields and dipolar fields, we obtain the dynamic susceptibility $\overleftrightarrow{\chi}$:

$$\overleftrightarrow{\chi} = \begin{pmatrix} \chi'_{xx} - i\chi''_{xx} & \chi'_{xy} - i\chi''_{xy} & 0 \\ \chi'_{yx} - i\chi''_{yx} & \chi'_{yy} - i\chi''_{yy} & 0 \\ 0 & 0 & 0 \end{pmatrix} \tag{1.46}$$

$$\chi'_{xx} = \frac{\omega_M}{D} \left[\omega_H J + 2\left(\alpha\omega\right)^2 \omega_1\right] \tag{1.47}$$

$$\chi''_{xx} = \frac{\omega_M \omega}{D} \left[2\alpha\omega_1\omega_H - \alpha J\right] \tag{1.48}$$

$$\chi'_{xy} = -\chi'_{yx} = \frac{\omega_M}{D} \left[2\alpha\omega_1\omega^2\right] \tag{1.49}$$

$$\chi''_{xy} = -\chi''_{yx} = \frac{\omega_M \omega}{D} \left[-J\right] \tag{1.50}$$

$$\chi'_{yy} = \frac{\omega_M}{D} \left[\omega_H J + 4\pi\omega_M J + 2\left(\alpha\omega\right)^2 \omega_1\right] \tag{1.51}$$

$$\chi''_{yy} = \frac{\omega_M \omega}{D} \left[2\alpha\omega_1\omega_H + 8\pi\omega_M\alpha\omega_1 - \alpha J\right], \tag{1.52}$$

where

$$\omega_0 = \sqrt{\omega_H\left(\omega_H + 4\pi\omega_M\right)} \tag{1.53}$$

$$\omega_1 = \omega_H + 2\pi\omega_M \tag{1.54}$$

$$J = \omega_0^2 - \left(1 + \alpha^2\right)\omega^2 \tag{1.55}$$

$$D = J^2 + 4\alpha^2\omega^2\omega_1^2. \tag{1.56}$$

Applying the fluctuation dissipation theorem for thin ferromagnetic films [86–88], we obtain a relationship between the power spectral density $S_{m_i m_i}(\omega)$ of the fluctuating magnetization component m_i at frequency ω to the dissipative part of the linear response $\chi_{ij}(\omega)$,

$$\overleftrightarrow{S}_{\vec{m}\vec{m}}(\omega) = \begin{bmatrix} S_{m_x m_x}(\omega) & S_{m_x m_y}(\omega) \\ S_{m_y m_x}(\omega) & S_{m_y m_y}(\omega) \end{bmatrix} = \frac{4k_B T}{\gamma M_0 V} \frac{1}{\omega} \begin{bmatrix} \chi''_{xx}(\omega) & \frac{1}{i}\chi'_{xy}(\omega) \\ \frac{1}{i}\chi'_{yx}(\omega) & \chi''_{yy}(\omega) \end{bmatrix} \tag{1.57}$$

where k_B is the Boltzmann constant, T the temperature, and V the volume of the element (considered bounded in the y–z plane). With this relationship, we may study the spectrum of magnetization fluctuations by performing linear response measurements, e.g. by investigating the ferromagnetic resonance.

1.3.2 Spin-Transfer Torque

The interplay between spin transport and magnetization, a collective property of the electrons, plays a central role in spin-based electronic devices such as magnetic memory and sensors. Operation of these devices relies on the dependence of their electronic properties on the magnetic configuration due to the magnetoresistance [89, 90] or, conversely, on the ability to electrically control their magnetic configuration by the current [91]. The effect of current on the magnetic configuration results from the modification of the dynamical properties of nanomagnets by the spin transfer torque (STT) [92, 93].

In this section, we introduce the concept of STT. We establish the spin filter effect of a ferromagnet, then discuss current-induced magnetization dynamics in a ferromagnet-nonmagnet-ferromagnet trilayer system. In doing so we address STT, and illustrate its quantum mechanical origins. Finally, we discuss the experimental results concerning the effect of STT on the magnetization dynamics of a thin ferromagnetic film/layer.

The interest in current-induced magnetization dynamics derived from the discovery of giant magnetoresistance (GMR) by Grünberg and Fert [89, 90]. In particular, in the current perpendicular to the plane (CPP) geometry [94] of a GMR device, Berger [93] and Slonczewski [92] predicted that the electric current may achieve switching of the magnetization direction of one of the ferromagnetic layers in the ferromagnet-nonmagnet-ferromagnet stack. The STT-induced switching process in these structures relies on the spin-filter effect of a conducting ferromagnet.

Spin filtering in ferromagnets can be explained by spin-dependent transmission and reflection at ferromagnet-nonmagnet interfaces, as well as by spin-dependent scattering by defects or impurities in the ferromagnet. In the following, we limit our focus to transition metal ferromagnets and their alloys. The actual electronic band structure of such ferromagnets is complex, and theoretically approachable by quantum mechanical calculations only in certain approximations. It is found, however, that the salient features of the band structure responsible for spin filtering, and thus the device physics of GMR sensors as well as STT, may be explained by means of a greatly simplified picture of the electronic band structure in these materials.

If we assume the simple $s-d$ model [95] for a transition metal ferromag-

net, we consider conduction electrons to fill the delocalized s states while the d states describe non-itinerant, localized states. The simplest origin of spin filtering occurs in this picture, for which the strength of scattering from impurities and defects for majority and minority states is siginificantly different. Hereby, transmission of an unpolarized electron current through the ferromagnet results in preferential scattering of the majority/minority itinerant s-electrons into localized d states, which results in a corresponding spin polarization of the current due to excess minority/majority itinerant electrons. Such effects may partially explain the spin polarization of electronic currents in thin film Fe layers [96].

If we consider spin filtering in structures containing a single ferromagnet, we may observe appreciable STT in layers much thicker than the spin diffusion length. If we instead consider a structure consisting of two thin ferromagnets separated by a nonmagnetic spacer layer F1/N/F2, we may address the effects of a spin-polarized current on the dynamics of the ferromagnetic layers. The quantization axis in a ferromagnet is defined by the static magnetization direction. If we consider a CPP structure, in which both ferromagnets are magnetized in-plane, with an angle θ between the two static magnetization directions, then we may investigate the transfer of angular momentum between F1 and F2 due to electric current polarized along the quantization axis of F1 incident at the N/F2 interface.

To elucidate the physical mechanism of this angular momentum transfer, we consider F1 to act as a spin filter along its quantization axis, and we approximate the band structure of F2 by the free electron Stoner model [97]. In this model, the electrons are described by the dispersion of free electrons, with a exchange-induced shift of the spin-up electrons relative to spin-down electrons. We consider a simplified model for STT due to Stiles and Ralph [91], in which we consider a spin current incident at the N/F2 interface, where electrons experience a spin-dependent potential barrier equal to the exchange splitting Δ. For a single electron, the spin current density $\overleftrightarrow{Q}$ may be written

$$\overleftrightarrow{Q} = \frac{\hbar^2}{2m} \mathrm{Im}\left(\psi^* \vec{\sigma} \otimes \nabla \psi\right) \tag{1.58}$$

where $\vec{\sigma}$ represents the Pauli matrices, m is the free electron mass, and ψ is the single-electron wavefunction.

Stiles and Ralph [91] have shown that the corresponding spin current

densities are given by

$$\overleftrightarrow{Q}_{in} = \frac{\hbar^2}{2m\Omega}\left[k_\uparrow \sin\theta\hat{x} + k_\uparrow \cos\theta\hat{z}\right] \tag{1.59}$$

$$\overleftrightarrow{Q}_{trans} = \frac{\hbar^2}{2m\Omega}k_\uparrow \sin\theta\cos\left[(k_\uparrow - k_\downarrow)x\right]\hat{x} \tag{1.60}$$

$$- \frac{\hbar^2}{2m\Omega}k_\uparrow \sin\theta\sin\left[(k_\uparrow - k_\downarrow)x\right]\hat{y} \tag{1.61}$$

$$+ \frac{\hbar^2}{2m\Omega}\left[k_\uparrow \cos^2\frac{\theta}{2} - k_\downarrow\left(\frac{2k_\uparrow}{k_\uparrow + k_\downarrow}\right)^2 \sin^2\frac{\theta}{2}\right]\hat{z} \tag{1.62}$$

$$\overleftrightarrow{Q}_{refl} = \frac{\hbar^2}{2m\Omega}k_\uparrow\left(\frac{k_\uparrow - k_\downarrow}{k_\uparrow + k_\downarrow}\right)^2 \sin^2\frac{\theta}{2}\hat{z}. \tag{1.63}$$

where $k_\uparrow = k$ the wavevector of the incident electron, $k_\downarrow = \frac{1}{\hbar}\sqrt{2m(E-\Delta)} < k$, and Ω represents the wavefunction normalization volume.

These results of the simplified model illustrate the basic microscopic mechanisms of STT from a spin current incident at the N/F2 interface. From (1.63), the transverse spin component of the reflected spin current vanishes, i.e. the transverse ($\hat{x}$ and $\hat{y}$) spin component is completely transmitted. The microscopic mechanism assumed responsible for the transfer of this component of the spin current density into the spin system of F2 is dephasing. Due to the exchange splitting in F2, the up and down spin components of the transmitted spin current density for a given energy E have different kinetic energies, resulting in precession of the spin current density about the exchange field in F2. It is found that, in first principles calculations, summing states over the Fermi surface corresponding to a broad directional distribution of incident electrons results in dephasing, deconstructive interference, of the transverse spin components of the spin current density within on the order of a few atomic spacings in F2 [98]. In this way, the spin current density transfer angular momentum from F1 to F2.

Experimental results have confirmed the possibility of STT to induce magnetization reversal as well as spin-wave emission. After the prediction of STT in magnetic multilayers [92, 93], the first experimental confirmation of STT came from measurements of current-induced resistance changes in a magnetic multilayer [99]. Several years later, it was experimentally confirmed [32] that STT may induce microwave oscillations in ferromagnetic layers. Recently, electrical measurements of the magnetization noise spectrum yielded measurements of the thermally-activated ferromagnetic resonance due to STT [100]. In the measurements of chapter 5, we present optical measurements in STT-driven spin systems.

1.3.3 Spin Hall Effect

STT phenomena may arise from the transfer of spin angular momentum of conduction electrons to a ferromagnetic layer. It is not essential, however, that the spin current be accompanied by electrical current, and we may formally consider the STT generated by a pure spin current. In our experiments, such a torque can originate from the spin Hall effect [101, 102] in the bulk of Pt producing a spin current at the interface with the Py disk [103–105].

In this section, we discuss the origins of the spin Hall effect (SHE) in metals. We focus our attention on the SHE in non-magnetic metal electrodes adjacent to ferromagnetic layers. We discuss the microscopic origin of a spin current due to Mott scattering of electrons in the presence of strong spin-orbit coupling the non-magnetic electrode, the so called extrinsic SHE.

The theoretical prediction of the spin Hall effect [101, 102] considered the multiple scattering of electrons in a non-magnetic (semi-)conductor with appreciable spin-orbit coupling. The spin-dependent scattering results in the spatial separation of electrons with different spin orientations from a beam of unpolarized electrons, producing a spin-current density perpendicular to the electron motion.

Later, it was predicted that a transverse spin-current density may arise in non-magnetic systems due to the relativistic band structure in certain (semi-)conductors [106, 107]. The spin Hall effect was first observed by optical detection in GaAs samples [108, 109]. Interestingly, the two papers attribute their observations to the intrinsic [109] and extrinsic [108] spin Hall effect, respectively. An extensive literature treats the intrinsic/extrinsic origin of the SHE in various non-magnetic systems [110]. Here, we are concerned primarily with the experimental fact of the generation of a transverse spin-current density from an electric current in paramagnetic conductors.

The discovery of the SHE in semiconductors was followed by the demonstration of the inverse spin Hall effect (iSHE) in metals by injection of spin-polarized electric currents from ferromagnetic contacts due to the spin-filter effect [111]. In these experiments, it was found, that an incident spin-current density in a non-magnetic material exhibiting the spin Hall effect results in a reciprocal effect—the generation of an electric current transverse to the incident spin-current density. It soon followed, that a single-layer paramagnetic conductor may be used as a spin-wave transducer for microscopic transition metal ferromagnets [103–105, 111–114].

These experiments study STT generated by the SHE or, conversely, electric voltage generated by the iSHE due to spin pumping. Spin pumping [115] refers to the reciprocal effect of STT—the emission from a precessing ferromagnetic layer of a spin-current density into adjacent non-magnetic lay-

ers [116]. The conversion of a spin-pumping induced spin current density into an electric current by the iSHE was first observed in [111]. In a Py/Pt bilayer, a microwave frequency magnetic field excited ferromagnetic resonance in the Py layer, inducing a spin-current density in a Pt, a paramagnetic conductor with strong spin-orbit coupling. The iSHE generated a voltage at the transverse sides of the Pt layer, which was measured in experiment.

Thereafter, experiments on a Py/Pt bilayer device showed that STT from the SHE-induced spin-current density could enable electric control of the ferromagnetic characteristics in Py [103].

Chapter 2

Experimental Techniques

2.1 Magnetization Excitation

In this section, we discuss two techniques, ferromagnetic resonance and parallel pumping, used to excite the dynamic magnetization in our experiments. We establish the basic theoreticals results of each technique, necessary for the interpretation of experiments.

2.1.1 Ferromagnetic resonance

The excitation of ferromagnetic resonance in magnetic specimens yields valuable information with respect to the magnetic parameters and relaxation rates. This technique was first applied over six decades ago by Griffiths [8] to confirm the previous predictions of Landau and Lifshitz [7]. In these measurements, a high-frequency (> 1 GHz) magnetic field is applied to the sample, with the absorbed power recorded as a function of the frequency of the microwave magnetic field. Kittel [9] has shown that the resonance conditions depend on the shape of the specimen as well as the crystal orientation. For an infinitely thin plate magnetized in-plane, Kittel's result for the resonance frequency f_0 reads

$$f_0 = \gamma\sqrt{H(H + 4\pi M_0)}, \tag{2.1}$$

where γ is the gyromagnetic ratio, $4\pi M_0$ is the saturation magnetization, and H is the externally applied magnetic field. Therefore, the measurement of the ferromagnetic resonance frequency as a function of the external applied field of the microwave magnetic field allows one to determine the saturation magnetization $4\pi M_0$ of the magnetic sample.

In the presence of losses, the linewidth of the resonance curve allows one to determine the phenomenological Gilbert damping parameter α. We

consider the following form of the LLG equation,

$$\frac{d\vec{M}}{dt} = -\gamma\vec{M} \times \mu_0\vec{H}_{eff} + \frac{\alpha}{M_s}\vec{M} \times \frac{d\vec{M}}{dt}, \tag{2.2}$$

for a thin ferromagnetic film, magnetized in the plan of the film. This case corresponds to the solutions (1.47)–(1.52).

From (1.55), it is evident that the resonance condition is $\omega_0^2 = (1+\alpha^2)\omega^2$, and we find for the diagonal components of χ_{ij},

$$(\chi''_{xx})_{res} = \frac{\omega_M\omega_H}{2\alpha\omega\omega_1} \tag{2.3}$$

$$(\chi''_{yy})_{res} = \frac{\omega_M}{2\alpha\omega\omega_1}\left[\omega_H + 4\pi\omega_M\right]. \tag{2.4}$$

The linewidth $\Delta\omega$ is given by the frequency interval in which χ''_{xx} or χ''_{yy} are equal to half their value at resonance. Therefore,

$$\chi''_{xx} = \frac{1}{2}(\chi''_{xx})_{res}, \tag{2.5}$$

yields

$$\Delta\omega = 2\alpha\omega_1. \tag{2.6}$$

In other words, the dissipation, phenomenologically modeled by the Gilbert damping parameter α, can be extracted from the linewidth of frequency-swept ferromagnetic resonance curves by

$$\alpha = \frac{\Delta\omega}{2\omega_1}. \tag{2.7}$$

2.1.2 Parallel Pumping

It is evident from equation (1.6) that a longitudinal component h_z of the driving field $\vec{h} = (h_x, h_y, h_z)$ does not excite magnetization oscillations. If the driving field is purely longitudinal $\vec{h} = (0, 0, h_z)$, then there is no energy transferred from the driving field to the magnetization. This holds as well (1.46) if the system is damped. Moreover, equations (1.47)–(1.52) imply that a spatially uniform microwave magnetic field excites exclusively uniform magnetization dynamics.

It has been experimentally observed, however, that at large amplitudes of the microwave magnetic field, subsidiary maxima appear in ferromagnetic resonance measurements [117]. These experiments were first performed with transverse $\vec{h} = (h_x, h_y, 0)$ microwave magnetic fields, and theoretical

explanation was provided by Anderson and Suhl [118]. Considering a non-linearized version of equation (1.3), they found that certain spin-wave modes with $|\vec{k}| \neq 0$ could grow exponentially in time, given that the amplitude of the microwave magnetic field was greater than a threshold value h_{th}. This process is a form of parametric resonance and is termed parametric resonance under transverse pumping. A treatment of transverse pumping may be found in [50].

Thereafter, similar phenomena were observed in ferromagnetic resonance measurements with a purely longitudinal driving field [119]. In this case, known as parallel pumping, the driving field acts as a variation of a parameter of the system, the local magnetic field, which results in parametric resonance at amplitudes of the driving field greater than a threshold value h_{th}. In this section, we wish to establish the principle of spin-wave excitation under parallel pumping, following early calculations [120, 121] for ellipsoidal samples.

The starting point is to notice that any energy transfer from a longitudinal driving field to the magnetization must necessarily derive from a non-linearity of (1.3). For simplicity, we consider the following sample geometry and form of the dynamic dipolar field. We consider an ellipsoid magnetized to saturation along its principal axes, with $\vec{H}_0 \parallel \vec{M}_0 \parallel \hat{z}$. Follwing Suhl [120] and Patton [121], we assume the normal modes of the system to be plane waves, so that the magnetization $\vec{m}$ at point $\vec{r}$ and time t can be expanded in a Fourier series,

$$\vec{m}(\vec{r}, t) = \sum_{\vec{k}} \vec{m}_{\vec{k}}(t) e^{i\vec{k}\cdot\vec{r}}. \tag{2.8}$$

This expansion is valid, as long as $|\vec{k}|$ is much greater than the inverse sample dimensions. For $|\vec{k}|$ comparable to the inverse sample dimensions, the magnetostatic eigenmodes, the so-called Walker's modes, must be used.

It can be shown [50], that the spin-wave amplitudes of the mode with wavevector $\vec{k}$, $c_{\vec{k}}$, and with wavevector $-\vec{k}$, $c^*_{-\vec{k}}$, are given by

$$\frac{dc_{\vec{k}}}{dt} = i\omega_{\vec{k}} c_{\vec{k}} + i\gamma h_z \frac{B_{\vec{k}}}{\omega_{\vec{k}}} c^*_{-\vec{k}} \tag{2.9}$$

$$\frac{dc^*_{-\vec{k}}}{dt} = -i\omega_{\vec{k}} c^*_{-\vec{k}} - i\gamma h_z \frac{B^*_{\vec{k}}}{\omega_{\vec{k}}} c_{\vec{k}}. \tag{2.10}$$

Here, $\omega_{\vec{k}} = \sqrt{A_{\vec{k}}^2 - B_{\vec{k}}^2}$ is the frequency of the spin-wave of wavevector $\vec{k}$, and

$$A_{\vec{k}} = \omega_H + q\gamma M_0 k^2 + \frac{1}{2}\omega_M \sin^2\theta_k \tag{2.11}$$

$$B_{\vec{k}} = \frac{1}{2}\omega_M \sin^2\theta_k e^{i2\phi_k}. \tag{2.12}$$

It is evident from (2.9) and (2.10) that $B_{\vec{k}} \neq 0$ and $h_z \neq 0$ leads to coupling of the spin-wave modes at $\vec{k}$ and $-\vec{k}$. It can be shown [120, 121], that the coupling of the spin waves at $\vec{k}$ and $-\vec{k}$ leads to the exponential growth of the amplitudes, i.e. the parametric spin-wave instability, at $\omega_{\vec{k}} = \frac{\omega_p}{2}$. In the presence of damping, the parametric spin-wave instability occurs only for values of the pumping field greater than a threshold value, given by

$$h_{th} = \min\left[\frac{\omega_{r\vec{k}}}{|V_{\vec{k}}|}\right] \tag{2.13}$$

where $\omega_{r\vec{k}}$ is the relaxation frequency of the mode at $\vec{k}$ and $V_{\vec{k}} = \frac{\gamma B_{\vec{k}}}{2\omega_{\vec{k}}}$ is the coupling parameter between the spin-wave amplitudes $c_{\vec{k}}$ and $c^*_{-\vec{k}}$.

We therefore may state the qualitative characteristics of the parallel pumping process relevant to our experimental results. On the one hand, the pumping process must exceed a threshold to induce exponential growth of the dynamic magnetization. On the other hand, this threshold amplitude of the pumping field is proportional to the mode damping and ellipticity.

2.2 BLS

In this section, we discuss the technique used for the detection of current-induced magnetization dynamics in the experiments of chapters 5–7. The well-established technique of Brillouin light scattering (BLS) [48] has been developed in recent years to enable the study of spin waves in microscopic structures. Micro-focus Brillouin light scattering (μBLS) [122, 123] applies the principle of BLS to the study of magnetization dynamics at nanometer length scales, at the expense of wavevector resolution. The unprecedented sensitivity of μBLS enables the frequency-resolved study of magnetization oscillations in real space, with a diffraction-limited spatial resolution and frequency resolution of up to 50 MHz, limited by the stability requirements of the interferometer. Moreover, μBLS enables the study of thermal magnetization fluctuations—magnetization oscillations in the absence of external excitation.

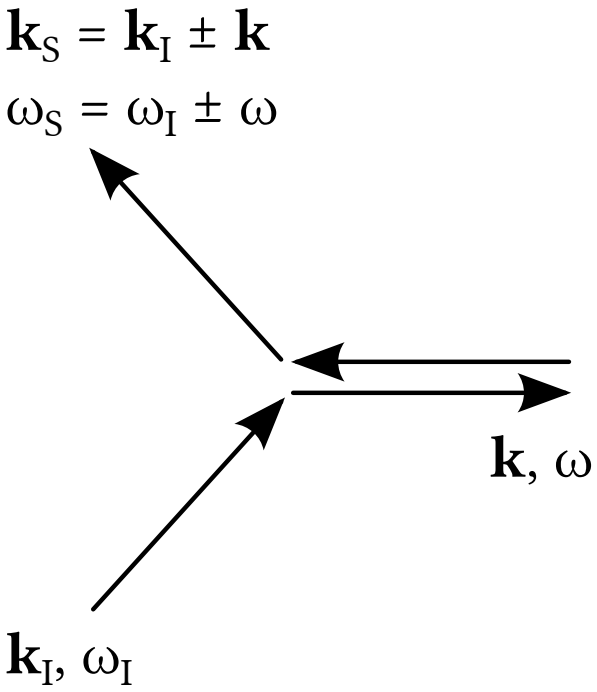

Figure 2.1: A schematic of the BLS scattering process.

2.2.1 Scattering

The scattering process, schematically shown in Figure 2.1, is identical in BLS and μBLS [124]. Incident photons interact with the excitations of the magnetic system, magnons, and may exchange energy during magnon creation/annihilation processes. Under conditions of energy and momentum conservation, an incident photon of frequency ω_I and wavevector $\vec{k}_I$ may annihilate or create a magnon of frequency and wavevector ω_m and $\vec{k}_m$ resulting in a scattered photon of frequency $\omega_I \pm \omega_m$ and wavevector $\vec{k}_I \pm \vec{k}_m$ whereby

$$\hbar\omega_S = \hbar\omega_I \pm \hbar\omega_m \tag{2.14}$$

$$\vec{k}_S = \vec{k}_I \pm \vec{k}_m \tag{2.15}$$

and ω_S is the frequency of the scattered photon, $\vec{k}_S$ its wavevector. In the case of magnon annihilation, one speaks of an anti-Stokes process; in the case of magnon creation, one speaks of a Stokes process.

By choice of the scattering geometry, it is possible to select the wavevector of the incident and detected photon and thus the magnon participating in the scattering process. Three scattering geometries are applied in BLS

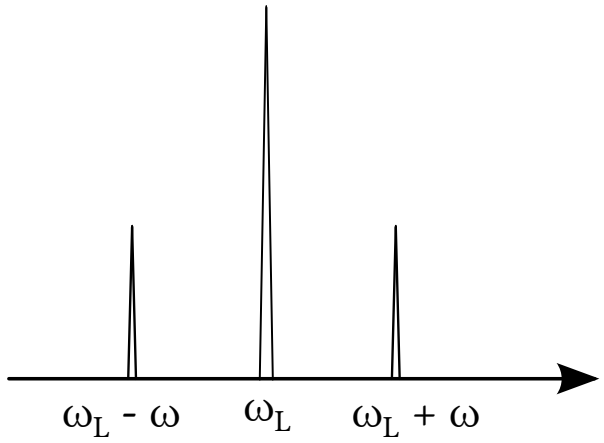

Figure 2.2: A schematic of the spectral peaks due to inelastic scattering of photons on magnons.

experiments, with the choice depending on the qualities of the sample under investigation,

- Back scattering: the scattered light (inelastic and elastic) is collected by the same objective lens used to focus the light onto the sample. Back scattering corresponds to a scattering angle $\psi \approx 180°$.
- Forward scattering: the scattered light (inelastic and elastic) is transmitted through the sample and collected by a second lens of large aperture. Forward scattering corresponds to a scattering angle $\psi \approx 0°$.
- Right-angle scattering: the scattered light (inelastic and elastic) is reflected from the sample and collected by a lens situated at a right angle with the incident light. Right-angle scattering corresponds to a scattering angle $\psi = 90°$.

In each case, the scattering geometry is chosen either to reduce the contribution of elastically scattered light, which appears as background and limits the contrast of the interferometer, and thus the sensitivity of the measurement, or in order to achieve wavevector sensitivity: back scattering enables the study of large $|\vec{k}_m|$ excitations, forward scattering is often chosen if the excitations of interest have small $|\vec{k}_m|$. In our measurements, we study non-transparent samples and therefore use exclusively the back scattering geometry.

In scattering experiments, one detects the scattered light at a selected wavevector, frequency, and polarization. In order to measure the spectrum

of the scattered light, we measure the differential scattering cross section, $\frac{d^2\sigma}{d\Omega d\omega_S}$, defined as the number of photons scattered into a solid angle $d\Omega$ between ω_S and $\omega_S + d\omega_S$ per unit incident flux density, where ω_S is the frequency of the scattered photon.

The classical description of Brillouin light scattering of photons on magnons consists in the consideration of magnon-induced fluctuations in the dielectric permittivity of the medium [125]. A magnon, or spin wave, constitutes a spatial variation of the magnetization of the system, which creates a phase grating in the medium. Due to Bragg diffraction and the Doppler effect, the light scattered from the grating changes its wavevector, determined by the spin-wave wavevector, and frequency, determined by the spin-wave phase velocity [47].

The magnon-induced fluctuations in the dielectric permittivity $\delta\epsilon^{\alpha\beta}$ may be represented as [51]

$$\delta\epsilon^{\alpha\beta} = \mathsf{F}^{\alpha\beta\gamma} M_\gamma + \mathsf{G}^{\alpha\beta\gamma\delta} M_\gamma M_\delta, \tag{2.16}$$

where the indices $(\alpha, \beta, \gamma, \delta)$ run through the coordinate directions, summation over repeated indices is implied, and M_i is the component of the dynamic magnetization in the i-th direction. The tensors F and G describe circular birefringence and linear dichroism or linear birefringence and circular dichroism, respectively. With these definitions, it can be shown that the differential scattering cross section is given by [48, 51],

$$\frac{d^2\sigma}{d\Omega d\omega_S} \propto \langle \delta\epsilon^*(\vec{k}_I - \vec{k}_S)\delta\epsilon(\vec{k}_I - \vec{k}_S)\rangle_{\omega_I - \omega_S} \tag{2.17}$$

where $\langle \cdots \rangle$ denotes statistical averaging. In view of (2.16), it follows that for the Fourier component of the correlation function $\langle \delta\epsilon^*(\vec{k})\delta\epsilon(\vec{k})\rangle_\omega$ of the fluctuating dielectric permittivity

$$\langle \delta\epsilon^*(\vec{k})\delta\epsilon(\vec{k})\rangle_\omega = \int d(t_2 - t_1) d^3(\vec{r}_2 - \vec{r}_1) e^{-i(\omega(t_2 - t_1) + \vec{k}\cdot(\vec{r}_2 - \vec{r}_1))} \langle \delta\epsilon^*(\vec{r}_1, t_1)\delta\epsilon(\vec{r}_2, t_2)\rangle \tag{2.18}$$

$$\propto \int d(t_2 - t_1) d^3(\vec{r}_2 - \vec{r}_1) e^{-i(\omega(t_2 - t_1) + \vec{k}\cdot(\vec{r}_2 - \vec{r}_1))} \langle \vec{m}^*(\vec{r}_1, t_1)\vec{m}(\vec{r}_2, t_2)\rangle, \tag{2.19}$$

and, therefore, the measured intensity of the scattered light at frequency ω is proportional to the magnitude of the magnetization fluctuations.

Lastly, we note that the wavevector conservation law (2.14) follows from the integration over all space in (2.19), whereby the correlation function is

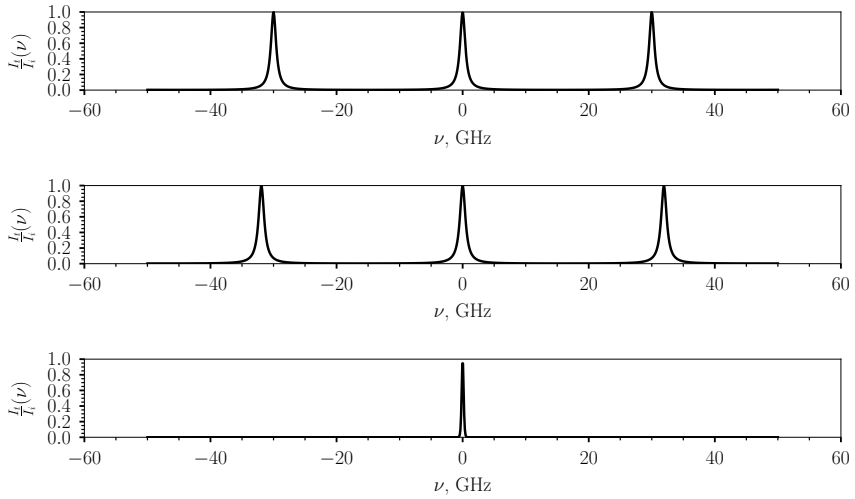

Figure 2.3: Top: Transmission of a single three pass etalon with $d = 5$ mm, $\mathcal{F} = 30$. Middle: Transmission function of three pass etalon oriented at an angle 20° with respect to the first. Bottom: Composite transmission function of etalons from (a) and (b) operating in tandem.

nonzero only if $\vec{k} = \vec{k}_S - \vec{k}_I$. If the translational invariance of the problem is broken, for example by a confined scattering volume, the wavevector is not well-defined in the directions of confinement, with uncertainty inversely proportional to the size of the confinement. We return to this consideration in our discussion of μBLS.

The *sine qua non* of a modern BLS apparatus is the multi-pass tandem Fabry-Pérot interferometer [126]. It is the interferometer that enables study of spin waves with a frequency resolution down to 50 MHz, and a contrast $> 10^{10}$. Typical magnon frequencies 1–100 GHz under investigation in BLS measurements are orders of magnitude smaller than the frequency ≈ 550 THz of the probing light. Thus, it is necessary to apply a high resolution frequency analyzing technique to the scattered light, in order to ascertain the magnon frequency.

A single Fabry-Pérot etalon [127] consists of two parallel, flat mirrors separated by a distance d of medium with refractive index n. We consider light incident normal to the plates. Then, the ratio of the intensity of transmitted light I_t to the intensity of incident light I_i at frequency ν is given by [127]

$$\frac{I_t}{I_i} = \frac{\tau}{1 + \frac{4\mathcal{F}^2}{\pi^2} \sin^2\left(\frac{2\pi dn}{c}\nu\right)} \tag{2.20}$$

where τ is the peak transmission, $\mathcal{F}$ the finesse, and c the speed of light in vacuum. The quantity $\frac{I_t}{I_i}$ is also called the transmission function of the etalon. The peak transmission $\tau \leq 1$ is maximum if $\mathcal{T}+\mathcal{R}=1$, where $\mathcal{T}$ and $\mathcal{R}$ are the transmissivity and reflectivity of the mirrors, and thus is limited by absorption. The sensitivity is limited by the contrast factor $\mathcal{C}$,

$$\mathcal{C} = \frac{\left(\frac{I_t}{I_i}\right)_{max}}{\left(\frac{I_t}{I_i}\right)_{min}}, \tag{2.21}$$

which is determined by the finesse $\mathcal{F}$,

$$\mathcal{C} = 1 + \frac{4\mathcal{F}^2}{\pi^2}. \tag{2.22}$$

Ideally, the finesse is determined solely by the reflectivity $\mathcal{R}$ of the mirrors,

$$\mathcal{F} = \frac{\pi\sqrt{\mathcal{R}}}{1-\mathcal{R}}, \tag{2.23}$$

however, factors such as non-planity of the mirrors serve to decrease the finesse. The finesse determines the width $\delta\nu$ of the transmission peaks,

$$\delta\nu = \frac{\Delta\nu}{\mathcal{F}} \tag{2.24}$$

where the free spectral range $\Delta\nu$ gives the frequency spacing between two transmission peaks (2.20),

$$\Delta\nu = \frac{c}{2nd}. \tag{2.25}$$

For typical etalon parameters, a single interferometer arrangement does not exhibit a sufficiently high contrast ratio to distinguish between the lines of the inelastically scattered light and the peak of the elastically scattered light. The design of a tandem (two-etalon) multi-pass (folded beam) Fabry-Pérot interferometer by Sandercock first enabled the study of magnons by the BLS process [128]. We discuss the so-called (3+3)-pass arrangement of two etalons operating in tandem, with the beam passing 3 times through each etalon. The finesse of a 3-pass etalon $\mathcal{F}_3$ is given by

$$\mathcal{F}_3 = \frac{\mathcal{F}}{\sqrt{2^{\frac{1}{3}}-1}} \tag{2.26}$$

which significantly improves the contrast factor of the etalon. In Sandercock's arrangement, the etalons are oriented at an angle θ to one another, and one

mirror of each etalon is mounted on a linear scanning stage. We refer to the etalon receiving light from the sample as FP1 and the second etalon as FP2. In the tandem arrangement,

$$d_{FP2} = d_{FP1} \cos\theta, \tag{2.27}$$

therefore, in general, the etalon transmission functions $\left(\frac{I_t}{I_i}\right)_{FP2}(\nu) \neq \left(\frac{I_t}{I_i}\right)_{FP1}(\nu)$. The transmission function of a single etalon is periodic, with period $\frac{d}{2}$, which can hinder the analysis of the inelastic scattering peaks, due to erroneous assignment to the appropriate transmission order. In the tandem arrangement, it is found, that the overlap of two transmission orders, depending on the mirror distance d_{FP1} leads to unambiguous assignment of the inelastic scattering peaks, since neighbouring peaks do not add constructively. Therefore, under conditions of stability, the multipass, tandem Fabry-Pérot interferometer achieves the necessary contrast and free spectral range to analyze the spectral peaks of the scattered light due to inelastic scattering of photons on magnons.

2.2.2 μBLS

The foregoing discussion applies to a standard BLS arrangement. The development of μBLS applies the BLS principle to achieve the spatial resolution necessary to study magnetization oscillations on a scale limited by diffraction. A schematic of the μBLS extension is shown in Figure 2.4. In the back scattering geometry, the incident light from a diode-pumped solid state laser (Spectra-Physics Excelsior 532) is focused on the sample by an objective lens characterized by a large magnification (100x) and numerical aperture (0.75). In order to ensure minimum beam diameter at the sample surface, the laser light, corresponding to a single TEM_{00} spatial mode, is expanded by a beam expander and passed through a small round diaphragm, to reduce beam divergence. The resulting spot size at the sample is, in a far-field scheme, determined by the wavelength, in our experiments 532 nm, resulting in a spot size of $\approx$ 250nm. The sample is positioned by a piezoelectric stage, with a precision of 50 nm along each of the three dimensions.

The small spatial length scales of interest in μBLS measurements require careful mechanical stabilization of the sample/stage system. An optical table is used to damp ambient vibrations, while an active stabilization system corrects spontaneous drift and ensures a constant positioning of the laser spot over long measurement times. White light from a standard flashlight is focused onto the sample along with the laser beam. The reflected white light is filtered to attenuate the intensity of the laser beam and collected

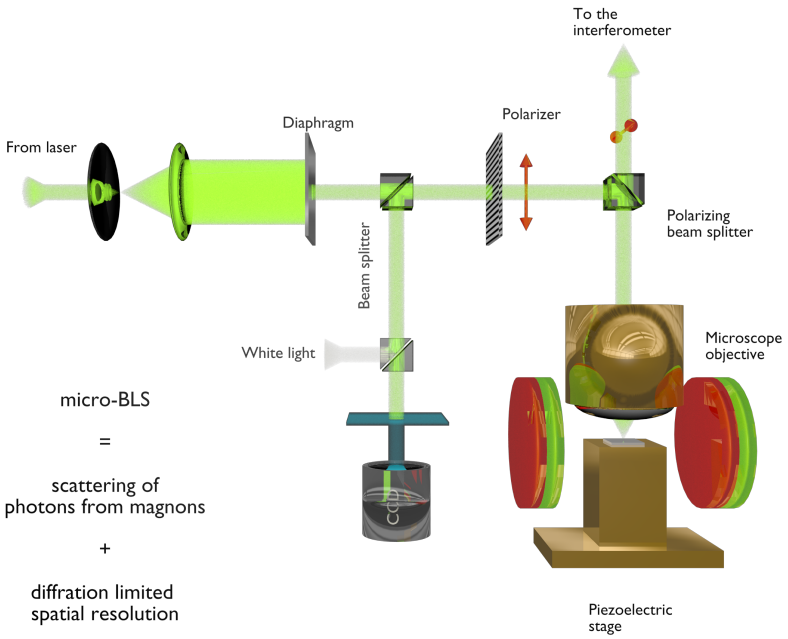

Figure 2.4: A schematic of the μBLS setup, courtesy H. Ulrichs.

by a CCD camera fitted with a telescopic objective. The obtained image enables precise positioning of the laser spot on the sample, and in case of need, active stabilization by image analysis linked with the positioning stage. It is important to note that the intensity of the incident light is < 1 mW, in order to ensure the absence of sample heating under the laser spot.

The light is collected by the same objective and sent to the Fabry-Pérot for spectral analysis. A coarse reduction of the intensity of the elastic component of the scattered light is achieved by the polarizer and polarizing beam splitter shown in Figure 2.4. The inelastically scattered light interacts with the magnetic system of the sample, and, due to magneto-optical effects, undergoes a 90° rotation of its polarization plane. By applying a polarizer with an extinction ratio of $1 : 10^4$ in combination with a polarizing beam filter to transmit the rotated light, assists in eliminating the background of the elastically scattered light in the BLS spectral analysis.

The analysis of the scattered light follows the same principles as in a standard BLS arrangement, with one notable exception. As previously mentioned, the confinement of the scattering volume, in μBLS caused by the small lateral spot size and the microscopic transverse dimensions of the thin film samples, forfeits the wavevector resolution available in BLS ex-

periments. While BLS works in the frequency domain, with spatial resolution in reciprocal space, the confinement of the scattering volume in μBLS results in information in the frequency domain, with spatial resolution in real space. Depending on the numerical aperture of the objective, scattered light is collected up to a maximum scattering angle θ_{max}, resulting in the scattered light simultaneously containing spectral contributions from all magnons with wavevector $|\vec{k}_m| < |\vec{k}_{max}|$, in our experimental configuration, $|\vec{k}_{max}| \approx 1.5 - 2.5 \times 10^5 \mathrm{cm}^{-1}$. Therefore, the intensity of the scattered light at frequency ω is proportional to the spectral density of magnons at ω.

2.3 SKEM

A complimentary technique to μBLS, developed in our workgroup in the context of this work, is ferromagnetic resonance scanning Farady/magneto-optical Kerr effect microscopy (SFEM or SKEM) [44, 129]. This technique is an extension of time-resolved scanning Faraday/Kerr effect microscopy, in which data is collected in the time domain, with spatial resolution in real space. In SKEM, data is collected directly in the frequency domain, with spatial resolution in real space. The spatial resolution is, like μBLS, limited by the spot size of the focused laser beam at the sample. In this section, we introduce the SKEM setup. We discuss the origin of the SKEM signal, the magneto-optical Kerr or Faraday effect, depending on whether one works in the reflection or transmission geometry, respectively. We then present the details of the measurement setup.

2.3.1 MOKE/Faraday Effect

In SFEM/SKEM experiments, light is focused onto the sample, and the signal is obtained by analyzing the rotation of the plane of polarization, and possibly the ellipticity of the reflected light. The Faraday effect, i.e. magnetic circular birefringence, denotes the rotation of the plane of polarization of linearly polarized light under transmission through a magnetized sample [130]. In a magnetized medium, the refractive index of circularly polarized light are different for right and left-handed polarization. Therefore, linearly polarized light is decomposed upon propagation through the medium, and upon recombination, experiences a rotation of the plane of polarization proportional to the difference in the refractive indices of left- and right-hand polarized components, and the sample thickness.

In contrast, the magneto-optical Kerr effect is associated with a change in the polarization state of light upon reflection from magnetic media. De-

pending on the orientation of the plane of incidence, the incoming light polarization, and the sample magnetization, one speaks of three MOKE reflection geometries–longitudinal, transverse, and polar. In our experiments, we work exclusively in the polar MOKE geometry—in which the magnetization is oriented parallel to the film normal vector and parallel to the plane of incidence—and therefore address its specifics here. The consideration of the MOKE signal reduces to the solution of macroscopic Maxwell's equations with respect to the boundary conditions between the sample and vacuum, in which one accounts for magneto-optical effects by relating the Fresnel coefficients to the sample magnetization via the dielectric tensor. In the polar Kerr effect geometry, we specifically assume incidence normal to the sample surface. Under the condition of small rotations, valid for a wide range of experimental conditions, the complex Kerr angle Φ_K,

$$\Phi_K = \Theta_K + i\Psi_K \tag{2.28}$$

where Θ_K is the Kerr rotation and Ψ_K the Kerr ellipticity, can be given as [130],

$$\Phi_K = \frac{\sqrt{\epsilon_0 \epsilon_{xx}}}{\epsilon_0 - \epsilon_{xx}} \frac{\epsilon_{xy}}{\epsilon_{xx}} \tag{2.29}$$

where ϵ_{ij} are the component of the dielectric tensor, $\vec{D} = \overleftrightarrow{\epsilon}\ \vec{E}$. The MOKE rotation occurs, since ϵ_{xy} is linearly proportional to the magnetization. The theory of MOKE in multilayer systems has been worked out [131] in the framework of a matrix formalism.

2.3.2 SKEM

A schematic of the experimental setup is shown in Figure 2.5. We describe the setup in operation in the reflection geometry. The optical system consists of a second-harmonic generator, a beam expander and diaphragm, a beamsplitter, an objective lens, the sample, a Wollaston prism, and two balanced photodiodes. The principle of excitation/detection is based on stroboscopic imaging.

A Ti-sapphire modelocked laser, a Mira 900 from Coherent Inc., has been operated at a wavelength of 800 nm, a pulse-duration of about 200 fs, pulse energy 0.013 nJ and a average power of less than 1 mW. The pulses are frequency doubled and, in order to reduce beam divergence, a beam expander-diaphragm spatial filter is inserted in the beam path. The light is focused onto the sample by an objective with large magnification (100x) and numerical aperture (NA = 0.90), in order to achieve minimum spot size $\approx$ 200

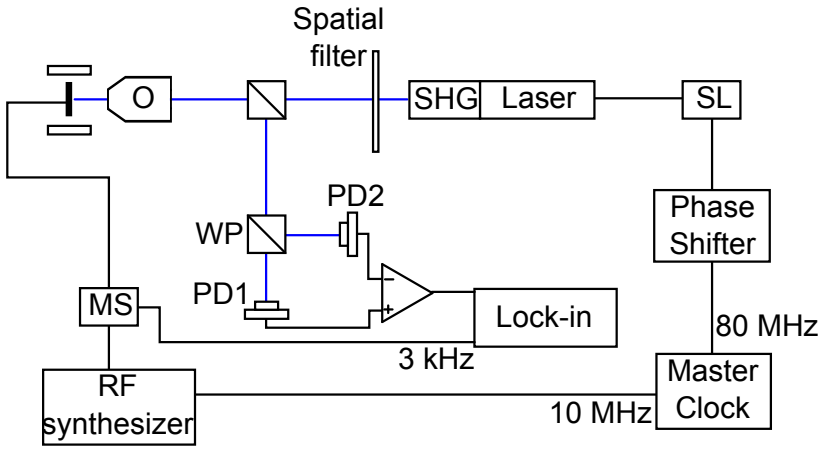

Figure 2.5: A schematic of the SKEM setup. O-Objective, MS-Microwave switch, WP-Wollaston prism, SHG-second harmonic generator, SL-Coherent Inc. Synchrolock module, PD1/2-photodiode 1/2.

nm. The reflected light is collected by the same objective, then split by a Wollaston prism onto two balanced photodiodes.

A sinusoidal microwave field of frequency f_{ex} sent through the microstrip antenna generates the excitation field h_{ex}. An oven-controlled crystal oscillator generates a highly-stabilized 10 MHz reference signal, which acts as a reference to generate the sinusoidal microwave field, as well as an 80 MHz signal used to phaselock the pulses to the CW microwave signal. To achieve phaselocking, the microwave frequency must be a multiple of both the laser repetition rate and the reference frequency, i.e. an integer multiple of 80 MHz. To improve the signal-to-noise ratio, we apply the microwave pulses for 150 μs at a repetition frequency of 3 kHz and a lock-in amplifier extracts this frequency component from the photoinduced current. We note that, due to the lock-in technique, we measure the contrast of the out-of-plane component between the excited state and its value in the absence of the excitation field.

As shown in Figure 2.6, by adjusting the phase between the 10 MHz reference signal, and the 80 MHz signal locked to the laser pulses, we are able to measure the response of the dynamic magnetization over a full cycle of the excitation field. We are thus able to measure both the amplitude and phase of the dynamic magnetization at the frequency of the excitation field.

Positioning and control are accomplished by a mechanical scanning stage with a precision of 50 nm along the three axes. By scanning the laser spot

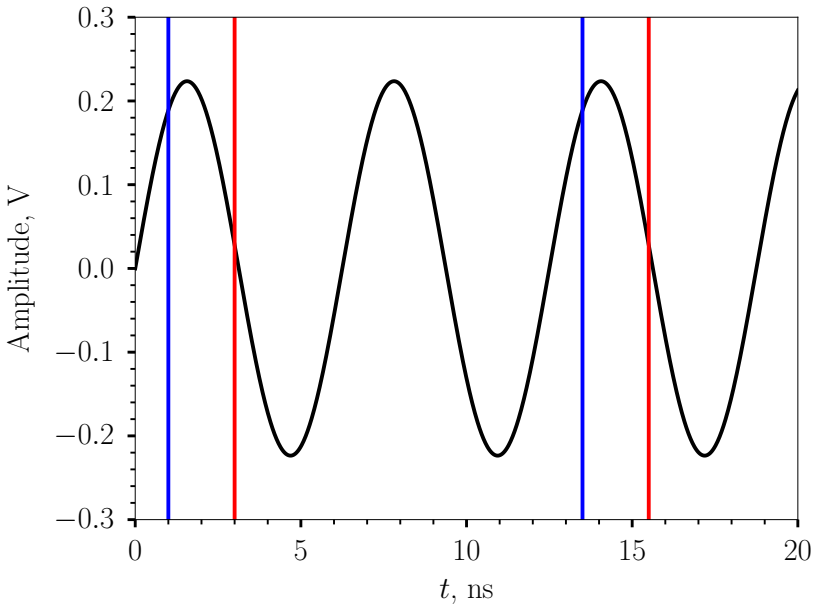

Figure 2.6: Representation of the timing for an hf excitation field of 160 MHz, average power 1 mW. The blue and red vertical lines correspond to probe pulses with delays of 1 and 3 ns, respectively.

over the sample surface, we obtain spatially resolved images of the dynamic magnetization in the frequency domain.

2.3.3 Noise analysis

Finally, we address the sensitivity of the setup, by analyzing the minimum detectable Kerr angle θ_k [129]. The detector comprises a Wollaston prism, two balanced photodiodes, and a differential amplifier.

The excitation current is modulated at a frequency f_{ln}, and a lock-in amplifier extracts this frequency component from the difference output of the differential amplifier connected to the two photodiodes. The lock-in signal V_{ln} is related to the Kerr rotation [129] by

$$\theta_k = \frac{\pi V_{ln}}{2\sqrt{2}(i_1 + i_2)G} \tag{2.30}$$

where G is the gain of the lock-in amplifier and i_1 and i_2 are the intensities at the two photodiodes. An irreducible noise element occurs in this measurement setup from shot noise in the photoinduced currents. It can be

shown [129], that the shot noise places a lower bound θ_{kmin} on the measurable Kerr rotation,

$$\theta_{kmin} = \frac{\pi}{2}\sqrt{\frac{eB}{2(i_1 + i_2)}} \tag{2.31}$$

where e is the electron charge and B is the bandwidth. The minimum measurable Kerr rotation is, therefore, inversely proportional to the intensity of the laser beam at the sample. Caution must be taken, however, as heating effects distort the magnetic signal, and therefore limit the sensitivity of the apparatus.

Chapter 3

Magnetostatic spin-wave modes of an in-plane magnetized garnet-film disk

3.1 Introduction

This chapter addresses the spin-wave eigenmode spectrum of an in-plane magnetized 1.3 mm diameter yttrium iron garnet (YIG) disk. In this sample, the spin-wave dynamics are governed by the dipolar interaction, so the modes are termed magnetostatic. We use SFEM, described in detail in Chapter 2, to locally record the magnetization response to a dynamic magnetic field oriented out-of-plane. We find that the classification, previously applied to in-plane magnetized rectangular samples, of eigenmodes as a product of one-dimensional, orthogonal standing waves is not valid in the case of an in-plane magnetized disk. Instead, imaging the modes up to very high order, we obtain a complex spatial profile of the modes, which depends on the position of the mode frequency relative to the quasi-uniform mode of the disk. Moreover, we observe the appearance of an interference pattern, generated by defect scattering and angular confinement of energy flow, due to the anisotropic dispersion.

3.2 Experiment

3.2.1 Sample

The investigated samples were prepared from a 5.1 μm thick high-quality monocrystalline film of YIG grown on transparent gadolinium gallium gar-

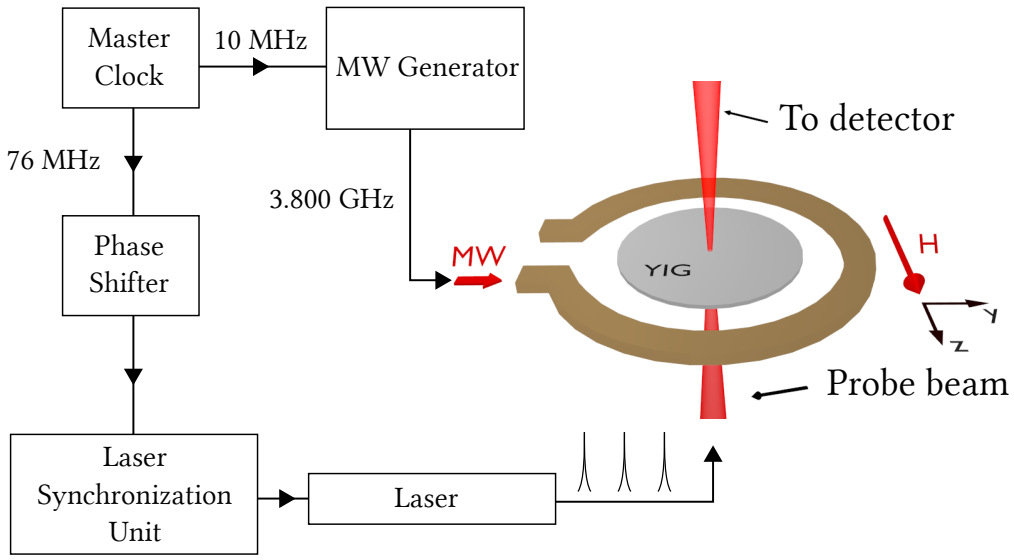

Figure 3.1: Schematic of the experimental setup.

net substrate. The sample was chemically etched to produce a disk with a diameter of 1.3 mm. It was mounted on a computer controlled scanning stage and placed in the center of an electromagnet, capable of providing the static in-plane magnetic field $B = 0 - 300$ mT, saturating the magnetization of the sample and tuning the eigenfrequencies of the spin-wave modes. In order to excite spin-waves, the sample was placed in the center of a circular loop copper microwave antenna, with an inner diameter of 2 mm. The excitation geometry is represented schematically in Figure 3.1. Applying a microwave continuous-wave (CW) current to the loop, the antenna produces a microwave magnetic field b directed along the sample normal. Thus, the condition for linear excitation of the magnetization $b \perp M$ is fulfilled. Throughout this experiment we have used a microwave frequency of 3.800 GHz, and the microwave power was varied from 10^{-5} mW to 1.6×10^{3} mW.

The magnetization dynamics was detected by stroboscopic imaging via magneto-optical Faraday-effect magnetometry synchronized with the microwave field, described in detail in Chapter 2. By scanning the laser spot over the sample edge and analyzing the intensity profile of the transmitted light, an optical resolution of 30 μm, close to the theoretical resolution limit of 20 μm of the optical system with a numerical aperture of NA = 0.025, has been determined. The angle of the Faraday rotation is proportional to the magnetization component parallel to the beam direction of propagation. For the

used experimental geometry this means that the setup is sensitive to the out-of-plane component of the magnetization, $M_\perp$. The experimental data shown below represent the dynamic out-of-plane magnetization normalized by M_s. In the rest of the paper we will refer to the ratio $m_\perp = \frac{M_\perp}{M_s}$ as the out-of-plane precession angle.

3.2.2 Micromagnetics

Micromagnetic simulations of the eigenmode spectrum have been carried out using the freely available OOMMF micromagnetics code [132]. The program approximates the magnetization to be uniform inside the cells of a rectangular mesh. In order to minimize the artifacts due to this discretization and, on the other hand, achieve a reasonable computation time, the dimensions of the cells have to be optimized. As the experimental setup is mainly sensitive to the modes with quasi-uniform profile of the amplitude across the film thickness, we have chosen a perpendicular discretization stepsize equal to the film thickness. Together with an in-plane discretization of 10 μm, which is smaller than the optical resolution of the setup, this results in reasonable computation times of about 1 day using a standard PC.

We have assumed the literature values for the saturation magnetization, $\mu_0 M_s = 0.175$ T, the exchange constant, $A = 3.614 \times 10^{-12}$ J/m, the gyromagnetic ratio $\gamma = 2.21 \times 10^5$ m/(As), and the Gilbert damping parameter, $\alpha = 5 \times 10^{-5}$ [28,133]. The ferromagnetic resonance (FMR) linewidth of the film (at 8 GHz) is $2\Delta B \approx 5\times 10^{-2}$ mT (in agreement with the cited value of α), the saturation magnetization $\mu_0 M_s = 0.175$ T. The external field has been set to $B_{ext} = 70$ mT, found experimentally to match the main mode at the experimental excitation frequency of $\nu = 3.800$ GHz. The magnetization, relaxed previously to the ground state, has been excited with a weak, short, Hann-shaped DC-field pulse directed along the film-normal. In order to guarantee that only a linear response is produced, a low maximum strength of the exciting field of 10 μT has been applied. This results in a maximum out-of-plane precession angle of about 0.3×10^{-3} rad, a value which is one order of magnitude below the experimentally found nonlinearity threshold. The selected duration of the fieldpulse of 270 ps has a Fourier spectrum which is flat in the frequency range of the eigenmodes, between 3-4 GHz, therefore all exited modes correspond to a sinusoidal CW excitation of the same power and phase. In order to optimally resolve the dense spectrum of eigenmodes a long total simulation time of 800 ns yielding a frequency resolution of 0.125 MHz has been selected. The calculated maps of the magnetization have been stored at a sampling frequency of 20 GHz and converted with a discrete Fourier transformation into the frequency domain. In the experimental

field range, the frequency is a linear function of the field, and the spectra are subsequently converted into the field domain for direct comparison with experiment.

3.2.3 Results

In an unconfined medium a uniform microwave field can only linearly excite ferromagnetic resonance (the fundamental spin-wave mode with zero wavevector). All other spin-wave modes described by nonzero wavevectors and correspondingly varying frequencies cannot be excited under such conditions. In laterally confined films the situation is changed: (i) the spectrum of spin waves becomes quantized due to the finite size effect, which imposes selection rules on the in-plane wavevector; (ii) a spatially uniform microwave field of a given frequency can excite different spin-wave modes, albeit at different applied magnetic fields and with different effectiveness. Figure 3.2 illustrating the spin-wave spectrum in the studied YIG disc shows the measured out-of-plane precession angle as a function of the applied magnetic field. The upper curve represents the out-of-plane precession angle recorded at the sample center. One sees several peaks corresponding to different spin-wave modes. The most profound peak apparently corresponds to a fundamental spin-wave mode for this confined structure. Weaker peaks both at higher and lower applied fields indicate excitation of non-uniform modes. By recording this curve the phase of the microwave field has been adjusted to maximize the detected signal for the fundamental mode. Note that the phases of the spin-wave modes change alternatively with increasing or decreasing magnetic field. This is connected with excitation conditions of the corresponding modes by the spatially quasi-uniform microwave field.

Measurements at the center of the disc provide valuable information on the spin-wave modes. However, they also have essential drawbacks: (i) there is no information on the mode-profiles; (ii) the signal-to-noise ratio is rather poor. These disadvantages can be removed, if one maps the out-of-plane precession angle over the entire sample at a given applied field. First, the mode structure can be obtained in this way, as discussed below. Second, by integrating the squared out-of-plane precession angle over the sample one increases the signal-to-noise ratio as demonstrated by the lower curve in Figure 3.2, showing $\langle m_\perp \rangle = \sqrt{\int\int m_\perp^2(y,z)dydz}$. Up to 15 resonances are observed using this approach. Comparison of the resonance fields for different modes given by the upper and the lower curves in Figure 3.2 indicates a very good agreement between the two techniques.

Figure 3.2 demonstrates the results of the modeling of the spin-wave dy-

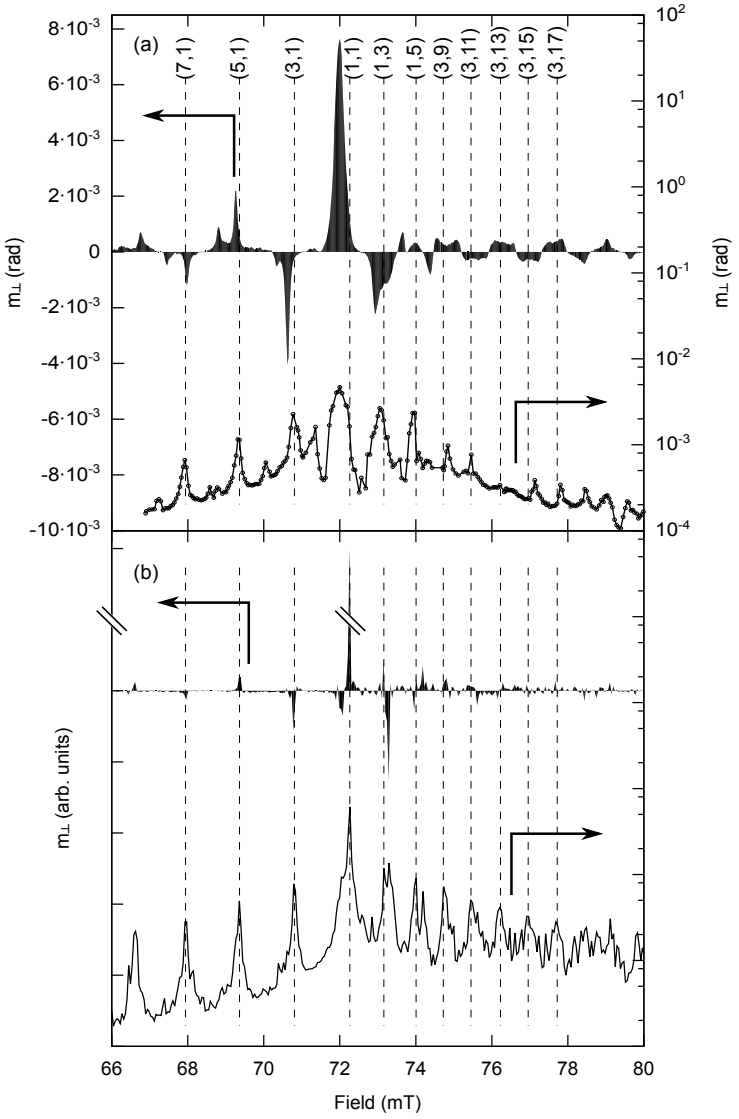

Figure 3.2: (a) Field-swept spectrum recorded in experiment for microwave frequency 3.800 GHz. Filled curves represent data recorded with the laser spot fixed at the sample center. Points correspond to data obtained by integration over the sample. (b) The corresponding curves obtained using the OOMMF simulations.

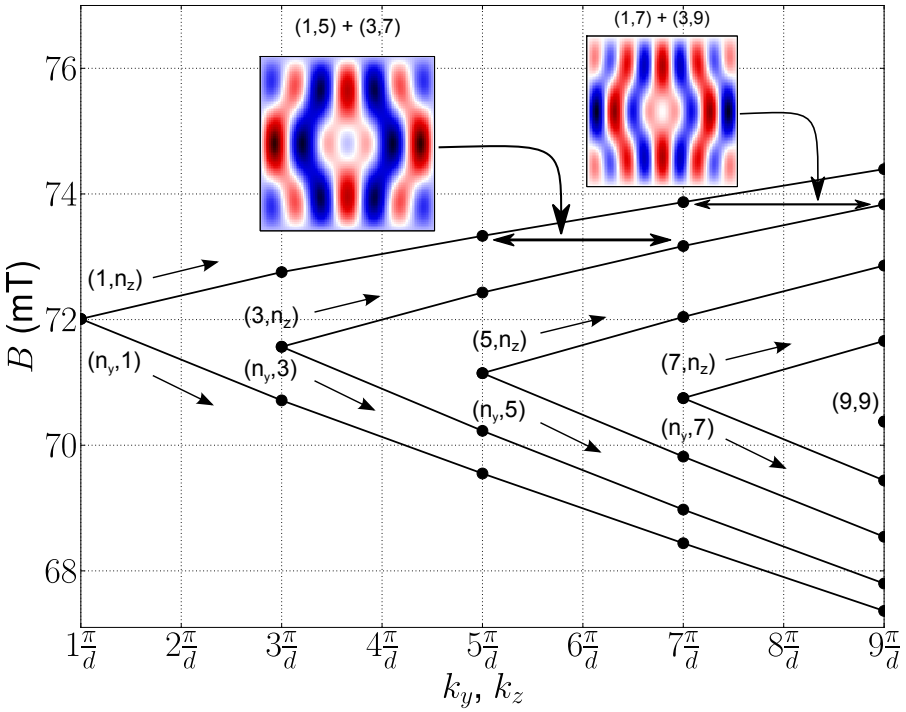

Figure 3.3: Frequencies of the spin-wave modes in a square sample with different number of antinodes. Note partial degeneracy of different modes. Inset: calculated spatial profiles of the pattern formed by a linear combination of the (1,5)- and (3,7)-modes and (1,7) and (3,9) modes.

namics in a YIG disk using the approach described above. One can see that modeling nicely reproduces the experimental data for the resonance fields for most of the modes, as illustrated by the vertical dash lines in Figure 3.2 corresponding to the theoretically determined resonance fields. Moreover, by analyzing the calculated mode profiles (see below) one can classify the modes by two integers (shown in brackets) indicating the number of antinodes on a line through the center of the sample perpendicular and parallel to the field, respectively. Apparently, the modeling shows only the spin-wave modes with odd antinode numbers. This fact is connected with the quasi-uniform spatial profile of the excitation field. In fact, the excitation efficiency of a mode with a given spatial profile of the out-of-plane magnetization $m_\perp(y,z)$ is proportional [21] to the overlap integral of $m_\perp(y,z)$ with the excitation microwave magnetic field produced by the loop $h(y,z)$, $\int\int h(y,z)m_\perp(y,z)dydz$. Since the field is quasi-uniform over the sample, only modes with an odd number of antinodes in either direction are efficiently excited. It is important to note that the effectiveness of the excitation decreases with increasing number of antinodes in the mode. Therefore, to analyze the general features of the modes with different symmetries, we have chosen modes with one antinode in one direction, since these modes should have higher excitation effectiveness. In general, modes with an even number of antinodes in either direction are not excluded by lateral confinement but require excitation by a spatially non-uniform microwave field [134]. One can also observe in Figure 3.2 some additional modes, which apparently correspond to even numbers of the antinodes perpendicular to the magnetic field. The excitation of these modes is due to a non-uniform profile of the microwave field along this direction, caused by the inevitable disturbance of the axial symmetry by the leads of the excitation loop shown in in Figure 3.1.

Analytical modeling of the spin-wave dynamics of an in-plane magnetized disc is extremely challenging task, since the axial symmetry of the sample is broken by the field. Nevertheless, to gain insight into general properties of the observed modes, it is constructive to compare them with the modes of an otherwise identical YIG square sample with side length equal the diameter of disk, d. In a square sample the two-dimensional profile of each mode can be factorized

$$m_\perp(y,z) = A\cos k_y y \cos k_z z = A\cos\frac{n_y\pi}{d}y\cos\frac{n_z\pi}{d}z \qquad (3.1)$$

where n_y and n_z are the numbers of antinodes along the corresponding direction. The frequency of a spin wave with a wavevector defined by its in-plane components $k = (k_y, k_z)$ can be calculated based on the theory for unconfined films [21], assuming a uniform spatial profile of the magnetization across the

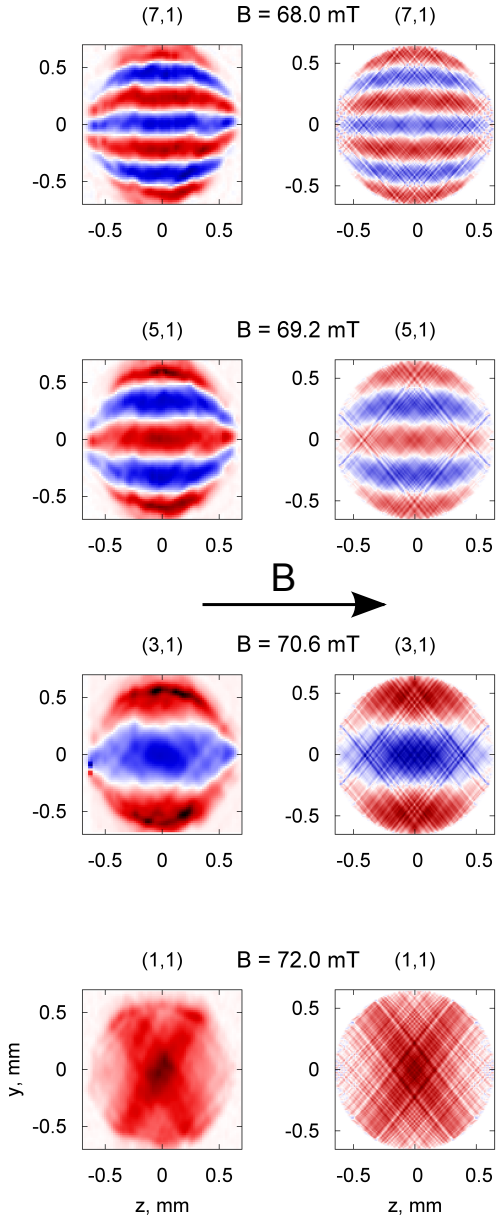

Figure 3.4: Left, experimentally recorded spatial profiles for the fundamental (1,1)-mode as well as for the DE (3,1), (5,1), and (7,1) modes, respectively. Right, corresponding spatial profiles obtained via simulation with OOMMF. The resonance field for each mode at 3.800 GHz is indicated.

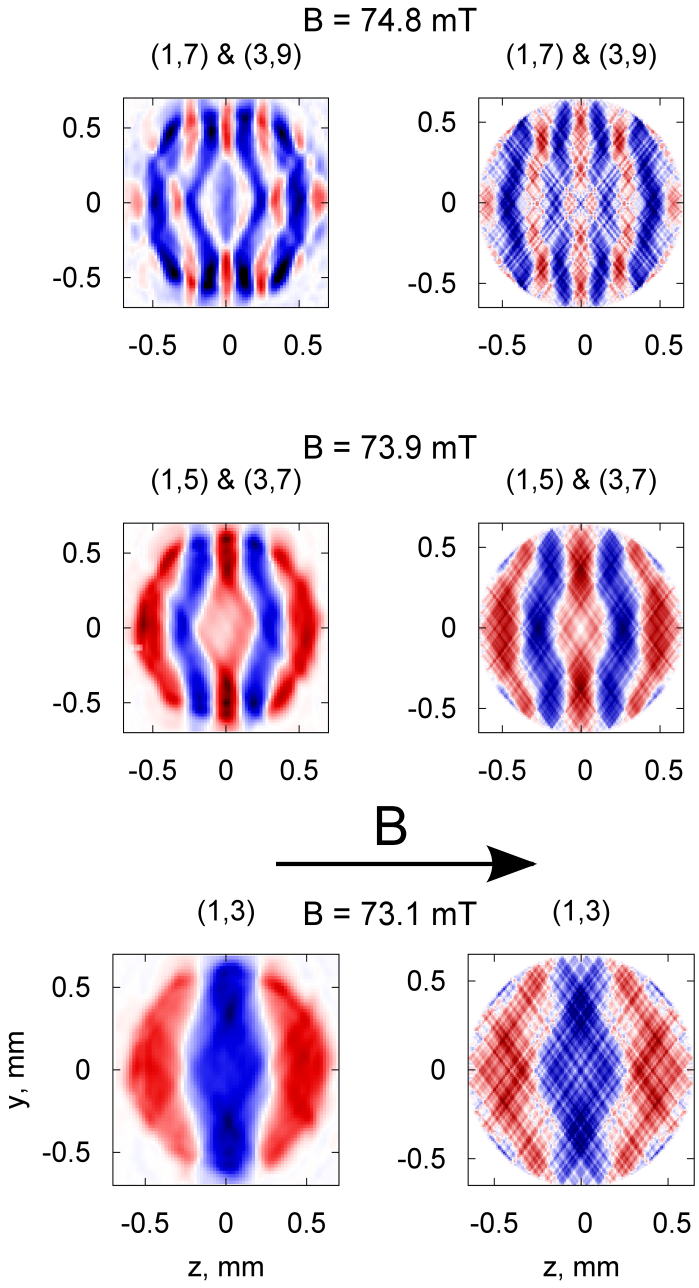

Figure 3.5: Left, experimentally recorded spatial profiles for the BV (1,3), degenerate (1,5), and degenerate (1,7), modes, respectively. Right, corresponding spatial profiles obtained via simulation with OOMMF. The resonance field for each mode at 3.800 GHz is indicated.

film thickness and small thickness of the film, t such that $kt \ll 1$,

$$\nu(k) = \gamma\sqrt{\left(B + \frac{k_y t}{2}\mu_0 M_s \frac{k_z^2}{k_y^2 + k_z^2}\right)\left(B + \mu_0 M_s\left(1 - \frac{k_y t}{2}\right)\right)}. \qquad (3.2)$$

Equation (3.2) describes the spin-wave modes in a particular confined sample, if one introduces the values of k_y and k_z, fulfilling the selection rules for this sample. Since the aspect ratio of the confined sample used in these studies $\frac{t}{d} = 4 \times 10^{-3}$ is small, one can neglect static demagnetizing effects here and consider B as the external magnetic field. To compare the experimental data with the dispersion given by (3.2), one should recall that the dipole interaction results in the pinning boundary conditions for dynamic magnetization at the lateral edges of a confined sample [77]. Therefore, the smallest allowed component of the wavevector in both directions is $\frac{\pi}{d}$, corresponding to the number of antinodes of 1. Taking into account this fact we have calculated the frequencies of the modes for $k = (\frac{n_y\pi}{d}, \frac{n_z\pi}{d})$ as shown in Figure 3.3. Comparing Figure 3.2 and Figure 3.3 one can conclude that this crude analytical model nicely describes the appearance of quantized modes at the fields both below and above the resonance field of the fundamental (1,1) mode. Moreover, Figure 3.3 illustrates a possible degeneracy of different modes, for example of the (1,5) and (3,7) modes. The degeneracy results in a simultaneous excitation of these modes by the microwave field at a given external magnetic field. Space resolved measurements in this case provide a complex profile of the precession which essentially differs from a profile of a single mode (see the inset in Figure 3.3).

Further comparison between the numerical modeling and the experiment can be made based on the mode profiles, as shown in Figure 3.4 and Figure 3.5. Figure 3.4 demonstrates the modes obtained at the magnetic field equal or lower than 72 mT, the resonance field of the fundamental (1,1) mode. We adopt the terminology of the so-called surface Damon-Eshbach (DE) modes as shorthand for describing these modes [18], although the wavevectors characterizing these modes are not exactly perpendicular to the field. Nevertheless, in agreement with this classification alternative changes of the sign $m_\perp(y, z)$ are observed for these modes along the y-directions. The modes can apparently be identified as $(n_y, 1)$-modes, n_y increasing with decreasing field. The situation with the backward volume (BV) modes [18] obtained for $B > 72$ mT is more complex, as illustrated in Figure 3.5 for nominally $(1, n_z)$-modes. On one hand, one observes that the number of antinodes increases with increasing field, as one expects from the negative group velocity of the BV-modes in an unconfined film. On the other hand, comparing the inset in Figure 3.3 with the profile of mode (1,5) in Figure 3.5 one can conclude,

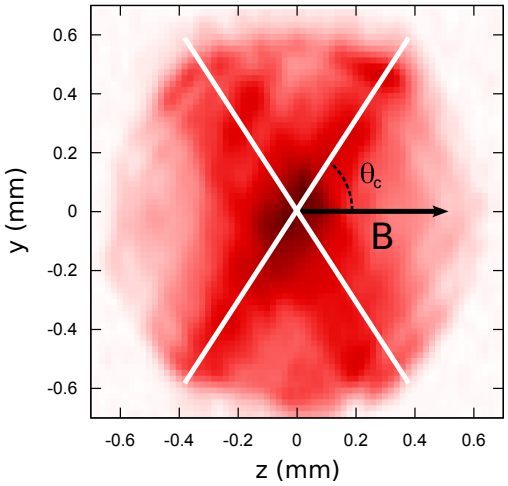

Figure 3.6: Experimentally recorded spatial profiles of the fundamental (1,1) mode. Note the X-like network of straight lines. The white lines correspond to the calculated value of the critical angle $\theta_c = 57°$.

that the profiles presented in Figure 3.5 correspond to a linear combination of two almost degenerate (1,5) and (3,7) modes. Similarly, mode (1,7) can be reproduced as a linear combination of (1,7) and (3,9) modes. At higher fields, the modes become increasingly complex, and are no longer simple linear combinations of two almost degenerate modes.

Concluding this section, let us notice that both experimentally measured and numerically simulated spatial profiles of the modes shown in Figure 3.4 and Figure 3.5 demonstrate X-like networks of crossing straight lines. The origin of the network, exemplarily shown in more detail in Figure 3.6 for the experimentally measured profile of the (1,1)-mode, is scattering of spin waves by defects of the disks. Note here, that the network of rectangular cells used for simulation of a circular disk in micromagnetic calculations results in creation of defects on the contour of the disk. In fact, it is well known [61, 62, 64] that the scattering of spin waves by a point defect results in formation of caustic beams due to a strong anisotropy of their dispersion. The process can be understood as follows: due to the anisotropy of the spin-wave dispersion the phase and the group velocity are not parallel to each other. While for a given frequency the direction of the phase velocity can vary in a wide interval of angles, the group velocity exhibits a certain preferential direction, determined by a critical angle θ_c. The scattering of spin waves by a point defect can be considered as re-radiation conserving the frequency of the wave, but not its wavevector. In this case, the re-

radiated spin waves have the same frequency equal to the frequency of the mode, but different k. Despite the large diversity in the direction of the phase velocity, which is parallel to k, the radiated waves propagate along the preferential directions of the group velocity, which determines the flow of spin-wave energy. Thus, well defined beams along the direction defined by θ_c are built. Using the parameters of the experiment and applying the approach developed in Ref. [61], one can calculated the critical angle $\theta_c = 57°$. The white lines in Figure 3.6 corresponding to the calculated value of θ_c clearly demonstrate a very nice agreement between theory and experiment.

3.3 Conclusion

Using magneto-optical Faraday-microscopy we have imaged and investigated the magnetostatic spin-wave modes in a macroscopic YIG disk magnetized in plane. By sweeping the applied magnetic field at a constant excitation frequency we were able to detect up to 15 both Damon-Eshbach and backward-volume-like modes. Taking advantage of micromagnetic simulations based on the OOMMF software package we were able to reproduce the frequencies of the modes as well as their spatial profiles. Although the modes with small numbers of antinodes can be classified based on the more analytically tractable square-sample geometry, the profiles of the modes with large number of antinodes cannot be modeled as the product of two orthogonal standing waves, or a simple linear combination of almost degenerate modes. Caustic beams are observed on top of the mode profiles for different modes. Experimental results, including the caustic patterns, are convincingly reproduced in micromagnetic simulations.

Chapter 4

Fundamental Eigenmodes of Nonellipsoidal Microscopic Magnetic Elements

4.1 Introduction

This chapter addresses the spin-wave eigenmode spectrum of microscopic $Ni_{80}Fe_{20}$ = Py elements of uniform thickness and various lateral geometries. By means of scanning Kerr effect microscopy (SKEM), we investigate the spatial profile of the spin-wave eigenmodes excited in these elements by an in-plane microwave magnetic field oriented perpendicular to the static saturating magnetic field. Due to the inhomogeneous internal demagnetizing field of nonellipsoidal magnetic elements, the spin-wave dispersion acquires a spatial dependence, resulting in the formation of spin-wave wells. We aim to demonstrate the functionality of the SKEM setup at sub-μm spatial scales and to characterize the spectra and spatial profile of the localized modes in these structures.

4.2 Experiment

The test device in this experiment consists of a set of elements (squares and circles) with lateral dimensions < 3 μm patterned by e-beam lithography and ion-beam etching from a 20 nm thick film of Py. The elements are located on top of a 6.2 μm wide, 200 nm thick Au microstrip transmission line used for the excitation of the magnetization dynamics. The dynamic magnetic field h created by the current was perpendicular to the direction of the static magnetic field $H = 1100$ Oe oriented along the microstrip transmission line.

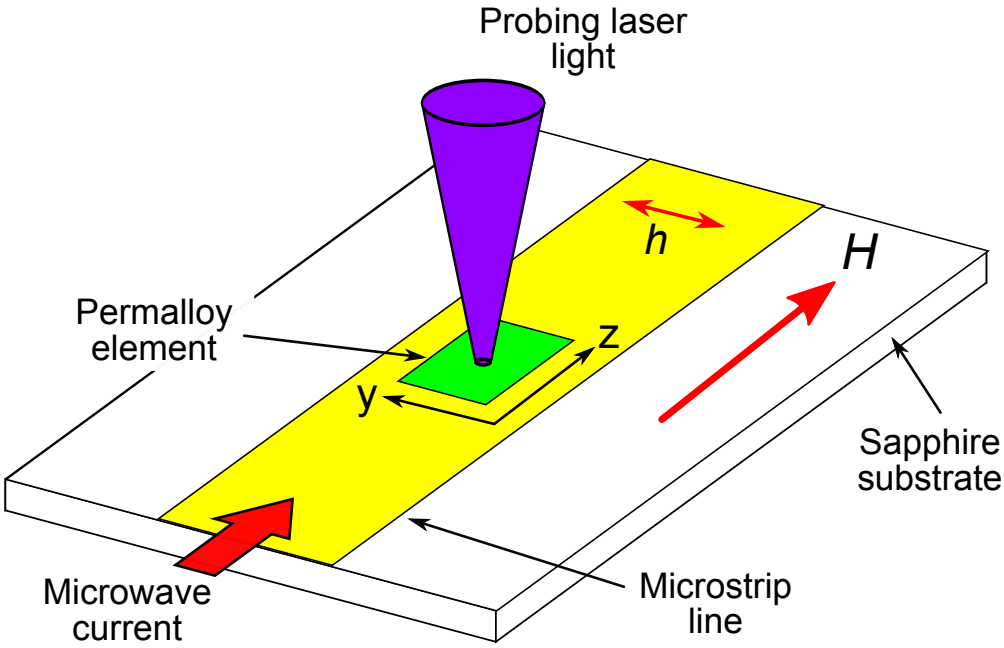

Figure 4.1: Schematic of the experimental setup.

Thus the conditions for excitation of FMR are fulfilled. Figure 4.1 shows a schematic of the experimental setup. The local detection of the magnetization dynamics was performed using scanning Kerr effect microscopy (SKEM). By synchronization of the femtosecond laser pulses with the excitation current, the waveform of the magnetization response can be captured over one entire cycle of the excitation current. Repeating this process over the sample yields phase-resolved, two-dimensional maps of the magnetization, with resolution limited by the laser spot size, here ≈ 250 nm. For more details, refer to chapter 2.

In magnetic elements with ellipsoidal shape, the internal magnetic field is uniform [9, 12]. Due to demagnetizing effects [78], nonellipsoidal microscopic thin-film magnetic elements support two types of eigenmodes: dipole-dominated center modes spread over the entire area of the element and exchange-dominated edge modes localized in the narrow spatial regions close to the edges, where the internal magnetic field is reduced [71, 135]. These regions of high inhomogeneity of the internal field create potential wells for spin-waves. Since the internal field at the position of the edge modes is much smaller than the applied field due to stron demagnetizing effects, these modes can be excited at frequencies below the quasi-uniform FMR mode, depending on the material parameters and degree of reduction of the internal field.

To determine the spectrum of eigenmodes in the square and circular elements, we first placed the focused laser spot at the center of the element, and measured the out-of-plane component of the dynamic magnetization as a function of the frequency of the microwave magnetic field. In order to synchronize the probing laser pulses with the microwave current, the frequency resolution of the setup is limited to 80 MHz. The filled blue regions in Figure 4.2 and Figure 4.3 show the results of the measurements for the square and circular element, respectively. Both spectra exhibit dominant peaks corresponding to the quasi-uniform FMR mode, supplemented by subsidiary peaks lying above the quasi-uniform mode indicated by arrows. In correspondence with the results of chapter 3, we expect these peaks to comprise Damon-Eshbach type modes [18].

Now, we measure the spectra again, placing the laser spot at the edge of the elements. The filled red regions in Figure 4.2 and Figure 4.3 show the results of the measurements for the square and circular element, respectively. As expected, we observe the emergence of a new mode, at a frequency (≈ 6 GHz) far below that of the quasi-uniform mode. We expect these peaks to correspond to so-called edge modes, excited by the excitation current in spin-wave wells located near the edge of the sample.

Similar to μBLS, SKEM measures magnetization dynamics in the frequency domain, with resolution in real space. In other words, by setting

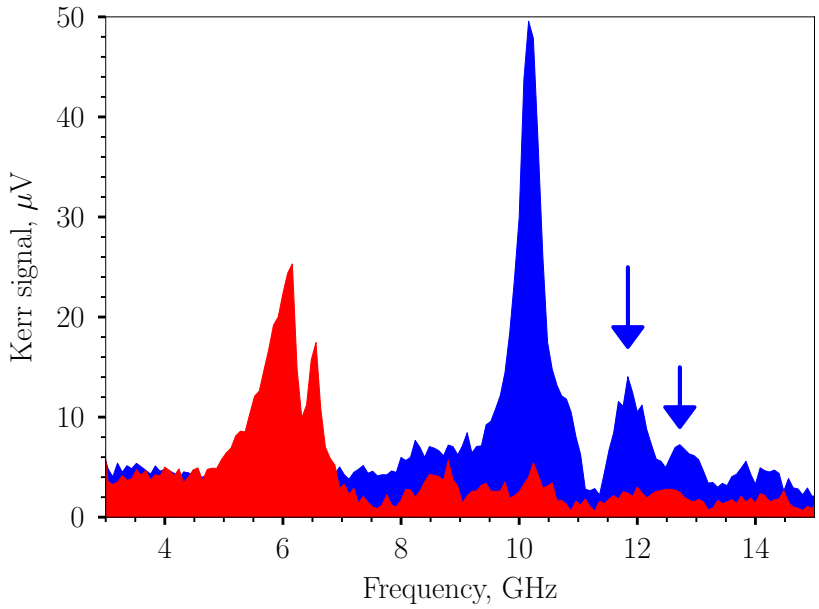

Figure 4.2: Resonant curves of the center (blue) and edge (red) modes in the square element. The power of the microwave current $P = 10$ mW.

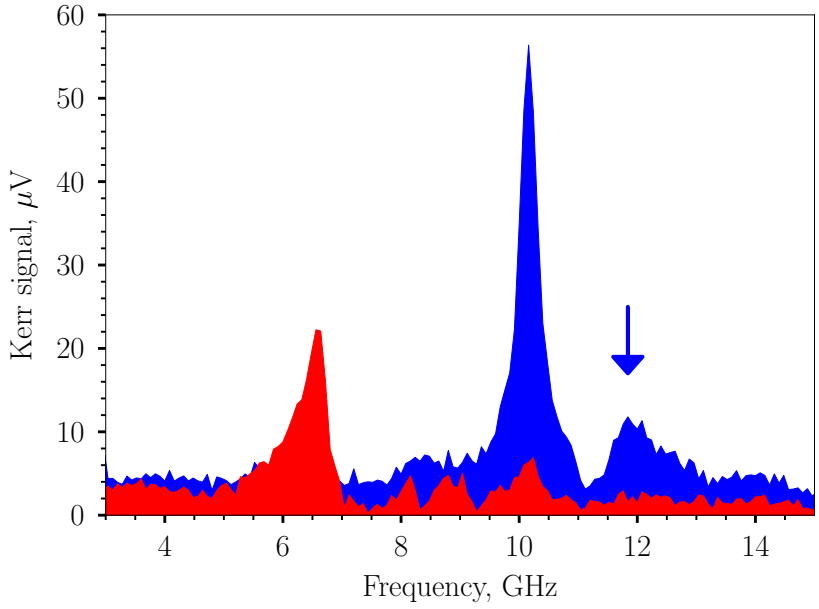

Figure 4.3: Resonant curves of the center (blue) and edge (red) modes in the circular element. The power of the microwave current $P = 10$ mW.

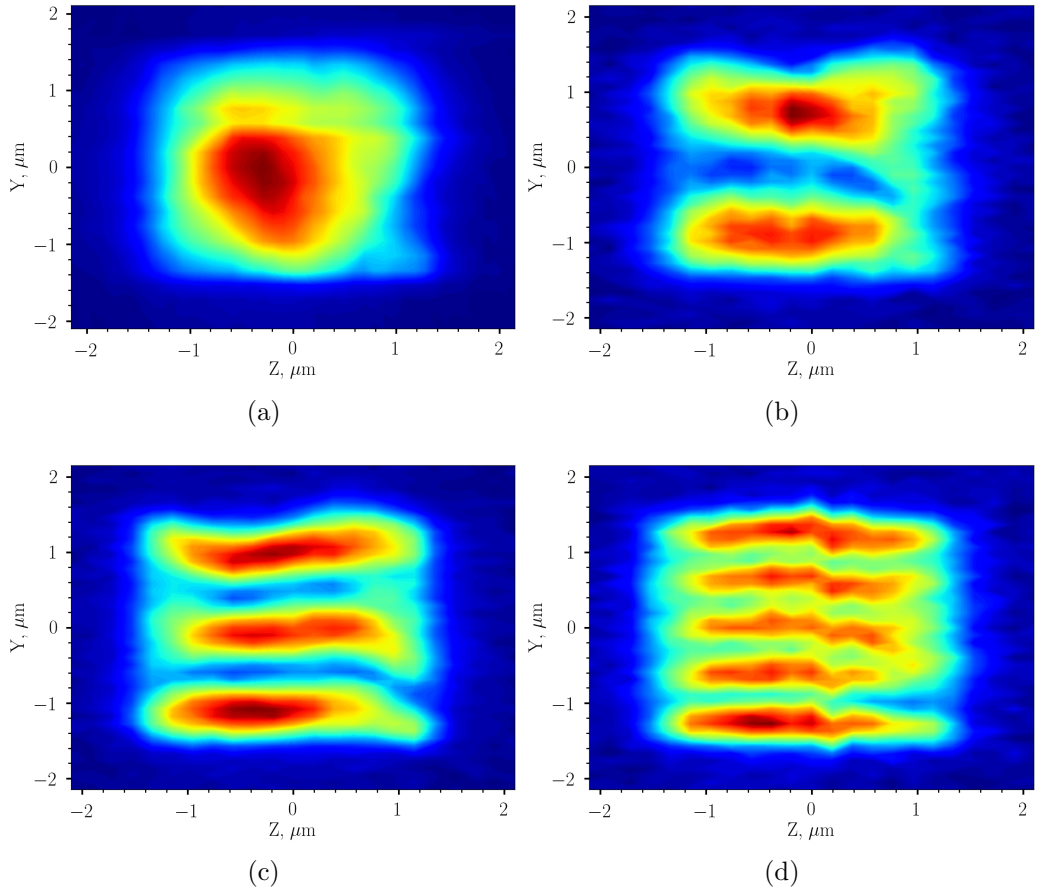

Figure 4.4: (a)–(d) Pseudocolor-coded maps of the normalized Kerr signal proportional to the out-of-plane component of the dynamic magnetization in the square element for frequency of the microwave current $f_{mw} = 10.16$, 11.20, 11.84, and 12.72 GHz, respectively. The power of the microwave current $P = 100$ mW. These modes correspond to the quasi-uniform FMR mode and higher-order Damon-Eshbach type modes.

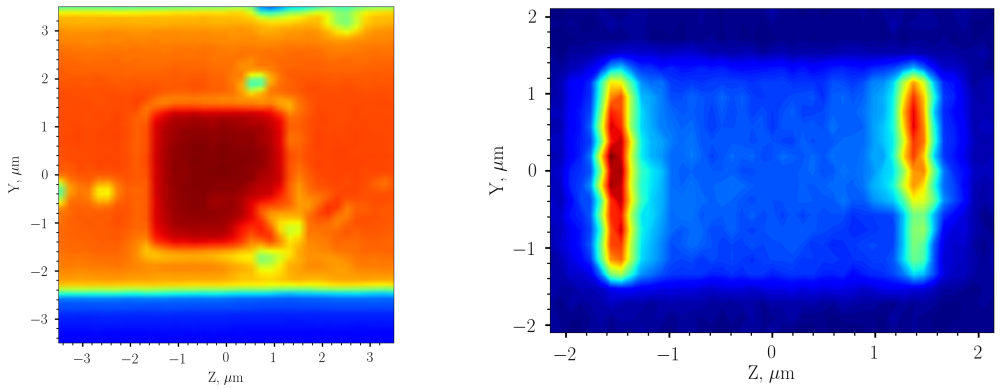

(a) (b)

Figure 4.5: (a) Topographical real space image of the square magnetic element. (b) Pseudocolor-coded maps of the normalized Kerr signal proportional to the out-of-plane component of the dynamic magnetization in the square element for frequency of the microwave current $f_{mw} = 6.56$ GHz. The power of the microwave current $P = 100$ mW. The formation of the spin-wave well along the edge of the element is hindered by the presence of the lithographical defects.

the excitation current to the spectral peaks, we may scan the laser over the sample and obtain real space images of the eigenmodes. Figure 4.4 shows the results of such measurements at spectral maxima obtained from measurements at the center of the square sample. The real space profile of the modes corresponds qualitatively to previous results on macroscopic YIG samples [136].

If we now tune the excitation current to the edge spectral peaks, we may image the edge modes in real space. Figure 4.5 shows the resultant spatial profile of the magnetization, as well as a real space image of the magnetic element. Since the localization of edge modes depends strongly on the profile of the internal magnetic field and thus the sample geometry, sample defects may modify or prohibit the formation of spin-wave wells. In the current element, lithographical defects at the corner of the element prevent the formation of a spin-wave well in the affected region, which can be clearly observed from the measurement of the spatial profile of the magnetization of the edge mode.

We may repeat analogous measurements on the circular element, yielding real space images of the spin-wave eigenmodes shown in Figure 4.6. The higher order Damon-Eshbach type modes exhibit strong qualitative agreement with the results of chapter 3 on macroscopic YIG samples; in order to respect the circular geometry of the element, the modes develop a spatial

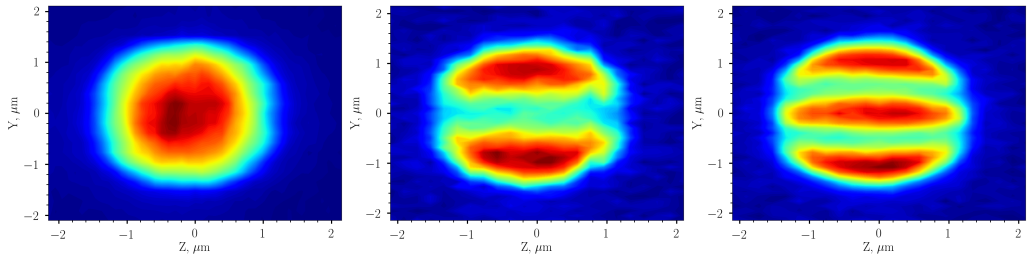

(a) (b) (c)

Figure 4.6: (a)–(c) Pseudocolor-coded maps of the normalized Kerr signal proportional to the out-of-plane component of the dynamic magnetization in the circular element for frequency of the microwave current $f_{mw} = 10.16$, 11.12, 11.84 GHz, respectively. The power of the microwave current $P = 100$ mW. These modes correspond to the quasi-uniform FMR mode and higher-order Damon-Eshbach type modes.

dependence of the in-plane wavevector. For comparison, we plot the (5,1) modes from the current element and the macroscopic YIG disk of chapter 3 side-by-side in Figure 4.7. This correspondence is an experimental verification of the scaling arguments presented in chapter 3. Finally, we observe the appearance of two edge modes in the circular samples. As shown in Figure 4.8. the first corresponds to strong localization at the edges of the circle lying along the external static field, in agreement with recent studies of these modes [137]. The second, at slightly higher frequencies, corresponds to a slight delocalization of the modes in the field-transverse direction, forming stripes reminiscent of the square element.

4.3 Conclusion

In conclusion, we have characterized the spectrum of spin-wave excitations in microscopic Py elements with square and circular lateral geometries. Together the quasi-uniform and higher order center modes and the localized edge modes constitute the fundamental eigenmodes of microscopic magnetic elements. Utilizing the frequency and spatial resolution of the SKEM setup, we have been able to image both the center and edge modes with diffraction-limited spatial resolution. Our results exhibit strong qualitative agreement with previous measurement on macroscopic YIG samples.

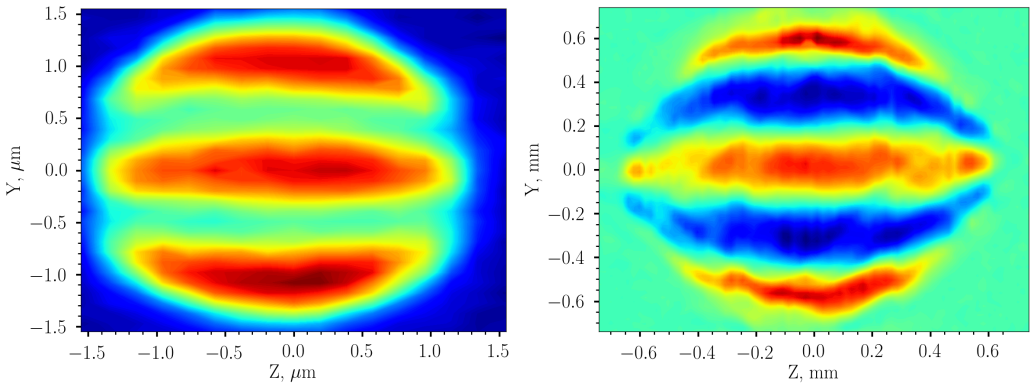

(a) (b)

Figure 4.7: (a) (5,1) Damon-Eshbach type mode in the circular Py element. (b) Corresponding (5,1) mode from the YIG disk in chapter 3.

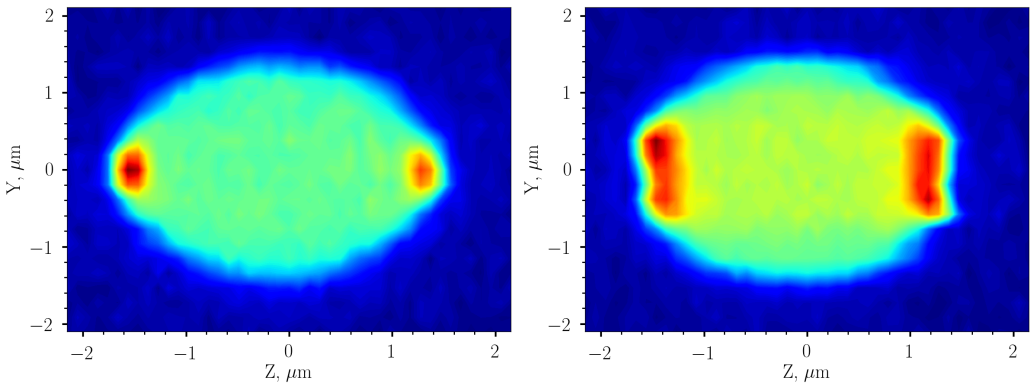

(a) (b)

Figure 4.8: (a)–(c) Pseudocolor-coded maps of the normalized Kerr signal proportional to the out-of-plane component of the dynamic magnetization in the circular element for frequency of the microwave current $f_{mw} = 6.16$, 8.80 GHz, respectively. The power of the microwave current $P = 100$ mW. These modes correspond to the edge modes occupying the spin-wave wells at the element edges.

Chapter 5

Control of Magnetic Fluctuations by Spin Current

5.1 Introduction

This chapter addresses the thermal spin-wave spectrum in a microscopic, in-plane magnetized Py disk under the influence of STT. The Py disk is part of a spin Hall system comprised of the Py disk fabricated on top of a Pt strip connected to a transmission line. We use the unprecedented sensitivity of μBLS to study the magnetization dynamics in the Py disk in the presence of dc current in the Pt strip, without external microwave excitation. Via the spin Hall effect in the Pt strip, this dc current results in a pure spin current, whic transfers angular momentum to the magnetic system in the Py disk and modifies the thermal spin-wave spectrum. In this experiment, we use μBLS to characterize the effect of the spin current on the magnetic fluctuations in the Py disk.

5.2 Experiment

The test device in this experiment consists of a 5nm thick, 2μm in diameter Py disk deposited on top of a 10nm thick, 2.8 μm wide Pt strip connected to a transmission line. In contrast to typical multilayer STT devices, this test device configuration enables optical access to the surface of the Py disk. We can, therefore, use μBLS to probe the magnetization dynamics in the Py disk, with a sensitivity capable of detecting the thermal spin-wave spectrum. Figure 5.1 shows a schematic of the experimental setup. Measurements are made by varying the dc current applied to the Pt strip, with a static magnetic field $H_0 = 900$ Oe applied in the plane of the Py disk, perpendicular to the

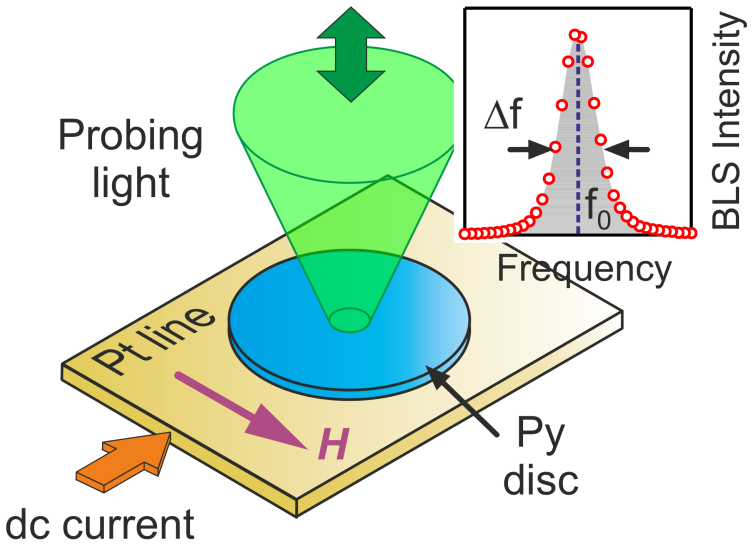

Figure 5.1: Schematic of the experimental setup.

direction of current in the Pt strip. In all measurements, we use μBLS to probe the magnetization dynamics in a 250nm-diameter spot at the center of the Py disk.

Microscopically, the operation of the device relies on a transverse spin current generated due to the spin-Hall effect (SHE) in the Pt strip, as shown schematically in Figure 5.2. This transverse spin current transfers angular momentum to the magnetic system of the Py disk via STT. Theoretically, the current-induced excitation is most efficient when the magnetization in the Py disk is perpendicular to the electric current in the Pt strip, corresponding to a spin-polarization of the spin-current parallel or anti-parallel to the magnetization. Thus, the excitation depends on the relative direction of the applied field and current, changing signs if either (a) the magnetic field H is rotated 180 degrees or (b) the current polarity is reversed [103].

Figure 5.3 shows a pseudocolor logarithmic plot of the BLS intensity as a function of current and frequency. Note here that the BLS intensity is proportional to the fluctuation energy of a given mode. As seen in Figure 5.3, the presence of electrical current in the Pt strip strongly modifies the magnetic fluctuations, characterized by the peak height of the BLS signal, and this dependence is asymmetric with respect to the current direction. For $I > 0$, the intensity of the peak monotonically decreases with increasing I, while its central frequency depends weakly on I. In contrast, for $I < 0$, the

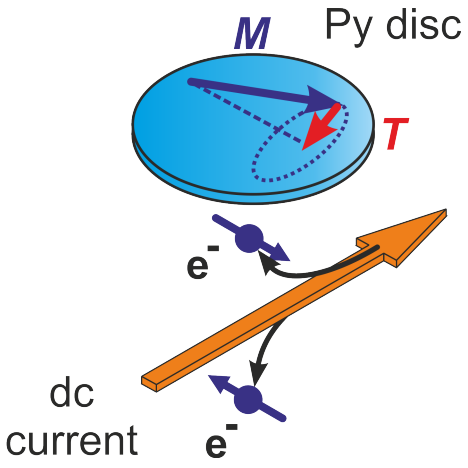

Figure 5.2: Schematic of the SHE-induced spin current.

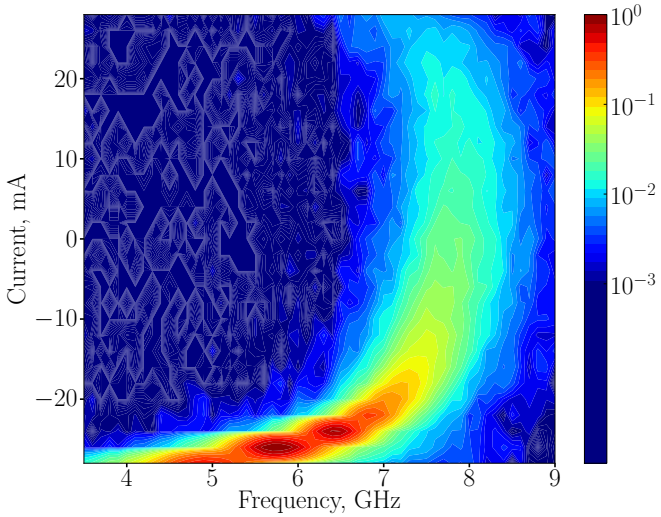

Figure 5.3: Pseudocolor logarithmic plot of the normalized BLS intensity vs. current and frequency.

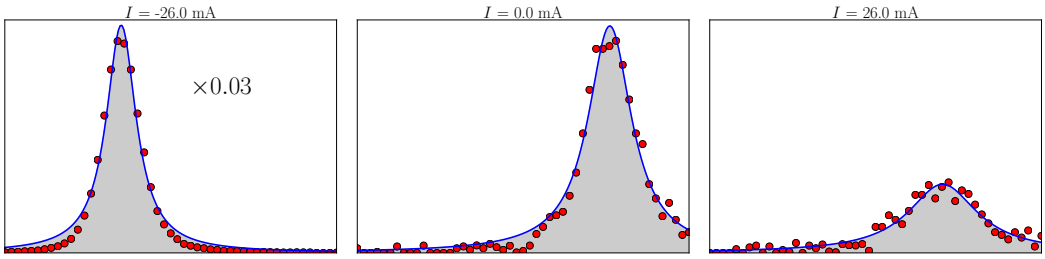

Figure 5.4: BLS spectra acquired at I = (a) -26 mA, (b) 0 mA, and (c) 26 mA. Curves are Cauchy-Lorentz fits to the experimental data.

intensity of the peak increases with increasing I and the central frequency exhibits a dramatic redshift at $I <$ -26 mA.

To quantitatively characterize these tendencies, we fit the measured BLS spectra to a Cauchy-Lorentz distribution,

$$L(f) = \frac{a}{1 + \left(\frac{(f-f_0)}{b}\right)^2},$$

where $a = L(f_0)$ gives the peak height at the central frequency f_0 and the full width at half maximum is given by FWHM $= 2|b|$. The BLS spectra at three different currents, I = -26, 0, 26 mA are shown in Figure 5.4. The fit is plotted as a line in Figure 5.4, and we obtain excellent agreement between the experimental data and the corresponding Cauchy-Lorentz distributions: we find mean uncertainties for f_0, Δf, and $L(f_0)$ of $< 1\%$, 4%, and 3%, respectively.

We can therefore use the fits $L(f)$ to characterize the current dependence of the BLS spectra. As discussed in Chapter 1, the frequency width Δf of the BLS spectrum is proportional to the magnetic damping in the system, captured phenomenologically by the Gilbert damping parameter α. In Figure 5.5, we plot the full width at half-maximum Δf versus current. The linear variation of Δf at small current values $|I| < 10$ mA is consistent with the previously documented linear effects of STT on the magnetic damping [42]. This variation corresponds to partial compensation ($I < 0$) or enhancement ($I > 0$) of the magnetic damping.

In contrast, the behavior of the integral intensity, as shown in Figure 5.6, reveals essentially new behavior. From Chapter 1 recall that, the μBLS signal at a given frequency is proportional to the spectral density of fluctuations. Hence, the integral of the BLS peak over all frequencies is proportional to the

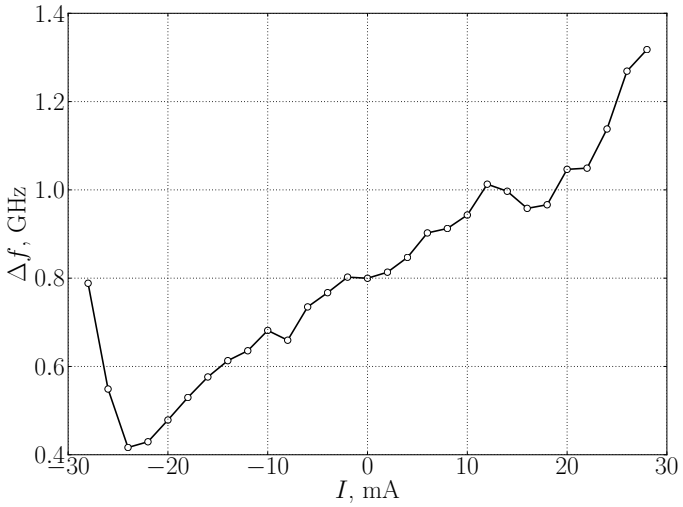

Figure 5.5: The full width at half maximum Δf of the BLS spectra vs. current, obtained from Cauchy-Lorentz fits to the experimental data. Lines are a guide for the eye. Note that, $\Delta f \propto \alpha$ where α is the dimensionless, phenomenological Gilbert damping parameter.

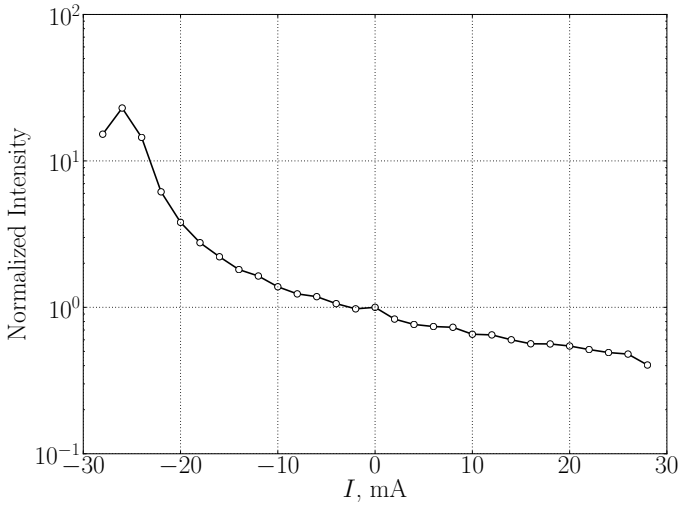

Figure 5.6: Normalized BLS integral intensity vs. current, calculated from Cauchy-Lorentz fits to the experimental data. Lines are a guide for the eye.The BLS integral intensity is proportional to the average fluctuation energy of the FMR mode.

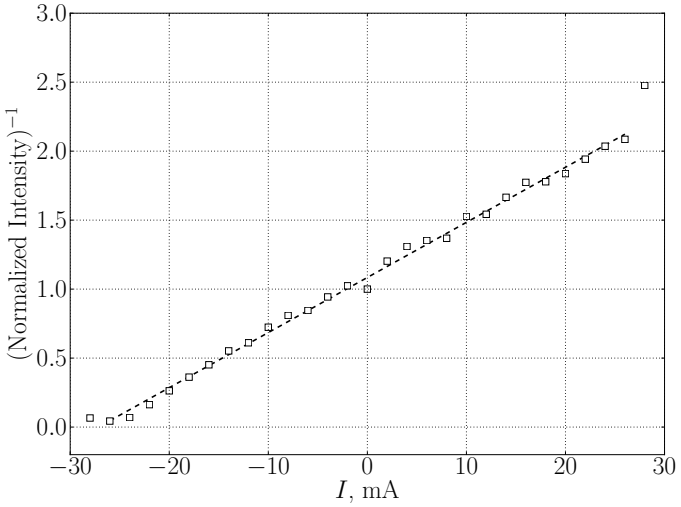

Figure 5.7: Normalized inverse integral intensity vs. current, calculated from Cauchy-Lorentz fits to the experimental data. The dashed line is a linear fit to the data.

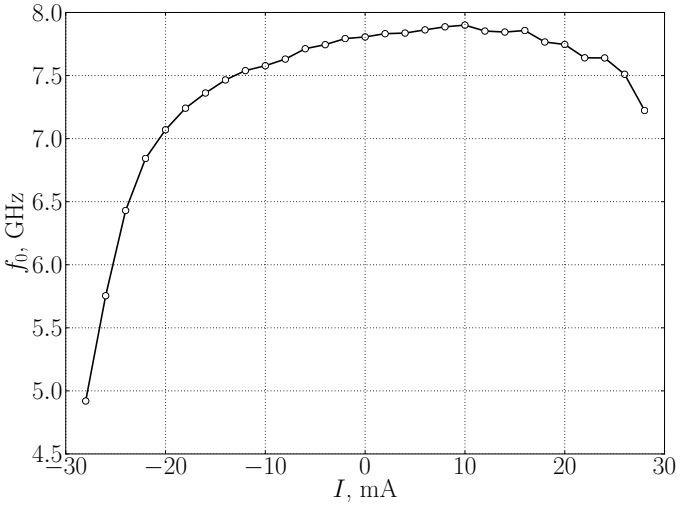

Figure 5.8: Peak central frequency vs. current, obtained from Cauchy-Lorentz fits to the experimental data. Lines are a guide for the eye.

average fluctuation energy of the FMR mode. According to the fluctuation-dissipation theorem, this energy is a function of the temperature and the mode frequency but is independent of the mode damping. If STT simply results in a modified damping of the FMR mode, then, in the classical limit, the fluctuation-dissipation theorem implies that the average fluctuation energy would remain k_BT, independent of the magnitude of the current [84].

Figure 5.6 shows that the integral intensity of the BLS spectra depends strongly on the current, varying by nearly two order of magnitudes over the current range from -26 mA to 26 mA. This dependence is asymmetric with respect to the current direction, and the integral intensity saturates at current values $I <$ -26 mA.

These results clearly demonstrate that STT drives the system into a nonequilibrium state. Moreover, the linear behavior of the inverse integral intensity (Figure 5.7) is consistent with theoretical predictions that the inverse of the average energy in each mode scales linearly with current [138]. Thus, the current-dependence of the BLS integral intensity provides a straightforward experimental illustration that a modified-α model of STT is incorrect.

Extrapolating a linear fit to the inverse intensity suggests that at $I =$ -28 mA the integral intensity can be expected to diverge, indicating the onset of auto-oscillations in the system. Instead, the integral intensity saturates at $I =$ -26 mA and begins to decrease, concomitant with a rise in the linewidth Δf as seen in Figure 5.5. The increasing linewidth suggests additional current-dependent contributions to the magnetic damping α, while the saturated integral intensity indicates the onset of amplitude-limiting relaxation processes.

As shown in Figure 5.8, the central frequency f_0 exhibits a dramatic redshift for $I < 0$, which we attribute to a decrease of the effective magnetization M_e due to increased magnetic fluctuations. In fact, for this orientation of the current, the angular momentum transferred to the system is antiparallel to the angular momentum associated with the static magnetization. This spin-current should destabilize the system and amplify the fluctuations. We use the Kittel formula [9] to determine M_e from our measurements of f_0,

$$f_0^2 = \gamma^2 H(H + 4\pi M_e)$$

where γ is the gyromagnetic ratio and $H = H_0 + H_I$ the magnetic field corrected by the Oersted field of the dc current. As shown in Figure 5.9, the resulting dependence of M_e on I exhibits a monotonic decrease at $I <$ -26 mA.

The saturation of the integral intensity, in contrast to the monotonic decrease of M_e, is attributed to the mode-dependent effect of STT on the

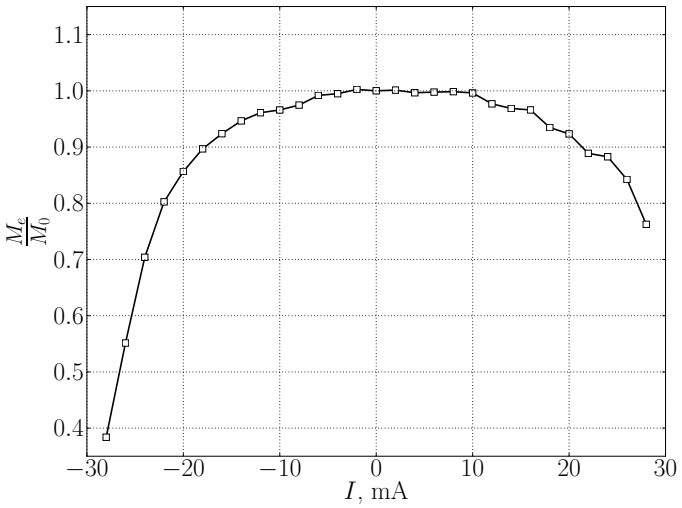

Figure 5.9: Calculated effective magnetization normalized by its value M_0 at $I = 0$ vs. current, calculated from the magnetic field H corrected by the Oersted field of the current and the peak central frequency f_0 obtained from Cauchy-Lorentz fits to the experimental data. Lines are a guide for the eye. The effective magnetization characterizes the total fluctuation intensity of the entire spin-wave ensemble.

spin-wave amplitude. μBLS is selectively sensitive to long-wavelength fluctuations, while the reduction of M_e characterizes the total fluctuation intensity of the entire spin-wave ensemble, here dominated by the large phase volume of short-wavelength spin waves. The saturation of the integral intensity and the monotonic decrease of M_e can be explained by a disproportional enhancement of different spin-wave modes. As the current approaches the critical value, short-wavelength fluctuations are continuously enhanced, while the intensity of long-wavelength fluctuations saturates. In the measurements, the enhancement of short-wavelength fluctuations manifests in the monotonic decrease of M_e while the saturation of long-wavelength fluctuations results in the saturation of the BLS integral intensity.

We therefore distinguish between three regimes characterizing the effect of dc current on the BLS integral intensity. First, for $I > 0$, the current reduces the BLS integral intensity, defining the fluctuation-suppression regime. For $-26 < I < 0$, we observe a steady growth of the integral intensity, which saturates at I = -26 mA. These current values constitute the pre-saturation fluctuation-enhancement regime. Finally, for $I <$ -26 mA, we observe a saturation of the BLS integral intensity. As previously discussed, comparison with the monotonic decrease of M_e at $I <$ -26 mA reveals that this saturation stems from the enhancement of short-wavelength fluctuations. This regime we term the post-saturation fluctuation-enhancement regime.

To further investigate the effects contributing to these phenomena, in particular in order to separate the effects of STT from those of Joule heating, we performed time-resolved BLS measurements of fluctuations in the presence of 1 μs long current pulses with a 5 μs repetition period. As shown in Figs. 5.10–5.12, we investigate the temporal evolution of M_e and the integral intensity for three current values I = 25, -25, and -30 mA corresponding to the fluctuation-suppression, pre-saturation fluctuation-enhancement, and post-saturation fluctuation-enhancement regimes, respectively.

For I = 25 mA, see Figure 5.10, the BLS integral intensity rapidly decreases by a factor of 2 at the onset of the pulse, remains constant over the pulse duration, then rapidly rises again to the original value at the end of the pulse. The time scale for these intensity variations is shorter than the 20 ns resolution limit of the measurement. In contrast, M_e exhibits a gradual exponential decrease at the beginning of the pulse, followed by a similar slow relaxation after its end, characterized by a time constant $\tau \approx 90$ ns.

To understand this behavior, one needs to consider different time scales associated with STT and Joule heating. The time scale for STT effects determined by the magnetic relaxation rate is typically a few nanoseconds. On the other hand, the time scale for the Joule heating is determined by the much slower rate of heat diffusion away from the device. Therefore,

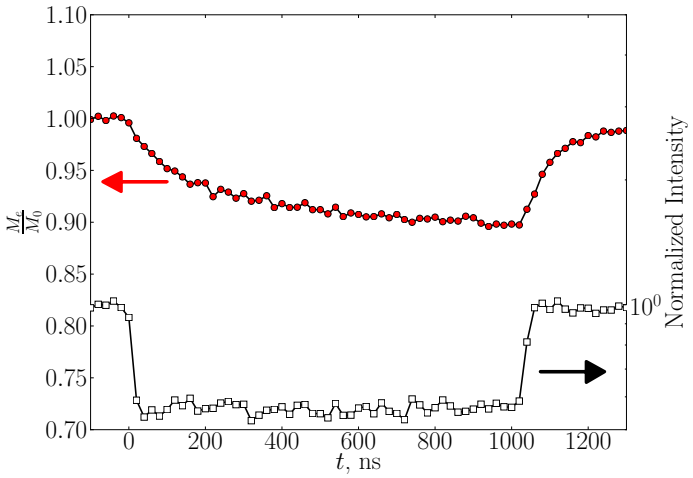

Figure 5.10: Temporal evolution of the normalized effective magnetization and normalized integral BLS peak intensity in the fluctuation-suppression regime. Lines are a guide for the eye. A 1 μs-long pulse of current I = 25mA has been applied at t = 0.

we conclude that in the fluctuation-suppression regime, the long-wavelength part of the fluctuation spectrum is rapidly cooled by STT, while the total intensity of the fluctuations dominated by short-wavelength modes is slowly enhanced due to Joule heating.

As shown in Figure 5.11, for I = -25 mA, in the pre-saturation fluctuation-enhancement regime, the temporal evolution of M_e and the integral intensity is qualitatively different. M_e rapidly decreases at the onset of the pulse and subsequently continues to slowly decrease. At the end of the pulse, M_e first rapidly increases , then continues to relax with a time constant $\tau \approx 90$ ns. The rapid increase of M_e at the end of the pulse can be attributed to the relaxation of the magnetic system with the lattice. This process is characterized by the spin-lattice relaxation rate of a few nanoseconds. The subsequent slow relaxation of M_e is associated with the simultaneous cooling of the lattice and the magnetic system. Therefore, by comparing the magnitudes of the fast and slow variations of M_e at the end of the pulse, we conclude that the contribution of the Joule heating to the total enhancement of fluctuations does not exceed 30%.

Comparing Figure 5.11 and Figure 5.12, one can observe that the temporal evolution of M_e is similar for I = -25 mA and I = -30 mA. However, the evolution of the BLS integral intensity shows different behavior in the pre-

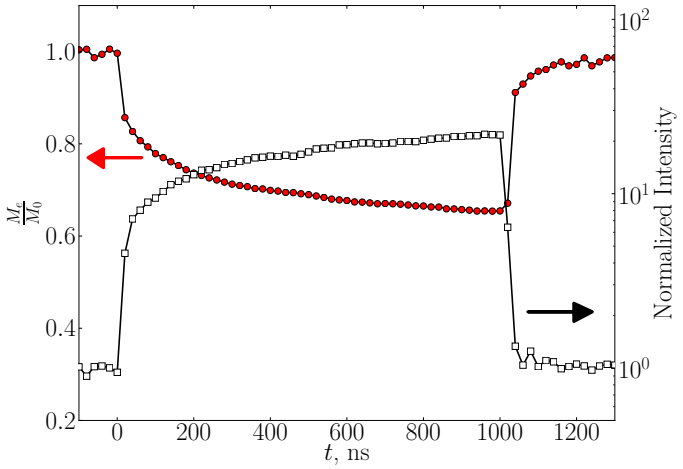

Figure 5.11: Temporal evolution of the normalized effective magnetization and normalized integral BLS peak intensity in the pre-saturation fluctuation-enhancement regime. Lines are a guide for the eye. A 1 μs-long pulse of current I = -25mA has been applied at t = 0.

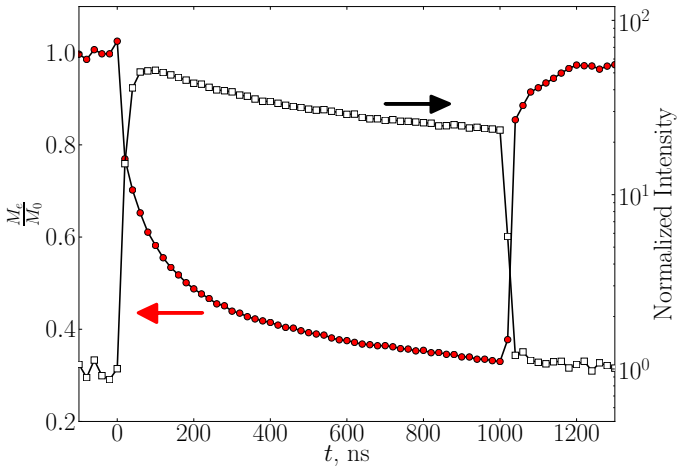

Figure 5.12: Temporal evolution of the normalized effective magnetization and normalized integral BLS peak intensity in the post-saturation fluctuation-enhancement regime. Lines are a guide for the eye. A 1 μs-long pulse of current I = -30mA has been applied at t = 0.

and post-saturation fluctuation-enhancement regime. At I = -25 mA, the integral intensity rapidly increases at the onset of the pulse then continues to slowly rise. At I = -30 mA, the intensity initially rapidly increases but then slowly decreases over the rest of the pulse duration.

We conclude that the different temporal behaviors indicate the appearance of a nonlinear dynamical mechanism, which also explains the saturation of the integral intensity in the static measurements for $I < -26$ mA. Since the initial increase of the integral intensity at I = -30 mA is significantly larger than at I = -25 mA, it is the subsequent slow variation that results in the saturation in the static measurements for $I < -26$ mA.

Comparing the temporal evolution of M_e and the integral intensity, we conclude that the fluctuations of both the long- and short-wavelength modes are initially significantly more enhanced at $I = -30$ mA than at $I = -25$ mA, resulting in stronger nonlinear magnon-magnon scattering that redistributes the energy within the fluctuation spectrum. While the details of these scattering processes are yet unknown and inaccessible by our experimental technique, they can generally be expected to drive the magnetic subsystem towards a thermal distribution [139], thus suppressing the intensity of the FMR-mode fluctuations close to the critical current and preventing the onset of auto-oscillation.

5.3 Conclusion

Concluding this chapter, let us emphasize that the discovered suppression of magnetic thermal fluctuations can be used for noise suppression. In fact, the main source of noise in GMR and/or TMR sensors is the magnetic fluctuations. We have therefore shown that pure spin currents represent a potential mechanism to improve the figures of merit of spintronic devices.

Chapter 6

Wide-range control of ferromagnetic resonance by spin Hall effect

6.1 Introduction

This chapter addresses ferromagnetic resonance in a microscopic, in-plane magnetized Py disk under the influence of STT. The Py disk is part of a spin Hall system comprised of the Py disk fabricated on top of a Pt strip connected to a matched transmission line. Additionally, a thin Cu spacer layer between the Pt strip and Py disk has been added to reduce interfacial spin-orbit scattering. By means of a bias tee, we simultaneously apply dc current and microwaves to the Pt strip. Using μBLS, we measure the ferromagnetic resonance characteristics of the Py disk in the presence of dc current in the Pt strip. We aim to show that the SHE constitutes a practical mechanism of control of the ferromagnetic resonance characteristics in the Py disk.

6.2 Experiment

The test device in this experiment consists of a 5nm thick, 2μm in diameter Py disk deposited on top of a 10nm thick, 2.4 μm wide Pt strip connected to a matched transmission line. In addition, a 2nm thick Cu spacer layer has been deposited between the Pt strip and Py disk. In previous experiments on similar systems, strong spin-orbit scattering at the Pt/Py interface resulted in a magnetic relaxation rate significantly larger than in free Py films [103,104]. In the current experimental configuration, the weak spin-orbit coupling of the Cu spacer reduces this scattering at the Py/Cu interface [140].

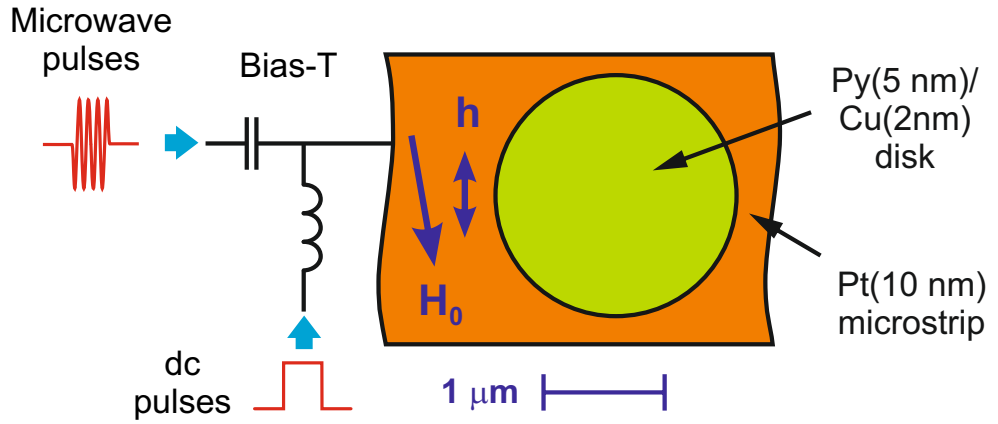

Figure 6.1: Schematic of the experimental setup.

As in the experiment of chapter 5, the operation of the device relies on a transverse spin current generated due to the spin Hall effect (SHE) in the Pt strip. This transverse spin current transfers angular momentum to the magnetic system of the Py disk via STT. By means of a bias tee, we simultaneously apply pulses of dc current and microwave pulses to the Pt strip. In this way, we measure the characteristics of FMR excited by the microwave magnetic field in the presence of dc current in the Pt strip.

A schematic of the experimental setup is shown in Figure 6.1. A static magnetic field H_0= 900 Oe is applied in the plane of the Py disk, at an angle of 80° with respect to the axis of the Pt strip. dc current was applied constant or in 100ns-long pulses with a repetition period of 2μs to reduce Joule heating. Microwaves with a peak power of 1mW were applied in 100ns-long pulses synchronized to the dc current pulses. We use mBLS to probe the magnetization dynamics in a 250 nm diameter spot at the center of the Py disk. This local detection technique eliminates the inhomogeneous broadening of the measured FMR curves.

Figure 6.2a and 6.2b show FMR peaks recorded for different values of the dc current I applied constant and pulsed, respectively. The curves have been recorded by varying the frequency of the microwave pulses from 7 to 10GHz while recording the BLS intensity at the same frequency. The peak characteristics depend strongly on the magnitude of I and its direction. For large $|I|$, the central frequency f_0 exhibits a redshift. For $I < 0$, this redshift is accompanied by an increase of the peak intensity and decrease in the

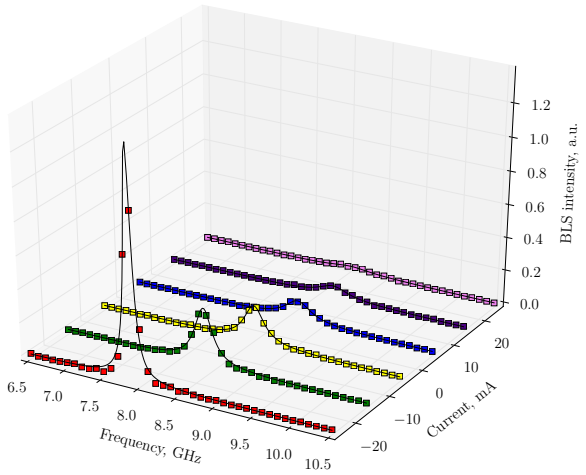

(a)

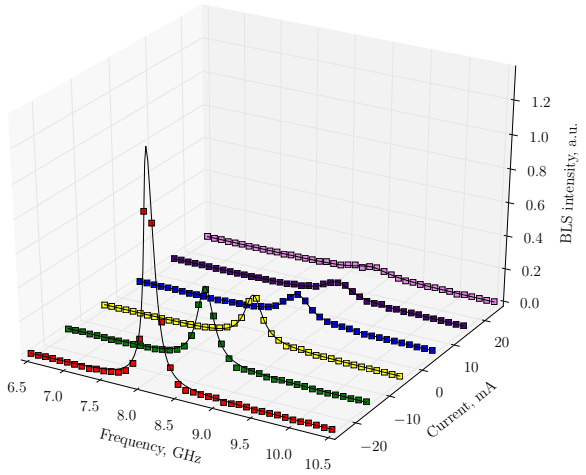

(b)

Figure 6.2: Normalized FMR peaks measured as a function of current I applied (a) constant (b) in pulses to the Pt strip. Curves are Cauchy-Lorentz fits to the experimental data.

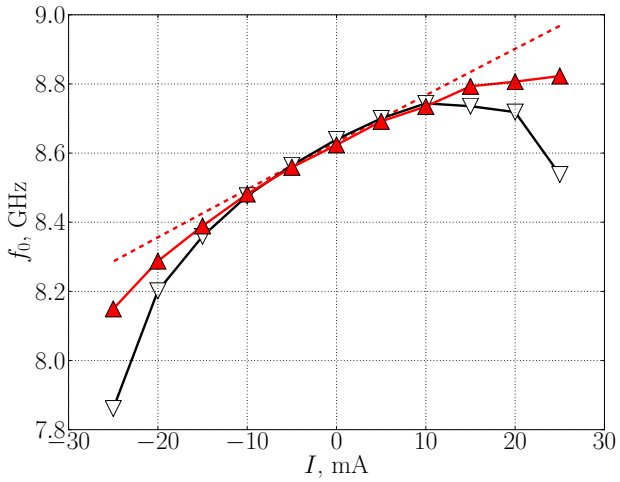

Figure 6.3: Current dependence of the FMR frequency. Open symbols denote measurements with constant current, filled symbols measurements with pulsed current. Lines are guides for the eye. Dashed line shows the calculated variation of the FMR frequency due solely to the Oersted field of the dc current.

peak width. For the opposite current polarity, $I > 0$, the peak intensity monotonically decreases and the peak broadens.

For each current, the FMR peak is fit to a Cauchy-Lorentz distribution, plotted as curves in Figure 6.2. We obtain excellent agreement between the experimental data and the best-fit distribution.[1] Using the fits of the data to the Cauchy-Lorentz distribution, we determine the dependence of the peak characteristics on the dc current. Figure 6.3 and Figure 6.4 show the central frequency f_0 and spectral width Δf as a function of current, respectively. Open symbols represent measurements made with constant current, closed symbols measurements with pulsed current. As in the experiment of chapter 5, the FMR frequency f_0 exhibits nonlinear variation with respect to the current I due to the influence of Joule heating, STT, and the Oersted field $\vec{H}_I$ of the current. The dashed line in Figure 6.3 shows the FMR frequency calculated using the Kittel formula [9],

$$f_0 = \gamma\sqrt{H(H + 4\pi M_0)}, \tag{6.1}$$

[1]Fits of the BLS spectra to Cauchy-Lorentz distributions give mean uncertainties for f_0, Δf, and $L(f_0)$ of $< 1\%$, 4%, and 3% for constant current and $< 1\%$, 3%, and 3% for pulsed current.

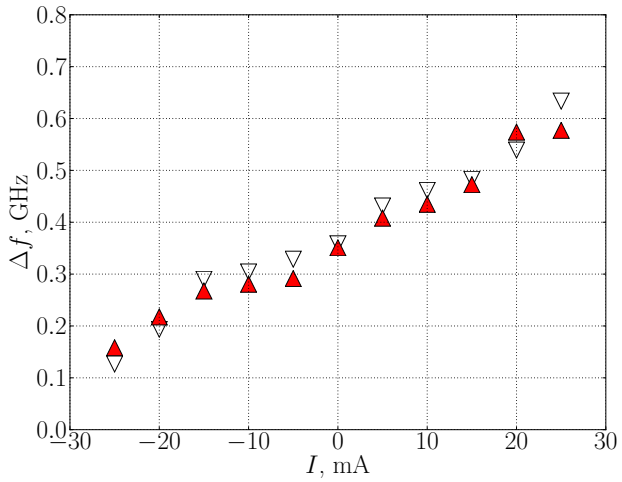

Figure 6.4: Current dependence of the spectral width of the FMR peak, obtained from Cauchy-Lorentz fits to the experimental data. Open symbols denote measurements with constant current, filled symbols measurements with pulsed current.

where γ is the gyromagnetic ratio, $4\pi M_0 = 9660$ G the saturation magnetization experimentally determined from the FMR frequency at zero current, and $H = |\vec{H}_0 + \vec{H}_I|$. The experimental data for both constant and pulsed current vary linearly for small $|I|$, indicating that the variations of f_0 at small $|I|$ are dominated by the Oersted field. With increasing $|I|$, the experimental dependencies deviate from the calculation based on the assumption of a constant M_0, indicating contributions from the variation of the effective magnetization M_e due to STT and Joule heating.

In order to differentiate between the contributions of Joule heating and STT to the FMR peak characteristics, we apply the dc current in low-duty sub-μs pulses. Joule heating occurs on a time scale determined by heat diffusion away from the device, i.e. on a micro- or milli-second time scale, whereas STT influences the magnetization dynamics on a time scale set by the magnetic relaxation rate, typically several nanoseconds. Therefore, the effect of Joule heating on data recorded by applying pulsed dc current should be greatly reduced. Comparing the constant/pulsed current datasets in Figure 6.3, we conclude that heating significantly affects the FMR frequency at large $|I|$. In contrast, as shown in Figure 6.4 the FMR peak's spectral width, characterizing the magnetic damping in the system [50], does not depend on whether the current is constant or pulsed. Therefore, the dependence of Δf

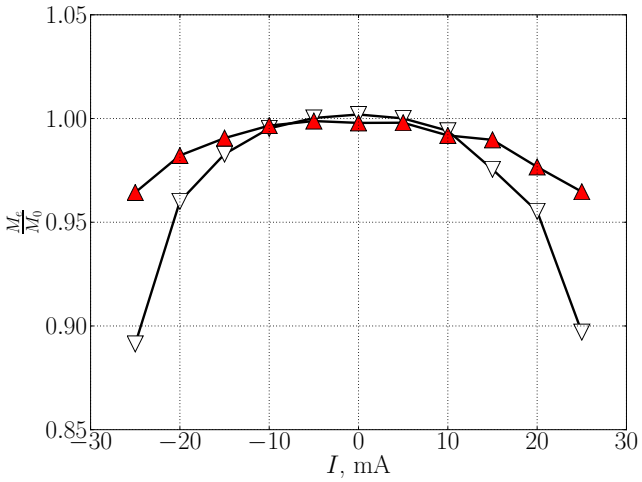

Figure 6.5: Current dependence of the effective magnetization normalized by its value at $I = 0$. Open symbols denote measurements with constant current, filled symbols measurements with pulsed current. Lines are guides for the eye.

on the current can be attributed entirely to STT.

The current dependency of the effective magnetization M_e and effective Gilbert damping parameter α can be determined from the measured FMR curves. To determine $M_e(I)$, we substitute $M_e(I)$ for M_0 in the Kittel formula (Equation 6.1) and use the measured data for f_0 (Figure 6.3) to extract $M_e(I)$, which is plotted in Figure 6.5. The calculated dependence $M_e(I)$ for constant current is significantly different from the pulsed-current calculation, and in both cases is nearly symmetric with respect to $I = 0$. Therefore, we conclude that this dependence is dominated by Joule heating.

To determine $\alpha(I)$, we use

$$\alpha = \frac{\Delta f}{2\gamma(H + 2\pi M_e)} \tag{6.2}$$

derived from the Landau-Lifshitz-Gilbert (LLG) equation taking into account the demagnetization effects for an in-plane magnetized ferromagnetic film [50]. Inserting the calculated $M_e(I)$, the calculated H, and the data for $\Delta f(I)$, we obtain $\alpha(I)$.

The value $\alpha(I = 0) = 0.011$ is close to the standard value $\alpha = 0.008$ for Py [141], demonstrating that the effect of Pt on the damping in Py is minimized by the Cu spacer. The dependence $\alpha(I)$ is the same for constant

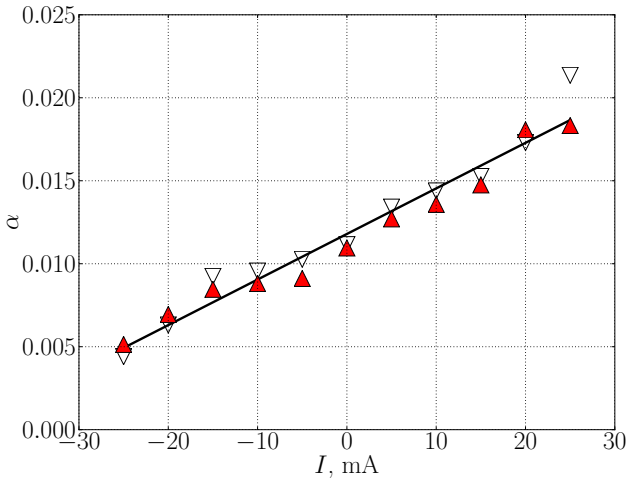

Figure 6.6: Current dependence of the Gilbert damping constant. Solid line is a linear fit to the data. Open symbols denote measurements with constant current, filled symbols measurements with pulsed current.

and pulsed current and does not contain a symmetric component. Therefore, this dependence is dominated by STT. This conclusion is also consistent with the linear dependence of α on current shown in Figure 6.6, as expected for the effect of STT on the magnetic damping.

Moreover, over the studied range of I, α changes by a factor of 4, and the smallest achieved value $\alpha = 0.004$ is reduced by a factor of 2 compared to the standard value for Py. This current-induced reduction demonstrates that the SHE can be utilized as an efficient and practical mechanism for controlling the dynamical characteristics of ferromagnets.

Finally, we analyze the effect of dc current on the amplitude of the coherent magnetization excited by the microwave magnetic field. As seen from Figure 6.2, the amplitude of the FMR peak increases for negative I and decreases for positive I. This variation can be expected from the current dependence of α, resulting in the variation of the resonant dynamic susceptibility of the system. To take this variation into account, we compare the experimentally obtained amplitude of the FMR peak with that calculated based on the LLG equation and the experimetnally determined dependencies $\alpha(I)$ and $M_e(I)$, as illustrated in Figure 6.7 for the case of constant negative current. These data show that the measured amplitude increases with I faster than one expects from the LLG equation with variable damping constant, i.e. STT not only reduces α but also amplifies the dynamic

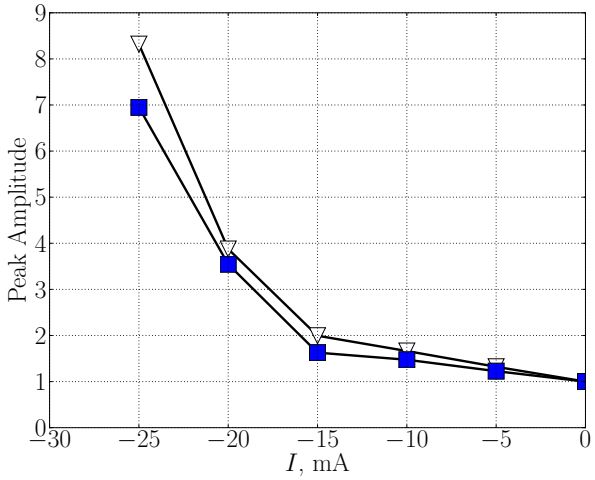

Figure 6.7: Current dependence of the amplitude of the FMR peak for constant current normalized by its value at $I = 0$. Open symbols show the measured amplitude. Filled symbols show the amplitude calculated using the LLG equation and the experimental data for α and M_e. Lines are guides for the eye.

magnetization. As in the experiment of chapter 5 in the case of incoherent magnetization dynamics, these results demonstrate amplification of coherent magnetization dynamics.

To characterize this result quantitatively, in Figure 6.8 we plot the current dependence of the amplification factor defined as the ratio of the measured to the calculated amplitude of the FMR peak. A systematic linear variation of the amplification factor with current is clearly seen in Figure 6.8. In particular, the dynamic magnetization is amplified at $I < 0$ and suppressed for $I > 0$.

6.3 Conclusion

In conclusion, by means of μBLS, we have investigated the ferromagnetic resonance characteristics of a Pt-Py spin Hall system, modified by the introduction of a 2 nm Cu spacer layer. By analyzing the FMR characteristics as a function of current and differentiating between datasets obtained with dc current applied constant and in pulses, we were able to delimit the effects of STT and Joule heating on the dynamics in the Py disk. Furthermore, we observed a two-fold reduction of the Gilbert damping in the Py disk from

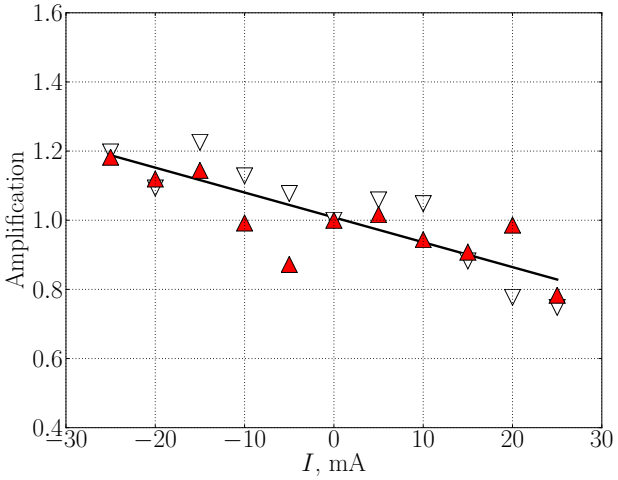

Figure 6.8: Current dependence of the amplification factor, defined as the ratio of the measured data to the calculated amplitudes of the FMR peak for constant (open symbols) and pulsed (filled symbols) dc current. Solid line is a linear fit to the data.

its standard value due to STT. Measurements at zero dc current confirm the salutary effect of the Cu spacer layer on the damping in Py. Lastly, by comparing the amplitudes of the observed resonance peaks with theoretical resonance peaks calculated on the basis of the LLG-equation with modified Gilbert damping, we have observed amplification of the coherent magnetization dynamics.

Chapter 7

Stimulation of parametric instability in magnetic microdots by pure spin currents

7.1 Introduction

This chapter addresses parametric resonance in a microscopic, in-plane magnetized Py disk under the influence of STT. The Py disk is part of a spin Hall system comprised of the Py disk fabricated on top of a Pt strip connected to a matched transmission line. Additionally, a thin Cu spacer layer between the Pt strip and Py disk has been added to reduce interfacial spin-orbit scattering. By means of a bias tee, we simultaneously apply dc current and microwaves to the Pt strip. Using μBLS, we observe the onset of the parametric spin-wave instability as a function of the power and frequency of the microwave magnetic field, under the influence of pure spin current generated from the dc current by the SHE in the Pt strip. We aim to demonstrate that by using pure spin currents of a given polarization one can essentially reduce the threshold power of the microwave pumping necessary to achieve the parametric instability, as well as to control the frequency characteristics of the instability region at the given pumping strength.

7.2 Experiment

The test device in this experiment consists of a 5 nm thick, 2 μm in diameter $Ni_{80}Fe_{20}$ = Permalloy (Py) dot fabricated on top of a 10 nm thick and 2.4 μm wide Pt line connected to Au microwave transmission lines. The Py dot is separated from the Pt line by a 2 nm thick Cu spacer to reduce the

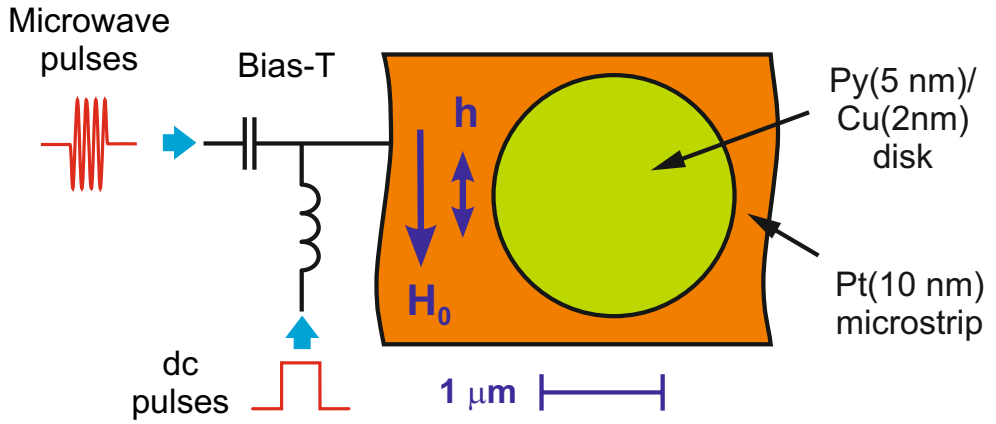

Figure 7.1: Schematic of the test device geometry and experimental setup.

detrimental influence of Pt on the damping in Py. Microwave current creating a dynamic magnetic field, which serves as the parametric excitation, was applied through the Pt line together with direct electric current I. Due to the SHE, the latter induces the pure spin current at the interface with Py exerting spin-transfer torque (STT) on its magnetization. Both microwave and dc currents were applied in short pulses to reduce the Joule heating. dc pulses had duration of 500 ns, whereas microwave pulses had duration of 100 ns and were delayed with respect to the onset of current pulses by 300 ns. The repetition period was 2 μs. The schematic of the experiment is shown in Figure 7.1.

The static magnetic field $H = 900$ Oe was applied in the plane of the sample perpendicular to the axis of the Pt line. In this configuration the dynamic magnetic field h created by microwave current in the Pt line is parallel to the static field. Therefore, the dynamic field does not excite the linear ferromagnetic resonance. Instead, the dynamic field h at the frequency f_p represents a periodic modulation of the parameter of the system—the static magnetic field. It is known [50, 142] that such modulation results in a reduction of the effective magnetic damping of magnetization oscillations at the frequency $\frac{f_p}{2}$. With the increase of the applied microwave power P, the damping can be completely compensated leading to the excitation of magnetization oscillations at the frequency $\frac{f_p}{2}$ (the so-called parametric instability). Since the parametric instability requires the complete damping compensation, this process can only develop starting from a certain threshold value of the pumping

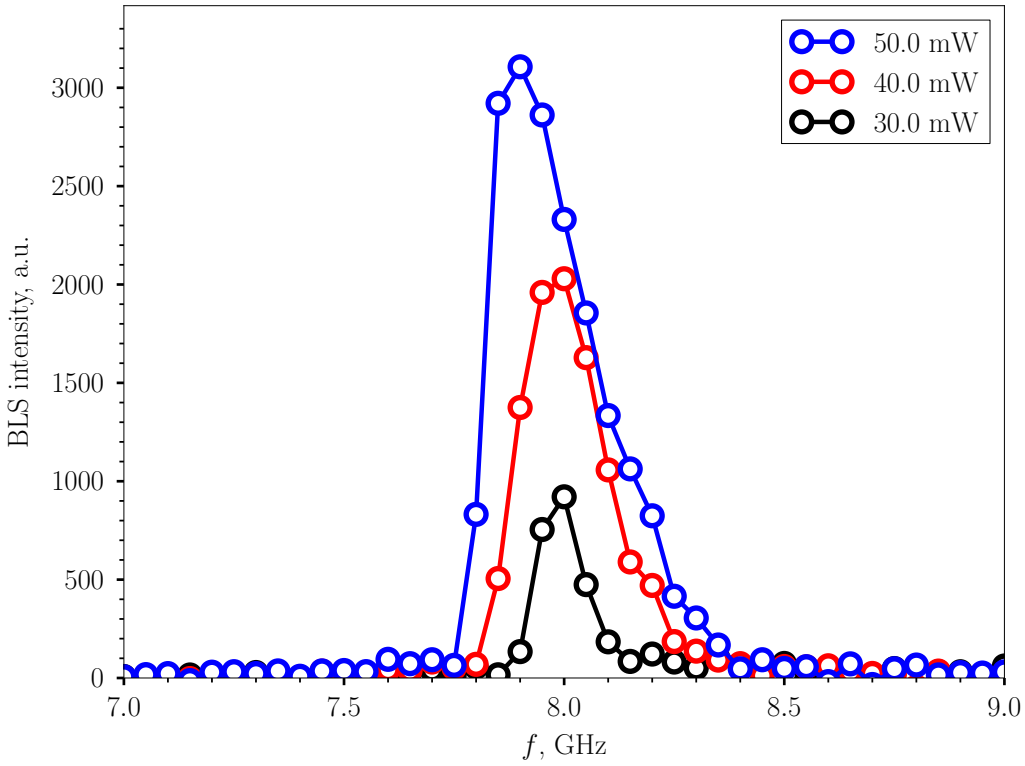

Figure 7.2: Typical example of the spectra of magnetization oscillations excited due to the parametric instability for different values of the parametric pumping power measured as a function of the detection frequency of the interferometer $f = \frac{f_p}{2}$. The data was obtained for $I = 20$ mA.

power P_{th} determined by the relaxation characteristics of the system.

The parametrically excited magnetization dynamics was detected by using micro-focus BLS (μBLS) with the probing laser light focused into a diffraction-limited spot at the center of the Py dot, yielding a signal proportional to the square of the amplitude of dynamic magnetization at this location. When combined with pulsed coherent microwave excitation, the technique provides the frequency resolution better than 50 MHz and the temporal resolution down to 1 ns.

The measurements were first performed in the absence of the dc current ($I = 0$). Under these conditions no parametric instability was observed for pumping powers P up to the maximum used value of 50 mW, which indicates that without injection of the spin current, the dynamic damping in the Py dot is too large to be completely compensated by the parametric process at moderate levels of the pumping power. Then, the measurements were repeated for different non-zero values of I and different dc current directions. Starting from $I \approx 12$ mA, clear signatures of the parametric instability were detected. In agreement with the symmetry of SHE [103], the instability was only observed for positive I corresponding to the STT reducing the effective magnetic damping in the system for the given direction of the static field H.

Figure 7.2 shows a typical example of the spectra of magnetization oscillations excited due to the parametric instability at different values of the pumping power P and $I = 20$ mA. The spectra were recorded by varying f_p in the range from 14 to 18 GHz with the step size of 100 MHz and simultaneously recording the BLS intensity proportional to the square of the amplitude of dynamic magnetization at the frequency $f = \frac{f_p}{2}$. The measured spectra exhibit a resonant excitation of magnetization oscillations at frequencies close to the independently determined frequency of the low-amplitude quasi-uniform ferromagnetic resonance (FMR) in the Py dot $f_{FMR} = 8.49$ GHz. The lowering of the resonant frequency with respect to f_{FMR} is mainly associated with the reduction of the static magnetization caused by the spin current, as well as with the Oersted field of the driving current in the Pt line. With the increase of P, the resonant peak shifts toward smaller frequencies, broadens, and becomes noticeably asymmetric, which are behaviors typical for the parametric resonance [143].

Figure 7.3 summarizes the results of the spectroscopic measurements. It shows the color-coded dependences of the BLS intensity on the frequency $f = \frac{f_p}{2}$ and the pumping power P for $I = 15$, 17.5, 20, 22.5, and 25 mA. The points in the graphs mark the boundaries of the instability region for the given pumping power, defined as points in the spectra of parametrically excited oscillations, where the oscillation intensity falls below 20% of the maximum detected value. The width of the instability region generally increases with

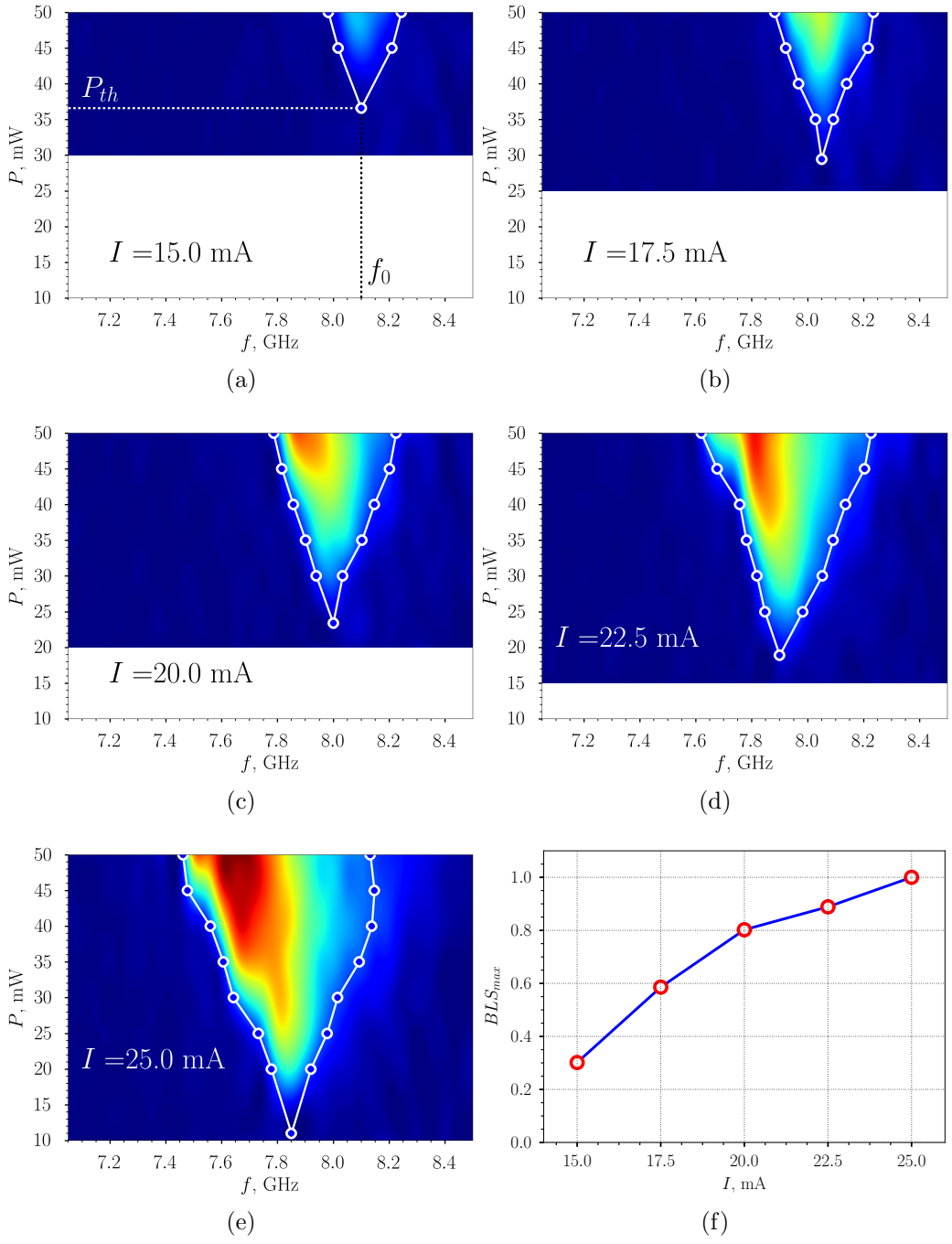

Figure 7.3: (a)–(e) Color-coded dependences of the BLS intensity at the frequency $f = \frac{f_p}{2}$ and the pumping power P for different values of dc current I as indicated. Points in the graphs mark the boundaries of the instability region. Lines are a guide for the eye. (f) Maximum BLS intensity vs. current, normalized by value at $I = 25$ mA.

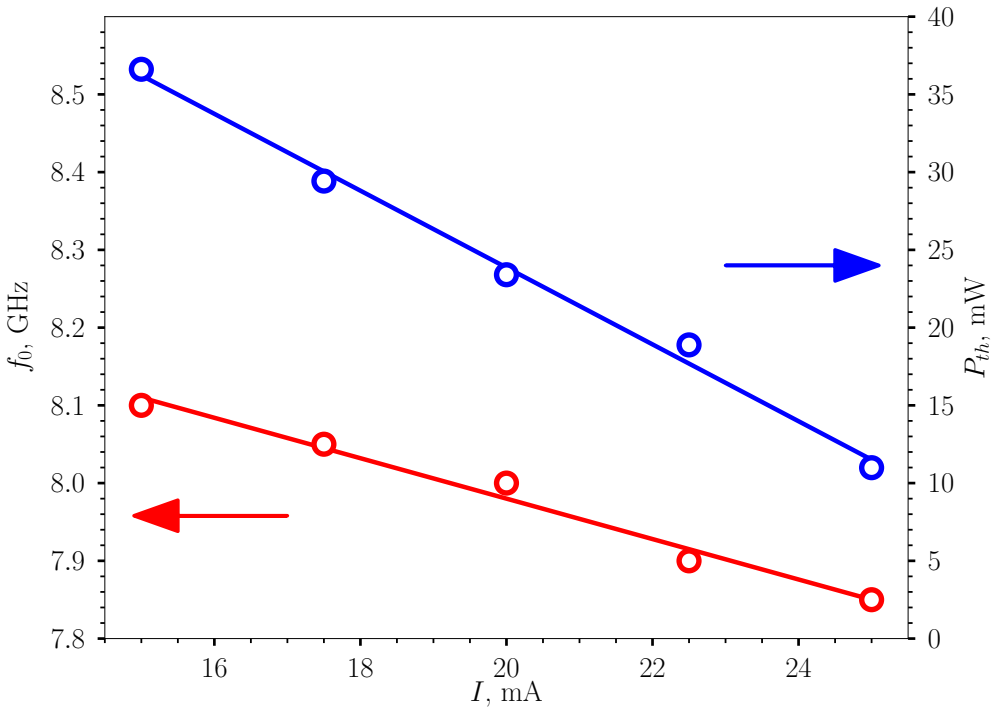

Figure 7.4: Current dependences of the threshold pumping power P_{th} and the frequency of the parametrically excited magnetization oscillations at the onset of the parametric instability f_0. Curves are linear fits to the data.

the increase of the pumping power P and vanishes, as P decreases toward the threshold value P_{th}, being determined by the dynamic magnetic damping in the Py microdot. Correspondingly, P_{th} decreases with the increase of I reflecting the reduction of the effective damping by the spin current.

Quantitative characteristics of the observed behaviors are presented in Figure 7.4-Figure 7.6. As seen from Figure 7.4, the threshold power P_{th} decreases by about a factor of 4 with I increasing from 15 to 25 mA. From this data it is clear that, in agreement with our observations, the parametric instability cannot be achieved in the studied system with moderate pumping powers without injection of the spin current, since for $I < 10$ mA the threshold power is expected to be above 50 mW. The frequency of parametrically excited oscillations at the onset of the instability f_0 decreases with the increase of I nearly linearly, suggesting that the main contribution to its

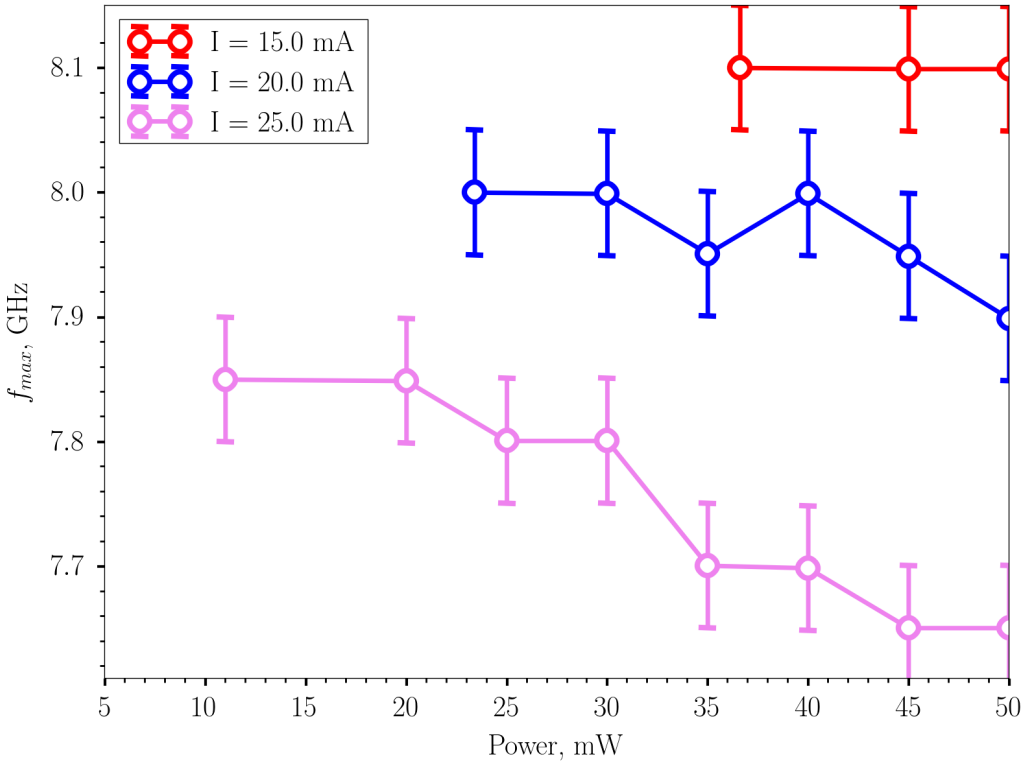

Figure 7.5: Dependences of the frequency of the maximum intensity f_{max} of the parametrically excited magnetization oscillations on the pumping power for different strengths of the direct current I, as labeled. Lines are guides for the eye.

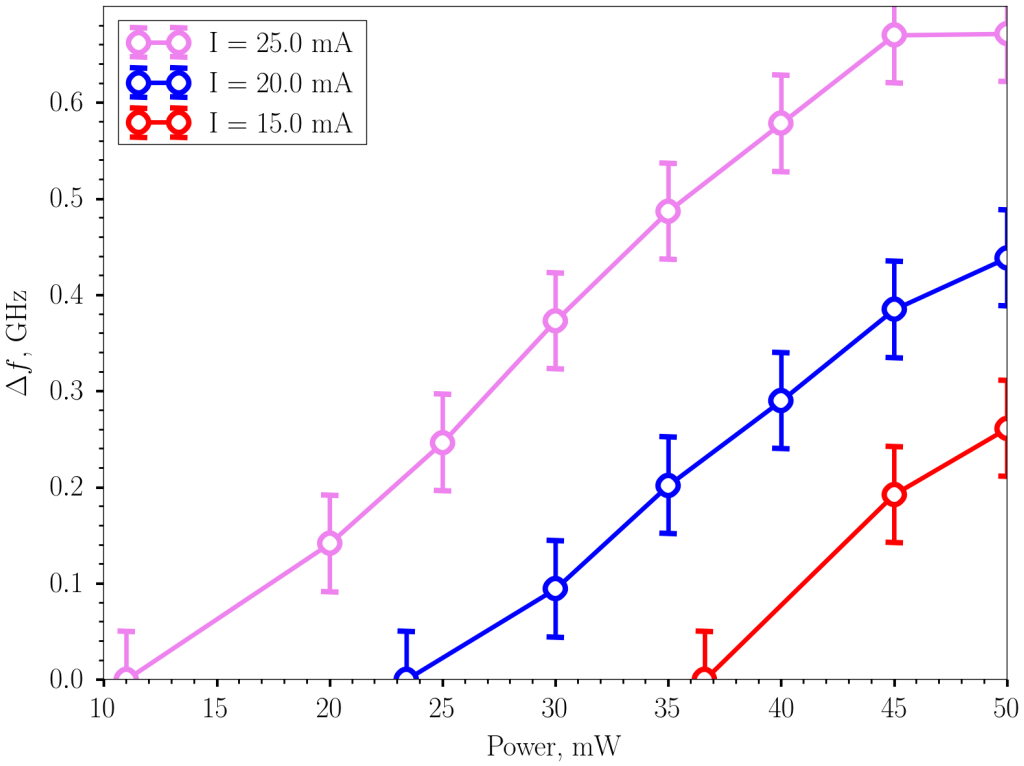

Figure 7.6: Dependences of the frequency width of the instability region Δf on the pumping power for different strengths of the direct current I, as labeled. Lines are guides for the eye.

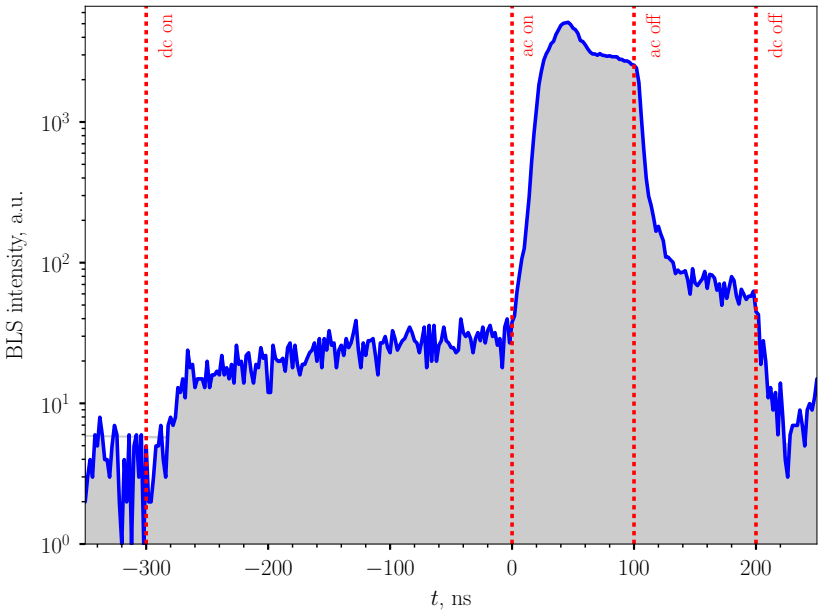

Figure 7.7: Schematic of the timing of microwave and dc pulses in the temporal measurements. At a given dc current, the temporal evolution of the parametrically excited mode is investigated at resonance as a function of the microwave power. Data for $I = 25$ mA, $P = 50$ mW.

variation is associated with the Oersted field of the current in the Pt line. Extrapolating this dependence to $I = 0$ one obtains the value of 8.5 GHz, which agrees well with the independently determined $f_{FMR} = 8.49$ GHz. This shows that the mode exhibiting parametric instability in the studied system is the quasi-uniform FMR mode of the Py microdot. Additional variation of the frequency with the increase of P above P_{th} is characterized by Figure 7.5, which shows power dependences of the frequency f_{max} corresponding to the maximum intensity in the recorded spectra, i.e. to highest efficiency of the parametric excitation. As seen from Figure 7.5, with the increase of P, f_{max} first stays constant and then starts to decrease. This red shift is apparently associated with the reduction of the saturation magnetization in Py due to the increase in the intensity of parametrically excited magnetization oscillations with the increase in the pumping power.

Finally, Figure 7.6 characterizes the controllability of the frequency width of the instability region Δf by the spin current. This data shows that apart from the possibility to switch the instability on and off by applying the spin current, varying of the strength of the spin current one can continuously

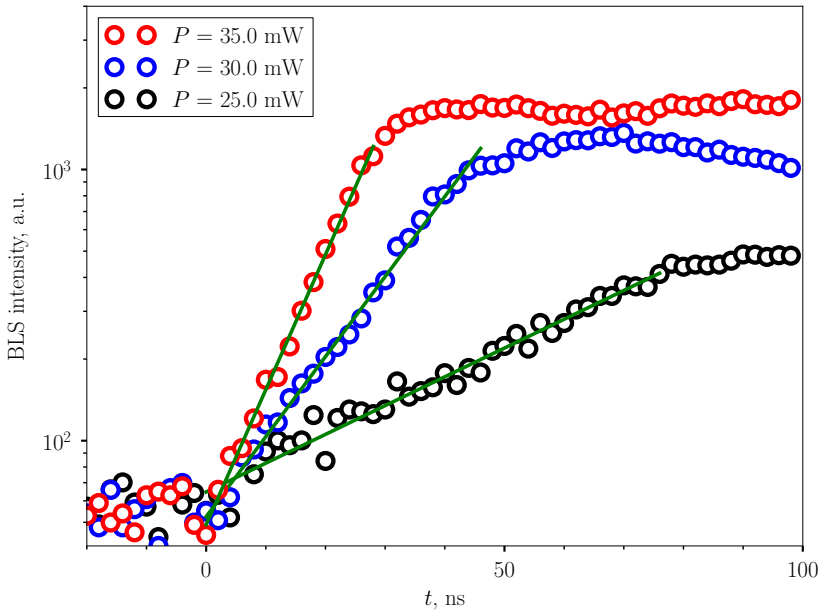

Figure 7.8: Temporal dependences of the BLS intensity after the onset of the microwave pumping pulse at $t = 0$ for different pumping powers, as labeled (note the logarithmic scale of the vertical axis). The data was obtained for $I = 20$ mA. Lines are linear fits to the experimental data.

change the frequency width of the instability region at the given pumping power. For example, at $P = 50$ mW, Δf changes from 0.3 to 0.8 GHz, i.e by more than a factor of two, as I is varied from 15 to 25 mA.

Measurements of the temporal characteristics of the parametric instability can also provide important quantitative information about the influence of the spin current on the relaxation in the Py dot. In previous studies [103,104] this information was obtained from measurements of the linewidth of the ferromagnetic resonance curve, which then can be used to calculate the Gilbert damping parameter or the relaxation frequency. In parametric-pumping experiments, the relaxation frequency and its dependence on the strength of the spin current can be determined directly based on the observation of the growth of the intensity of parametrically excited magnetization oscillations with time.

Figure 7.7 shows the timing of the dc/microwave currents, while Figure 7.8 shows in the logarithmic scale the temporal dependences of the BLS intensity after the onset of the microwave pumping pulse at $t = 0$ for different pumping powers. As shown in Figure 7.7, the onset of dc current corresponds

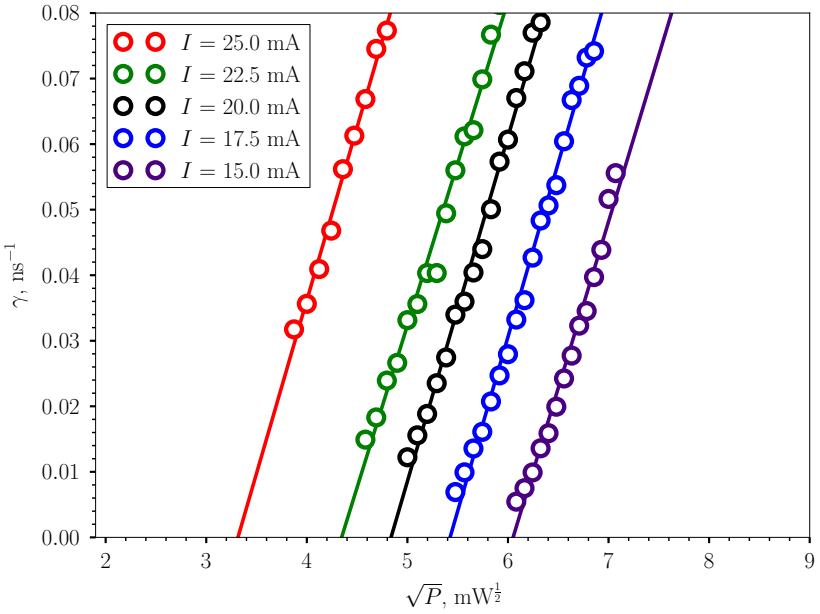

Figure 7.9: Power dependences of the growth rate of the amplitude of parametrically excited magnetization oscillations γ for different currents I, as labeled. Lines are linear fits to the experimental data.

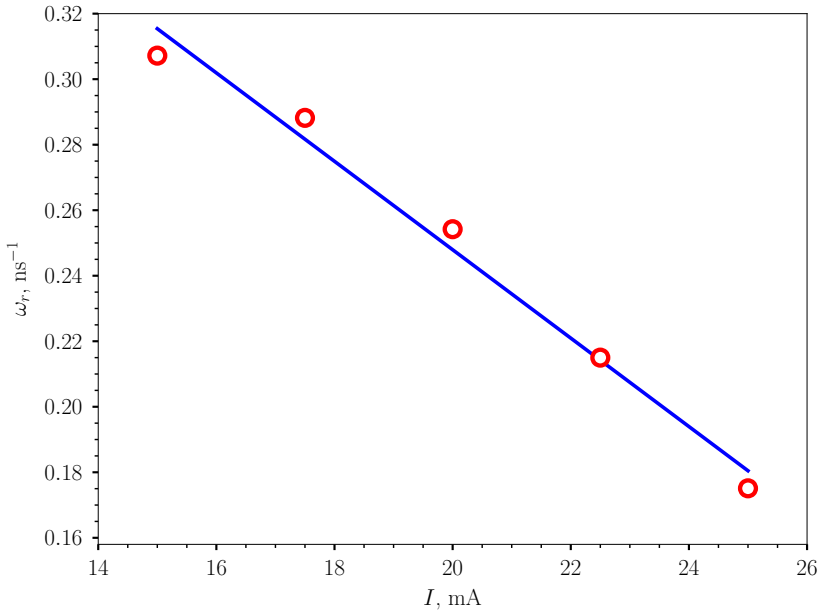

Figure 7.10: Current dependence of the relaxation frequency ω_r. Line is a linear fit to the data.

to an enhancement of magnetic fluctuations in the system, in agreement with the results of chapter 5. This dc current induced enhancement of the fluctuations is followed by the onset of the microwave magnetic field, resulting in parametric excitation of the magnetization. It is seen from Figure 7.8 that the initial growth of the intensity is exponential and is characterized by the time constant decreasing with the increase of the pumping power. This is associated with the fact that the parametric pumping reveals itself as amplification of magnetization oscillations counteracting their natural relaxation. As a result, at $P > P_{th}$ the amplitude grows exponentially with the rate $\gamma = C\sqrt{P} - \omega_r$, where the term $C\sqrt{P}$ characterizes the parametric amplification, ω_r is the relaxation frequency, and C is a constant [50, 142]. In agreement with the theory, the measured dependences $\gamma(\sqrt{p})$ shown in Figure 7.9 are linear. Extrapolating these dependences to $P = 0$, one easily finds the relaxation frequency for different values of the current I, as shown in Figure 7.10. For $I > 23.5$ mA, the relaxation frequency in the studied system is smaller than the value 0.2 ns^{-1} calculated based on the typical for Permalloy Gilbert damping parameter $\alpha = 0.008$.

7.3 Conclusion

In conclusion, we have demonstrated that the injection of pure spin currents represents an efficient mechanism for stimulation of nonlinear phenomena in microscopic magnetic structures. Our findings open advanced routes for basic studies of nonlinear magnetization dynamics on the microscopic scale, as well as for technical applications of nonlinear magnetic phenomena in spintronics. They demonstrate the important role of pure spin currents in dynamic magnetism, in general, and for spin-based electronics, in particular.

Bibliography

[1] F. Bloch, Zeitschrift für Physik A Hadrons and Nuclei **61**, 206 (1930), http://dx.doi.org/10.1007/BF01339661.

[2] A. C. Gossard, V. Jaccarino, and J. P. Remeika, Phys. Rev. Lett. **7**, 122 (1961), http://dx.doi.org/10.1103/PhysRevLett.7.122.

[3] I. Tsubokawa, J. Phys. Soc. Japan **15**, 1664 (1960), http://dx.doi.org/10.1143/JPSJ.15.1664.

[4] T. Holstein and H. Primakoff, Phys. Rev. **58**, 1098 (1940), http://dx.doi.org/10.1103/PhysRev.58.1098.

[5] C. Kittel, *Quantum theory of solids* (Wiley, New York, 1963).

[6] L. Landau, E. Lifshitz, and L. Pitaevskii, *Statistical Physics: Theory of the Condensed State* (Butterworth-Heinemann, 1980).

[7] L. D. Landau and E. M. Lifshitz, Phys. Z. Sowietunion **8**, 153 (1935).

[8] J. H. E. Griffiths, Nature **158**, 670 (1946), http://dx.doi.org/10.1038/158670a0.

[9] C. Kittel, Phys. Rev. **73**, 155 (1948), http://dx.doi.org/10.1103/PhysRev.73.155.

[10] C. Herring and C. Kittel, Phys. Rev. **81**, 869 (1951), http://dx.doi.org/10.1103/PhysRev.81.869.

[11] R. L. White and I. H. Solt, Phys. Rev. **104**, 56 (1956), http://dx.doi.org/10.1103/PhysRev.104.56.

[12] L. R. Walker, Phys. Rev. **105**, 390 (1957), http://dx.doi.org/10.1103/PhysRev.105.390.

[13] J. F. Dillon, Phys. Rev. **112**, 59 (1958), http://dx.doi.org/10.1103/PhysRev.112.59.

[14] J. F. Dillon Jr., J. Appl. Phys. **31**, 1605 (1960), http://dx.doi.org/10.1063/1.1735901.

[15] L. R. Walker, J. Appl. Phys. **29**, 318 (1958), http://dx.doi.org/10.1063/1.1723117.

[16] C. Kittel, Phys. Rev. **110**, 1295 (1958), http://dx.doi.org/10.1103/PhysRev.110.1295.

[17] M. H. Seavey and P. E. Tannenwald, Phys. Rev. Lett. **1**, 168 (1958), http://dx.doi.org/10.1103/PhysRevLett.1.168.

[18] R. Damon and J. Eshbach, J. Phys. Chem. Solids **19**, 308 (1961), http://dx.doi.org/10.1016/0022-3697(61)90041-5.

[19] M. Hurben and C. Patton, J. Magn. Magn. Mater. **139**, 263 (1995), http://dx.doi.org/10.1016/0304-8853(95)90006-3.

[20] M. Hurben and C. Patton, J. Magn. Magn. Mater. **163**, 39 (1996), http://dx.doi.org/10.1016/S0304-8853(96)00294-6.

[21] B. Kalinikos, IEE Proc. H **127**, 4 (1980), http://dx.doi.org/10.1049/ip-h-1:19800002.

[22] B. A. Kalinikos and A. N. Slavin, J. Phys. C: Solid State Phys. **19**, 7013 (1986), http://dx.doi.org/10.1088/0022-3719/19/35/014.

[23] M. Sparks, Phys. Rev. Lett. **24**, 1178 (1970), http://dx.doi.org/10.1103/PhysRevLett.24.1178.

[24] M. Sparks, Phys. Rev. B **1**, 3831 (1970), http://dx.doi.org/10.1103/PhysRevB.1.3831.

[25] R. E. De Wames and T. Wolfram, J. Appl. Phys. **41**, 987 (1970), http://dx.doi.org/10.1063/1.1659049.

[26] J. Adam, L. Davis, G. Dionne, E. Schloemann, and S. Stitzer, IEEE Trans. Micro. Theory Tech. **50**, 721 (2002), http://dx.doi.org/10.1109/22.989957.

[27] J. P. Parekh, Circuits, Systems, and Signal Processing **4**, 5 (1985), http://dx.doi.org/10.1007/BF01600070.

[28] V. Cherepanov, I. Kolokolov, and V. L'vov, Phys. Rep. **229**, 81 (1993), http://dx.doi.org/10.1016/0370-1573(93)90107-O.

[29] A. A. Serga, A. V. Chumak, and B. Hillebrands, J. Phys. D: Appl. Phys. **43**, 264002 (2010), http://dx.doi.org/10.1088/0022-3727/43/26/264002.

[30] T. Schneider, A. A. Serga, B. Leven, B. Hillebrands, R. L. Stamps, and M. P. Kostylev, Appl. Phys. Lett. **92**, 022505 (2008), http://dx.doi.org/10.1063/1.2834714.

[31] A. V. Chumak *et al.*, Nat. Commun. **1**, 141 (2010), http://dx.doi.org/10.1038/ncomms1142.

[32] S. I. Kiselev, J. C. Sankey, I. N. Krivorotov, N. C. Emley, R. J. Schoelkopf, R. A. Buhrman, and D. C. Ralph, Nature **425**, 380 (2003), http://dx.doi.org/10.1038/nature01967.

[33] S. Kaka, M. R. Pufall, W. H. Rippard, T. J. Silva, S. E. Russek, and J. A. Katine, Nature **437**, 389 (2005), http://dx.doi.org/10.1038/nature04035.

[34] F. B. Mancoff, N. D. Rizzo, B. N. Engel, and S. Tehrani, Nature **437**, 393 (2005), http://dx.doi.org/10.1038/nature04036.

[35] A. Dussaux *et al.*, Nat. Commun. **1**, 8 (2010), http://dx.doi.org/10.1038/ncomms1006.

[36] A. A. Tulapurkar, Y. Suzuki, A. Fukushima, H. Kubota, H. Maehara, K. Tsunekawa, D. D. Djayaprawira, N. Watanabe, and S. Yuasa, Nature **438**, 339 (2005), http://dx.doi.org/10.1038/nature04207.

[37] X. Cheng, C. T. Boone, J. Zhu, and I. N. Krivorotov, Phys. Rev. Lett. **105**, 047202 (2010), http://dx.doi.org/10.1103/PhysRevLett.105.047202.

[38] V. E. Demidov, S. Urazhdin, and S. O. Demokritov, Nature Mater. **9**, 984 (2010), http://dx.doi.org/10.1038/nmat2882.

[39] V. V. Kruglyak, S. O. Demokritov, and D. Grundler, J. Phys. D: Appl. Phys. **43**, 264001 (2010), http://dx.doi.org/10.1088/0022-3727/43/26/264001.

[40] V. E. Demidov, S. Urazhdin, V. Tiberkevich, A. Slavin, and S. O. Demokritov, Phys. Rev. B **83**, 060406 (2011), http://dx.doi.org/10.1103/PhysRevB.83.060406.

[41] I. N. Krivorotov, N. C. Emley, J. C. Sankey, S. I. Kiselev, D. C. Ralph, and R. A. Buhrman, Science **307**, 228 (2005), http://dx.doi.org/10.1126/science.1105722.

[42] J. C. Sankey, P. M. Braganca, A. G. F. Garcia, I. N. Krivorotov, R. A. Buhrman, and D. C. Ralph, Phys. Rev. Lett. **96**, 227601 (2006), http://dx.doi.org/10.1103/PhysRevLett.96.227601.

[43] J. F. Dillon Jr., H. Kamimura, and J. P. Remeika, J. Appl. Phys. **34**, 1240 (1963), http://dx.doi.org/10.1063/1.1729455.

[44] I. Neudecker, K. Perzlmaier, F. Hoffmann, G. Woltersdorf, M. Buess, D. Weiss, and C. H. Back, Phys. Rev. B **73**, 134426 (2006), http://dx.doi.org/10.1103/PhysRevB.73.134426.

[45] J. Li, M.-S. Lee, W. He, B. Redeker, A. Remhof, E. Amaladass, C. Hassel, and T. Eimuller, Rev. Sci. Instrum. **80**, 073703 (2009), http://dx.doi.org/10.1063/1.3170448.

[46] S. Tamaru, J. A. Bain, M. H. Kryder, and D. S. Ricketts, Phys. Rev. B **84**, 064437 (2011), http://dx.doi.org/10.1103/PhysRevB.84.064437.

[47] A. Borovik-Romanov and N. Kreines, Phys. Rep. **81**, 351 (1982), http://dx.doi.org/10.1016/0370-1573(82)90118-1.

[48] S. O. Demokritov, B. Hillebrands, and A. N. Slavin, Phys. Rep. **348**, 441 (2001), http://dx.doi.org/10.1016/S0370-1573(00)00116-2.

[49] C. Cohen-Tannoudji, B. Diu, and F. Laloe, *Quantum mechanics* (Wiley, New York, 1977).

[50] A. Gurevich and G. Melkov, *Magnetization Oscillations and Waves* (CRC-Press, 1996).

[51] L. D. Landau and E. M. Lifshitz, *Electrodynamics of continuous media* (Pergamon Press, 1960).

[52] D. Polder, Philos. Mag. **40**, 99 (1949).

[53] T. Gilbert, IEEE Trans. Magn. **40**, 3443 (2004), http://dx.doi.org/10.1109/TMAG.2004.836740.

[54] N. Bloembergen, E. M. Purcell, and R. V. Pound, Phys. Rev. **73**, 679 (1948), http://dx.doi.org/10.1103/PhysRev.73.679.

[55] G. Rado and J. Weertman, J. Phys. Chem. Solids **11**, 315 (1959), http://dx.doi.org/10.1016/0022-3697(59)90233-1.

[56] M. J. Lighthill, IMA J. Appl. Math **1**, 1 (1965), http://dx.doi.org/10.1093/imamat/1.1.1.

[57] B. Taylor, H. J. Maris, and C. Elbaum, Phys. Rev. Lett. **23**, 416 (1969), http://dx.doi.org/10.1103/PhysRevLett.23.416.

[58] B. Taylor, H. J. Maris, and C. Elbaum, Phys. Rev. B **3**, 1462 (1971), http://dx.doi.org/10.1103/PhysRevB.3.1462.

[59] G. A. Northrop and J. P. Wolfe, Phys. Rev. B **22**, 6196 (1980), http://dx.doi.org/10.1103/PhysRevB.22.6196.

[60] V. Veerakumar and R. E. Camley, Phys. Rev. B **74**, 214401 (2006), http://dx.doi.org/10.1103/PhysRevB.74.214401.

[61] O. Büttner, M. Bauer, S. O. Demokritov, B. Hillebrands, Y. S. Kivshar, V. Grimalsky, Y. Rapoport, and A. N. Slavin, Phys. Rev. B **61**, 11576 (2000), http://dx.doi.org/10.1103/PhysRevB.61.11576.

[62] T. Schneider, A. A. Serga, A. V. Chumak, C. W. Sandweg, S. Trudel, S. Wolff, M. P. Kostylev, V. S. Tiberkevich, A. N. Slavin, and B. Hillebrands, Phys. Rev. Lett. **104**, 197203 (2010), http://dx.doi.org/10.1103/PhysRevLett.104.197203.

[63] M. P. Kostylev, A. A. Serga, and B. Hillebrands, Phys. Rev. Lett. **106**, 134101 (2011), http://dx.doi.org/10.1103/PhysRevLett.106.134101.

[64] V. E. Demidov, S. O. Demokritov, D. Birt, B. O'Gorman, M. Tsoi, and X. Li, Phys. Rev. B **80**, 014429 (2009), http://dx.doi.org/10.1103/PhysRevB.80.014429.

[65] D. R. Birt, B. O'Gorman, M. Tsoi, X. Li, V. E. Demidov, and S. O. Demokritov, Appl. Phys. Lett. **95**, 122510 (2009), http://dx.doi.org/10.1063/1.3237168.

[66] C. Mathieu, J. Jorzick, A. Frank, S. O. Demokritov, A. N. Slavin, B. Hillebrands, B. Bartenlian, C. Chappert, D. Decanini, F. Rousseaux, *et al.*, Phys. Rev. Lett. **81**, 3968 (1998), http://dx.doi.org/10.1103/PhysRevLett.81.3968.

[67] J. Jorzick, S. O. Demokritov, C. Mathieu, B. Hillebrands, B. Bartenlian, C. Chappert, F. Rousseaux, and A. N. Slavin, Phys. Rev. B **60**, 15194 (1999), http://dx.doi.org/10.1103/PhysRevB.60.15194.

[68] J. P. Park, P. Eames, D. M. Engebretson, J. Berezovsky, and P. A. Crowell, Phys. Rev. Lett. **89**, 277201 (2002), http://dx.doi.org/10.1103/PhysRevLett.89.277201.

[69] C. Bayer, S. O. Demokritov, B. Hillebrands, and A. N. Slavin, Appl. Phys. Lett. **82**, 607 (2003), http://dx.doi.org/10.1063/1.1540734.

[70] C. Bayer, J. P. Park, H. Wang, M. Yan, C. E. Campbell, and P. A. Crowell, Phys. Rev. B **69**, 134401 (2004), http://dx.doi.org/10.1103/PhysRevB.69.134401.

[71] J. Jorzick, S. O. Demokritov, B. Hillebrands, M. Bailleul, C. Fermon, K. Y. Guslienko, A. N. Slavin, D. V. Berkov, and N. L. Gorn, Phys. Rev. Lett. **88**, 047204 (2002), http://dx.doi.org/10.1103/PhysRevLett.88.047204.

[72] K. Y. Guslienko, R. W. Chantrell, and A. N. Slavin, Phys. Rev. B **68**, 024422 (2003), http://dx.doi.org/10.1103/PhysRevB.68.024422.

[73] A. Barman, V. V. Kruglyak, R. J. Hicken, J. M. Rowe, A. Kundrotaite, J. Scott, and M. Rahman, Phys. Rev. B **69**, 174426 (2004), http://dx.doi.org/10.1103/PhysRevB.69.174426.

[74] P. H. Bryant, J. F. Smyth, S. Schultz, and D. R. Fredkin, Phys. Rev. B **47**, 11255 (1993), http://dx.doi.org/10.1103/PhysRevB.47.11255.

[75] K. Perzlmaier, M. Buess, C. H. Back, V. E. Demidov, B. Hillebrands, and S. O. Demokritov, Phys. Rev. Lett. **94**, 057202 (2005), http://dx.doi.org/10.1103/PhysRevLett.94.057202.

[76] S. O. Demokritov, *Spin Wave Confinement* (Pan Stanford Publishing, 2008).

[77] K. Y. Guslienko, S. O. Demokritov, B. Hillebrands, and A. N. Slavin, Phys. Rev. B **66**, 132402 (2002), http://dx.doi.org/10.1103/PhysRevB.66.132402.

[78] R. I. Joseph and E. Schlömann, J. Appl. Phys. **36**, 1579 (1965), http://dx.doi.org/10.1063/1.1703091.

[79] E. Schlömann, J. Appl. Phys. **35**, 159 (1964), http://dx.doi.org/10.1063/1.1713058.

[80] J. Jorzick *et al.*, J. Appl. Phys. **89**, 7091 (2001), http://dx.doi.org/10.1063/1.1357153.

[81] N. Smith and P. Arnett, Appl. Phys. Lett. **78**, 1448 (2001), http://dx.doi.org/10.1063/1.1352694.

[82] J.-G. Zhu, J. Appl. Phys. **91**, 7273 (2002), http://dx.doi.org/10.1063/1.1452675.

[83] Y. Zhou, A. Roesler, and J.-G. Zhu, J. Appl. Phys. **91**, 7276 (2002), http://dx.doi.org/10.1063/1.1452676.

[84] J. Weber, Phys. Rev. **101**, 1620 (1956), http://dx.doi.org/10.1103/PhysRev.101.1620.

[85] R. Kubo, Rep. Prog. Phys. **29**(1), 255 (1966), http://dx.doi.org/10.1088/0034-4885/29/1/306.

[86] W. F. Brown, Phys. Rev. **130**, 1677 (1963), http://dx.doi.org/10.1103/PhysRev.130.1677.

[87] N. Smith, J. Appl. Phys. **90**, 5768 (2001), http://dx.doi.org/10.1063/1.1402146.

[88] N. Smith, J. Appl. Phys. **92**, 3877 (2002), http://dx.doi.org/10.1063/1.1500782.

[89] M. N. Baibich, J. M. Broto, A. Fert, F. N. Van Dau, F. Petroff, P. Etienne, G. Creuzet, A. Friederich, and J. Chazelas, Phys. Rev. Lett. **61**, 2472 (1988), http://dx.doi.org/10.1103/PhysRevLett.61.2472.

[90] G. Binasch, P. Grünberg, F. Saurenbach, and W. Zinn, Phys. Rev. B **39**, 4828 (1989), http://dx.doi.org/10.1103/PhysRevB.39.4828.

[91] D. Ralph and M. Stiles, J. Magn. Magn. Mater. **320**, 1190 (2008), http://dx.doi.org/10.1016/j.jmmm.2007.12.019.

[92] J. Slonczewski, Journal of Magnetism and Magnetic Materials **159**, L1 (1996), http://dx.doi.org/10.1016/0304-8853(96)00062-5.

[93] L. Berger, Phys. Rev. B **54**, 9353 (1996), http://dx.doi.org/10.1103/PhysRevB.54.9353.

[94] W. P. Pratt, S.-F. Lee, J. M. Slaughter, R. Loloee, P. A. Schroeder, and J. Bass, Phys. Rev. Lett. **66**, 3060 (1991), http://dx.doi.org/10.1103/PhysRevLett.66.3060.

[95] D. C. Langreth and J. W. Wilkins, Phys. Rev. B **6**, 3189 (1972), http://dx.doi.org/10.1103/PhysRevB.6.3189.

[96] C. Vouille, A. Barthélémy, F. Elokan Mpondo, A. Fert, P. A. Schroeder, S. Y. Hsu, A. Reilly, and R. Loloee, Phys. Rev. B **60**, 6710 (1999), http://dx.doi.org/10.1103/PhysRevB.60.6710.

[97] E. C. Stoner, Proc. R. Soc. Lond. A **169**(938), 339 (1939), http://dx.doi.org/10.1098/rspa.1939.0003.

[98] M. D. Stiles and A. Zangwill, Phys. Rev. B **66**, 014407 (2002), http://dx.doi.org/10.1103/PhysRevB.66.014407.

[99] M. Tsoi, A. G. M. Jansen, J. Bass, W.-C. Chiang, M. Seck, V. Tsoi, and P. Wyder, Phys. Rev. Lett. **80**, 4281 (1998), http://dx.doi.org/10.1103/PhysRevLett.80.4281.

[100] S. Petit, C. Baraduc, C. Thirion, U. Ebels, Y. Liu, M. Li, P. Wang, and B. Dieny, Phys. Rev. Lett. **98**, 077203 (2007), http://dx.doi.org/10.1103/PhysRevLett.98.077203.

[101] M. I. Dyakonov and V. I. Perel, JETP Lett. **13**, 467 (1971).

[102] M. Dyakonov and V. Perel, Phys. Lett. A **35**, 459 (1971), http://dx.doi.org/10.1016/0375-9601(71)90196-4.

[103] K. Ando, S. Takahashi, K. Harii, K. Sasage, J. Ieda, S. Maekawa, and E. Saitoh, Phys. Rev. Lett. **101**, 036601 (2008), http://dx.doi.org/10.1103/PhysRevLett.101.036601.

[104] L. Liu, T. Moriyama, D. C. Ralph, and R. A. Buhrman, Phys. Rev. Lett. **106**, 036601 (2011), http://dx.doi.org/10.1103/PhysRevLett.106.036601.

[105] O. Mosendz, J. E. Pearson, F. Y. Fradin, G. E. W. Bauer, S. D. Bader, and A. Hoffmann, Phys. Rev. Lett. **104**, 046601 (2010), http://dx.doi.org/10.1103/PhysRevLett.104.046601.

[106] S. Murakami, N. Nagaosa, and S.-C. Zhang, Science **301**, 1348 (2003), http://dx.doi.org/10.1126/science.1087128.

[107] J. Sinova, D. Culcer, Q. Niu, N. A. Sinitsyn, T. Jungwirth, and A. H. MacDonald, Phys. Rev. Lett. **92**, 126603 (2004), http://dx.doi.org/10.1103/PhysRevLett.92.126603.

[108] Y. K. Kato, R. C. Myers, A. C. Gossard, and D. D. Awschalom, Science **306**, 1910 (2004), http://dx.doi.org/10.1126/science.1105514.

[109] J. Wunderlich, B. Kaestner, J. Sinova, and T. Jungwirth, Phys. Rev. Lett. **94**, 047204 (2005), http://dx.doi.org/10.1103/PhysRevLett.94.047204.

[110] T. Jungwirth, J. Wunderlich, and K. Olejník, Nature Mater. **11**, 382 (2012), http://dx.doi.org/10.1038/nmat3279.

[111] E. Saitoh, M. Ueda, H. Miyajima, and G. Tatara, Appl. Phys. Lett. **88**, 182509 (2006), http://dx.doi.org/10.1063/1.2199473.

[112] K. Ando, J. Ieda, K. Sasage, S. Takahashi, S. Maekawa, and E. Saitoh, Appl. Phys. Lett. **94**, 262505 (2009), http://dx.doi.org/10.1063/1.3167826.

[113] O. Mosendz, V. Vlaminck, J. E. Pearson, F. Y. Fradin, G. E. W. Bauer, S. D. Bader, and A. Hoffmann, Phys. Rev. B **82**, 214403 (2010), http://dx.doi.org/10.1103/PhysRevB.82.214403.

[114] Y. Kajiwara, K. Harii, S. Takahashi, J. Ohe, K. Uchida, M. Mizuguchi, H. Umezawa, H. Kawai, K. Ando, K. Takanashi, *et al.*, Nature **464**, 262 (2010), http://dx.doi.org/10.1038/nature08876.

[115] Y. Tserkovnyak, A. Brataas, and G. E. W. Bauer, Phys. Rev. Lett. **88**, 117601 (2002), http://dx.doi.org/10.1103/PhysRevLett.88.117601.

[116] Y. Tserkovnyak, A. Brataas, G. E. W. Bauer, and B. I. Halperin, Rev. Mod. Phys. **77**, 1375 (2005), http://dx.doi.org/10.1103/RevModPhys.77.1375.

[117] N. Bloembergen and R. W. Damon, Phys. Rev. **85**, 699 (1952), http://dx.doi.org/10.1103/PhysRev.85.699.

[118] P. W. Anderson and H. Suhl, Phys. Rev. **100**, 1788 (1955), http://dx.doi.org/10.1103/PhysRev.100.1788.

[119] E. Schlomann, J. J. Green, and U. Milano, J. Appl. Phys. **31**, S386 (1960), http://dx.doi.org/10.1063/1.1984759.

[120] H. Suhl, J. Phys. Chem. Solids **1**, 209 (1957), http://dx.doi.org/10.1016/0022-3697(57)90010-0.

[121] C. E. Patton, J. Appl. Phys. **40**, 2837 (1969), http://dx.doi.org/10.1063/1.1658085.

[122] V. E. Demidov, S. O. Demokritov, B. Hillebrands, M. Laufenberg, and P. P. Freitas, Appl. Phys. Lett. **85**, 2866 (2004), http://dx.doi.org/10.1063/1.1803621.

[123] S. Demokritov and V. Demidov, IEEE Trans. Magn. **44**, 6 (2008), http://dx.doi.org/10.1109/TMAG.2007.910227.

[124] M. Cottam and D. Lockwood, *Light scattering in magnetic solids* (Wiley, 1986).

[125] H. le Gall and J. P. Jamet, Phys. Stat. Solidi B **46**(2), 467 (1971), http://dx.doi.org/10.1002/pssb.2220460202.

[126] R. Mock, B. Hillebrands, and R. Sandercock, J. Phys. E: Sci. Instrum. **20**, 656 (1987), http://dx.doi.org/10.1088/0022-3735/20/6/017.

[127] M. Born and E. Wolf, *Principles of Optics: Electromagnetic Theory of Propagation, Interference and Diffraction of Light* (Cambridge University Press, 1999).

[128] J. Sandercock, in H. Queisser, ed., *Festkrperprobleme 15* (Springer Berlin / Heidelberg, 1975), vol. 15 of *Advances in Solid State Physics*, pp. 183–202, ISBN 978-3-528-08021-1, http://dx.doi.org/10.1007/BFb0107378.

[129] S. Tamaru, J. A. Bain, R. J. M. van de Veerdonk, T. M. Crawford, M. Covington, and M. H. Kryder, J. Appl. Phys. **91**, 8034 (2002), http://dx.doi.org/10.1063/1.1450815.

[130] A. Zvezdin and V. Kotov, *Modern Magnetooptics and Magnetooptical Materials* (Taylor & Francis, 1997).

[131] A. Yariv and P. Yeh, *Optical Waves in Crystals: Propagation and Control of Laser Radiation* (Wiley, 2002).

[132] M. J. Donahue, D. G. Porter, N. I. of Standards, and T. (U.S.), *OOMMF user's guide [microform] / M.J. Donahue, D.G. Porter* (U.S. Dept. of Commerce, Technology Administration, National Institute of Standards and Technology, Gaithersburg, MD :, 1999), version 1.0. ed.

[133] W. P. Wolf and G. P. Rodrigue, J. Appl. Phys. **29**, 105 (1958), http://dx.doi.org/10.1063/1.1722928.

[134] V. E. Demidov, U.-H. Hansen, and S. O. Demokritov, Phys. Rev. Lett. **98**, 157203 (2007), http://dx.doi.org/10.1103/PhysRevLett.98.157203.

[135] V. E. Demidov, M. Buchmeier, K. Rott, P. Krzysteczko, J. Münchenberger, G. Reiss, and S. O. Demokritov, Phys. Rev. Lett. **104**, 217203 (2010), http://dx.doi.org/10.1103/PhysRevLett.104.217203.

[136] M. Kostylev, V. E. Demidov, U.-H. Hansen, and S. O. Demokritov, Phys. Rev. B **76**, 224414 (2007), http://dx.doi.org/10.1103/PhysRevB.76.224414.

[137] J. Jersch, V. E. Demidov, H. Fuchs, K. Rott, P. Krzysteczko, J. Munchenberger, G. Reiss, and S. O. Demokritov, Appl. Phys. Lett. **97**, 152502 (2010), http://dx.doi.org/10.1063/1.3502599.

[138] A. Slavin and V. Tiberkevich, IEEE Trans. Magn. **45**, 1875 (2009), http://dx.doi.org/10.1109/TMAG.2008.2009935.

[139] S. M. Rezende, F. M. de Aguiar, and A. Azevedo, Phys. Rev. B **73**, 094402 (2006), http://dx.doi.org/10.1103/PhysRevB.73.094402.

[140] S. Mizukami, Y. Ando, and T. Miyazaki, Phys. Rev. B **66**, 104413 (2002), http://dx.doi.org/10.1103/PhysRevB.66.104413.

[141] J. O. Rantschler, R. D. McMichael, A. Castillo, A. J. Shapiro, J. W. F. Egelhoff, B. B. Maranville, D. Pulugurtha, A. P. Chen, and L. M. Connors, J. Appl. Phys. **101**, 033911 (2007), http://dx.doi.org/10.1063/1.2436471.

[142] V. L'vov, *Wave Turbulence under Parametric Excitation* (Springer, 1994).

[143] H. Ulrichs, V. E. Demidov, S. O. Demokritov, and S. Urazhdin, Phys. Rev. B **84**, 094401 (2011), http://dx.doi.org/10.1103/PhysRevB.84.094401.